Strain-Based Design and Assessment in Critical Areas of Pipeline Systems with Realistic Anomalies

Appendix B: Properties of Materials Used for Curved-Wide-Plate Tests

Contract No. DTPH56-14-H-00003

Prepared for

US Department of Transportation
Pipeline and Hazardous Materials Safety Administration
Office of Pipeline Safety

Prepared by

Timothy Weeks

NIST

Jim Gianetto

Natural Resources Canada | Ressources naturelles Canada

CANMET

Ming Liu and Yong-Yi Wang

CRES

Center for Reliable Energy Systems

July 10, 2017

Notice

This project was funded by the Department of Transportation, Pipeline and Hazardous Materials Safety Administration under the Pipeline Safety Research and Development Program. The views and conclusions contained in this document are those of the authors and should not be interpreted as representing the official policies, either expressed or implied, of the Pipeline and Hazardous Materials Safety Administration, or the U.S. Government.

Acknowledgements

NIST gratefully acknowledges the technical contribution of Ross Rentz for his participation in every aspect of the small-scale test program conducted at NIST. NIST also gratefully acknowledges the technical contributions from Ryan White, Nik Hrabe and Nikki Rentz for their expertise with sectioning and imaging for the small-scale test program conducted at NIST. Finally, NIST gratefully acknowledges the technical contribution of Enrico Lucon for conducting the data analysis of the SE(T) specimens tested at NIST.

Thanks are also due to several technical staff members at CanmetMATERIALS, including Mr. J. Liang for performing mechanical testing, Ms. P. Liu and Ms. R. Zavadil for metallographic analysis and microhardness testing as well as Mr. J-P. Talon and Mr. D. Sebesta for their expertise with machining of sub-press assemblies and small-scale test specimens. The support and guidance provided by Dr. M. Arafin, Program Manager-Pipelines is greatly appreciated. Additional funding provided by the Federal Program for Energy Research and Development (PERD) and Natural Resources Canada is also acknowledged.

Table of Contents

Nomenclature

Abbreviations

CMOD	Crack mouth opening displacement
CTOD	Crack tip opening displacement
$CTOD_A$	Apparent CTOD toughness
$CTOD_F$	CTOD driving force
$CTOD_R$	CTOD resistance
CWP	Curved wide plate
DIC	Digital image correlation
FCAW	Flux-cored arc welding
HAZ	Heat affected zone
ID	Inside diameter
LVDT	Linear variable displacement transducer
OD	Outside diameter
SE(T)	Single edge notch tension
WT	Wall thickness
YS	Yield strength

Organizations

API	American Petroleum Institute
ASME	The American Society of Mechanical Engineers
CRES	Center for Reliable Energy Systems
CSA	Canadian Standards Association
DNV	Det Norske Veritas
DOT	Department of Transportation
NIST	National Institute of Standards and Technology
PHMSA	Pipeline and Hazardous Materials Safety Administration
PRCI	Pipeline Research Council International
UOA	University of Alberta

Appendix B - Properties of Materials Used in Curve-Wide-Plate Tests

B.1 Small-Scale Specimen Sectioning

The small scale test specimens and CWP test specimens were sectioned from the two welded pipes in several steps to include plasma cutting of longitudinal strips and band saw cutting the small scale test sections. The 12 o'clock reference is defined by an axial line that bisects the girth weld between the seam welds of each pipe section. The offset between seam welds was not the same between the two pipes. This is shown in the annotated photograph in Figure B1. The sectioning plan was designed to maximize the coincidence between circumferential locations of the CWP specimens. This is shown by the axial centerlines drawn within the CWP specimens in Figure B2.

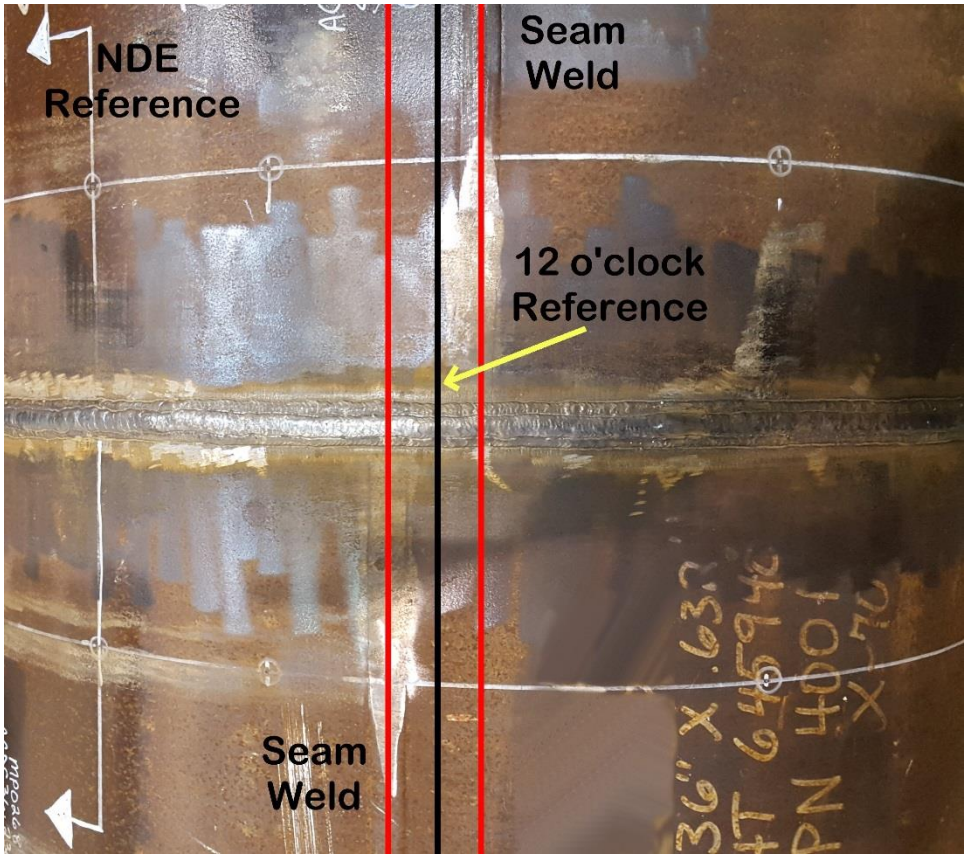

Figure B1 Annotated photograph of a pipe section girth weld with lines (red) aligned with each seam and the 12 o'clock reference line (black) used throughout the test program. The time-of-flight diffraction (TOFD) ultrasonic weld inspection report used a different reference and direction as indicated in the photograph.

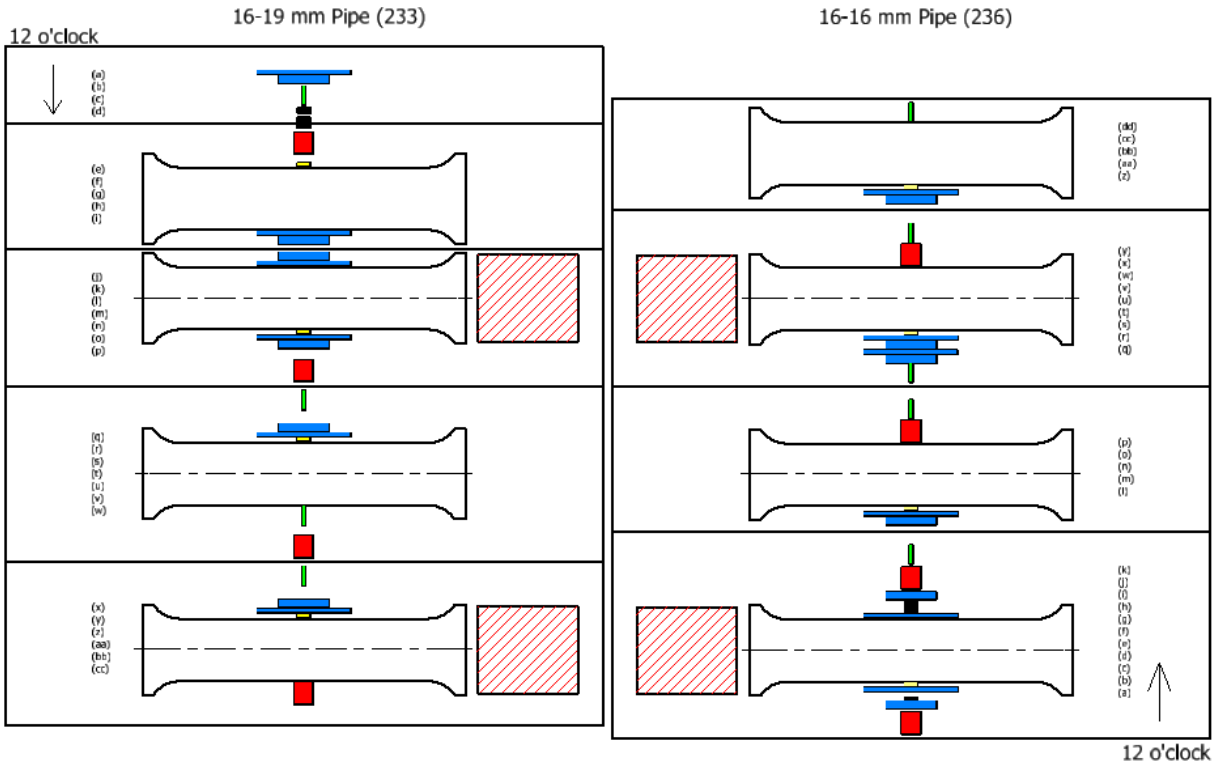

Figure B2 Schematic diagram indicating the location of CWP and small scale test sections. The 12 o'clock references are opposite in this view for the purpose of measurements and to show location coincidence between CWP specimens sectioned from the two pipes.

The reference letters shown in Figure B2 are described with small scale specimen identifiers shown in Table B1 and Table B2 for the 16 mm – 19 mm WT welded pipe (Weld 233 (Weld-2)) and the 16 mm – 16 mm WT welded pipe (Weld 236 (Weld-1)) respectively.

Table B1 Specimen sectioning legend for the 16 mm – 19 mm WT welded pipe (Weld 233)

Reference	Specimen ID	Reference	Specimen ID	Reference	Specimen ID
a	SET-1	k	SET-3	u	CWP-3
b	CTOD-1	l	CWP-2	v	AWMT-3
c	AWMT-1	m	Hardness-2	w	Charpy-3
d	NDE Indications	n	SET-4	x	AWMT-4
e	Charpy - 1	o	CTOD-4	y	CTOD-6
f	Hardness-1	p	Charpy-2	z	SET-6
g	CWP-1	q	AWMT-2	aa	Hardness-4
h	SET-2	r	CTOD-5	bb	CWP-4
i	CTOD-2	s	SET-5	cc	Charpy-4
j	CTOD-3	t	Hardness-3		

Table B2 Specimen sectioning legend for the 16 mm – 16 mm WT welded pipe (Weld 236 (Weld-1))

Reference	Specimen ID	Reference	Specimen ID	Reference	Specimen ID
a	Charpy-1	k	AWMT-1	u	SET-5
b	CTOD-1	l	CTOD-3	v	Hardness-3
c	NDE Indications	m	SET-3	w	CWP-3
d	SET-1	n	CWP-2	x	Charpy-4
e	Hardness-1	o	Charpy-3	y	AWMT-4
f	CWP-1	p	AWMT-2	z	CTOD-6
g	SET-2	q	AWMT-3	aa	SET-6
h	NDE Indications	r	CTOD-4	bb	Hardness-4
i	CTOD-2	s	SET-4	cc	CWP-4
j	Charpy-2	t	CTOD-5	dd	AWMT-5

The red hatched boxes in Figure B2 indicate the panels from which base metal specimens were taken. The sectioning details for base metal tensile specimens are shown in Figure B3. Note that sections were cut for flat tensile specimens but were not tested as part of this project.

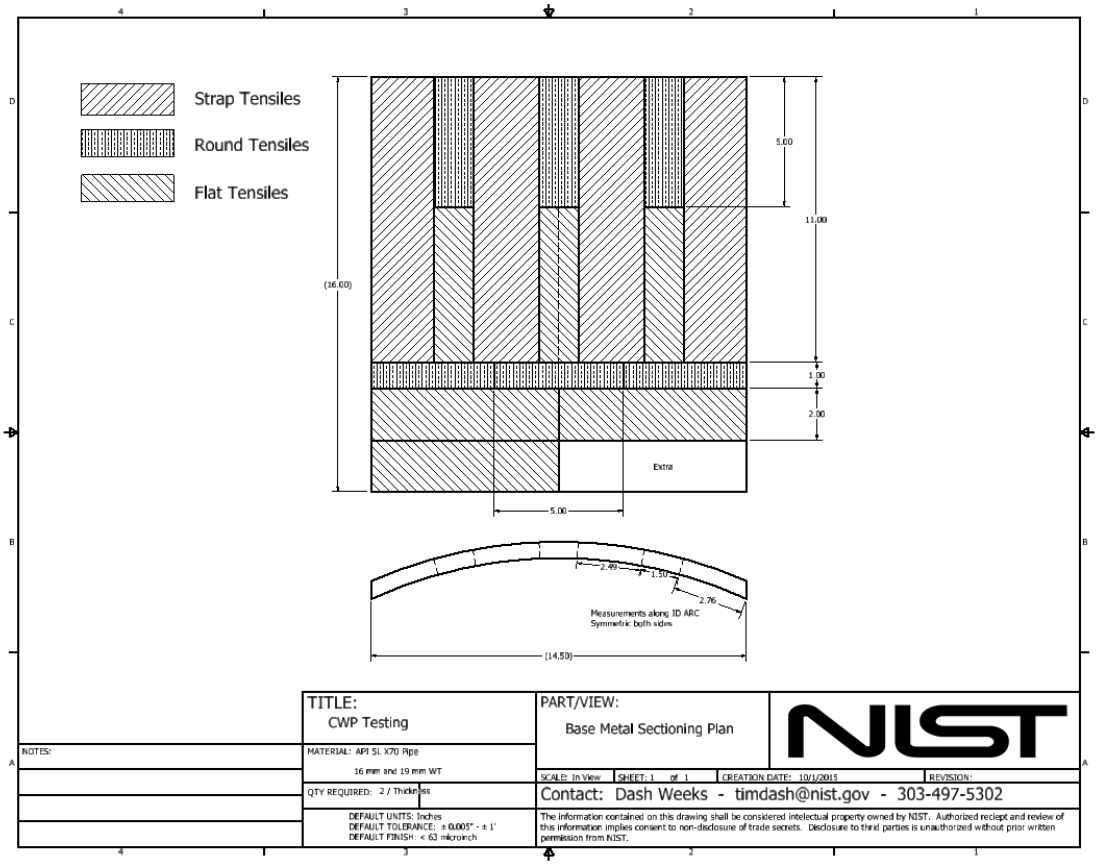

Figure B3 Base metal test specimen sectioning plan

B.2 Material Chemistry

The chemical compositions of the Grade 483 (API 5L X70) sections of pipe on either side of the respective girth welds were determined by optical emission spectroscopy (OES). In this case, the compositions of the pipe base metals were analyzed on the through-thickness surface for the respective pipes (Weld 236 (Weld-1): 16 mm to 16 mm WT pipe) and (Weld 233 (Weld-2): 16 mm to 19 mm WT pipe). The chemical compositions of the weld metal were determined on the through-thickness surface of weld cross-sections as well as on the top surface where the reinforcement of the cap passes was removed. This allowed the chemistries of both the cap and fill passes to be determined and reveal the difference of the two different welding wires. Combustion analysis was also used to determine the C, S, O and N on test samples cut from the cap and fill pass regions. The analysis of C and S was based on the combustion infrared detection technique, while the O and N were determined by means of infrared absorption and thermal conductivity.

The chemical compositions of the pipe steels and respective girth weld metals are listed in Table B3 and Table B4, along with calculated carbon equivalents. The small variations in pipe steel compositions are reflected in minor differences in CEs. The pipe steels had low C and N along with Mn, Ni, Cr, Cu, Nb and Ti additions.

The weld metal chemical compositions for the respective fill and cap passes of the two girth welds showed some small variations, evidenced by the differences in CE values. The differences between the cap and fill passes is directly related to the different chemistries of the consumable wires that were used for these passes. The weld metal of the fill passes has higher C, Mn, Si, and Mo, but lower Ni and O compared to the cap passes.

Table B3 Chemical compositions from the 16 mm – 16 mm WT welded pipe (Weld 236 (Weld-1))

Element wt. %	Grade 483 (API 5L X70) Pipe		Weld 236 (Weld-1)	
	16 mm	16 mm	Fill	Cap
C	0.078	0.071	0.103	0.08
Mn	1.44	1.49	1.79	1.37
Si	0.14	0.15	0.62	0.43
S	<0.001	<0.001	<0.001	<0.001
P	0.011	0.013	0.009	0.007
Ni	0.23	0.24	0.8	1.64
Cr	0.14	0.15	0.03	0.03
Mo	0.009	0.009	0.27	0.08
Cu	0.24	0.24	0.1	0.08
Al	0.034	0.033	0.008	0.003
Nb	0.041	0.051	0.006	0.013
V	0.005	0.005	0.012	0.023
Ti	0.013	0.014	0.03	0.05
N	0.003	0.004	0.005	0.005
O	-	-	0.066	0.118
CE_{IIW}	0.38	0.38	0.52	0.45
P_{cm}	0.17	0.17	0.23	0.19
CEN	0.26	0.25	0.38	0.28

$CE_{IIW} = C + Mn/6 + (Cr+Mo+V)/5 + (Ni + Cu)/15$

$P_{cm} = C + Si/30 + (Mn+Cu+Cr)/20 + Ni/60 + Mo/15 + V/10 + 5B$

$CEN=C+A(C)*(Si/24+Mn/6+Cu/15+Ni/20+(Cr+Mo+Nb+V)/5+5*B)$

where $A(C)= 0.75 + 0.25\tanh\{(20(C-0.12)\}$

Table B4 Chemical compositions from the 16 mm – 19 mm WT welded pipe (Weld 233 (Weld-2))

Element wt. %	Grade 483 (API 5L X70) Pipe		Weld 233 (Weld-2)	
	16 mm	19 mm	Fill	Cap
C	0.072	0.065	0.099	0.065
Mn	1.5	1.51	1.62	1.34
Si	0.15	0.15	0.51	0.38
S	0.008	0.006	0.007	0.006
P	0.011	0.012	0.012	0.009
Ni	0.24	0.23	0.74	1.93
Cr	0.15	0.16	0.04	0.04
Mo	0.009	0.011	0.23	0.04
Cu	0.23	0.23	0.12	0.03
Al	0.033	0.035	0.008	0.005
Nb	0.048	0.043	0.018	0.028
V	0.004	0.004	0.01	0.024
Ti	0.013	0.014	0.025	0.05
N	0.004	0.004	0.007	0.004
O	-	-	0.069	0.095
CE_{IIW}	0.39	0.38	0.48	0.44
P_{cm}	0.17	0.16	0.22	0.17
CEN	0.25	0.24	0.34	0.26

$CE_{IIW} = C + Mn/6 + (Cr+Mo+V)/5 + (Ni + Cu)/15$

$P_{cm} = C + Si/30 + (Mn+Cu+Cr)/20 + Ni/60 + Mo/15 + V/10 + 5B$

$CEN=C+A(C)*(Si/24+Mn/6+Cu/15+Ni/20+(Cr+Mo+Nb+V)/5+5*B)$

where $A(C)= 0.75 + 0.25\tanh\{(20(C-0.12)\}$

B.3 Base Metal Strap Tensile Tests

Base metal strap tensile specimens were machined by waterjet from blanks per the machine drawing in Figure B4 and are shown prepared for testing in the photograph shown in Figure B5.

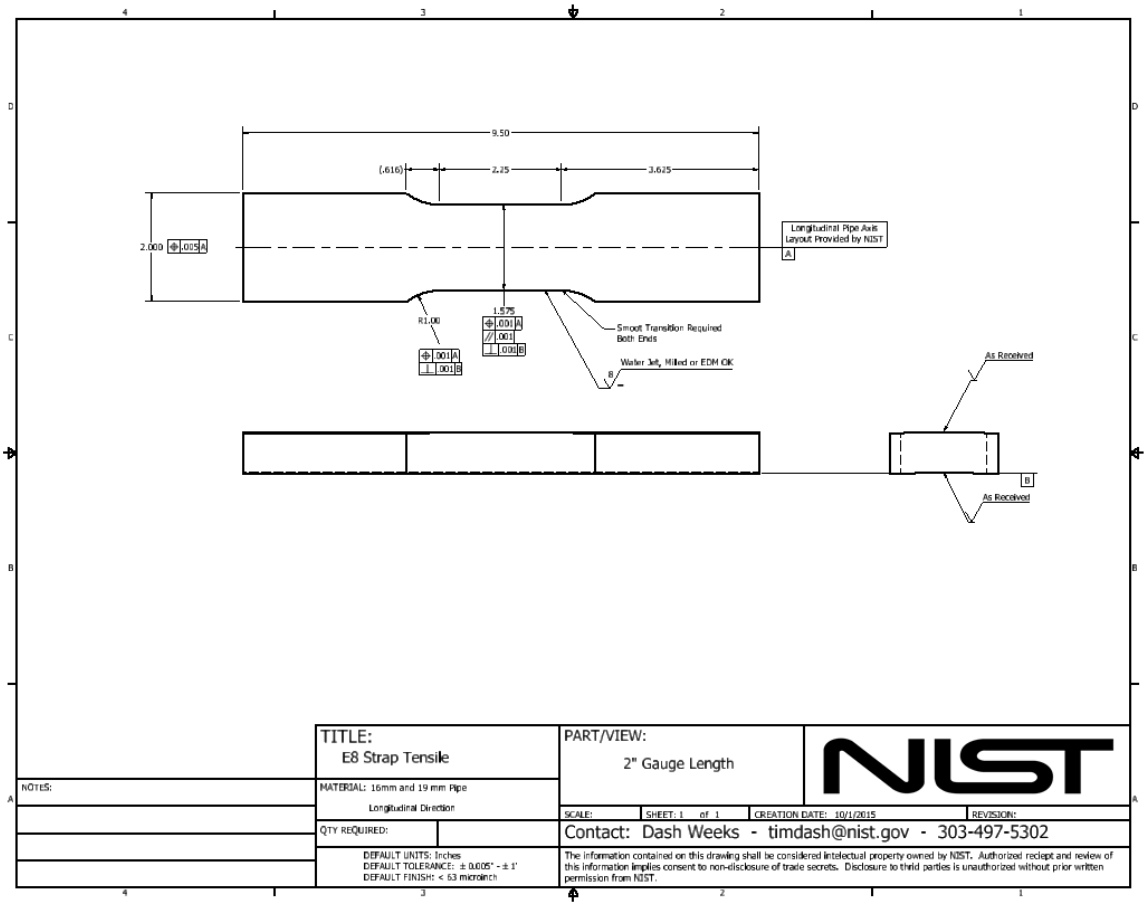

Figure B4 Machine drawing of base metal strap tensile specimens

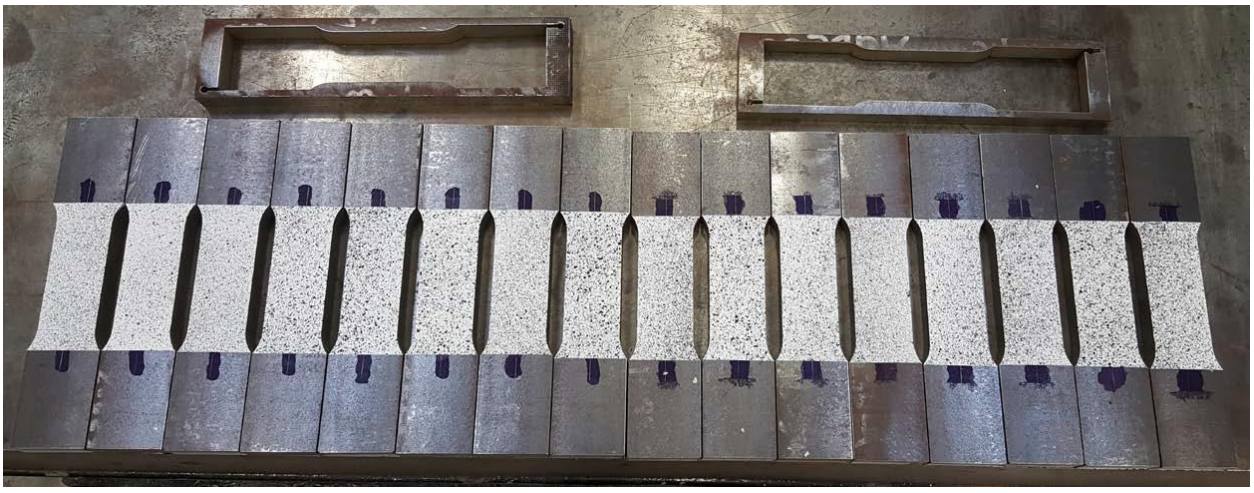

Figure B5 Photograph of base metal strap tensile specimens prepared for testing, each specimen was speckled for digital image correlation.

Base metal strap tensile tests were performed according to ASTM E8/8M: *Standard Test Methods for Tension Testing of Metallic Materials.* The tests were performed in displacement control at a rate of 1 mm/min and was maintained until failure of each specimen. A class B2 extensometer with a 50.8 mm (2 in) gauge length was installed on each specimen. The extensometer was installed on the flat edges (reduced section) of the specimen. Each specimen was tested in a servo-hydraulic universal test frame equipped with hydraulic wedge grips. The cross-sectional area was taken as the average of five chord width measurements by use of digital calipers in the reduced section multiplied by the average of five thickness measurements taken along the axial centerline of the specimen by use of a digital micrometer equipped with spherical anvils. The difference in area calculated from chords and arcs is not significantly different than that by assuming a rectangular cross-section considering measurement resolution and uncertainty of the digital calipers and micrometer. Three dimensional (3D) Digital image correlation (DIC) was also employed on each of the specimens. The data were used to validate the extensometer data and to identify anomalous strain distributions. No anomalies were detected and the DIC data were commensurate with the extensometer data. Therefore, DIC results are not presented in this report.

B.4 Base Metal Round Bar Tensile Tests

Base metal round tensile specimens were machined from blanks according to the machine drawings shown in Figure B6 and Figure B7.

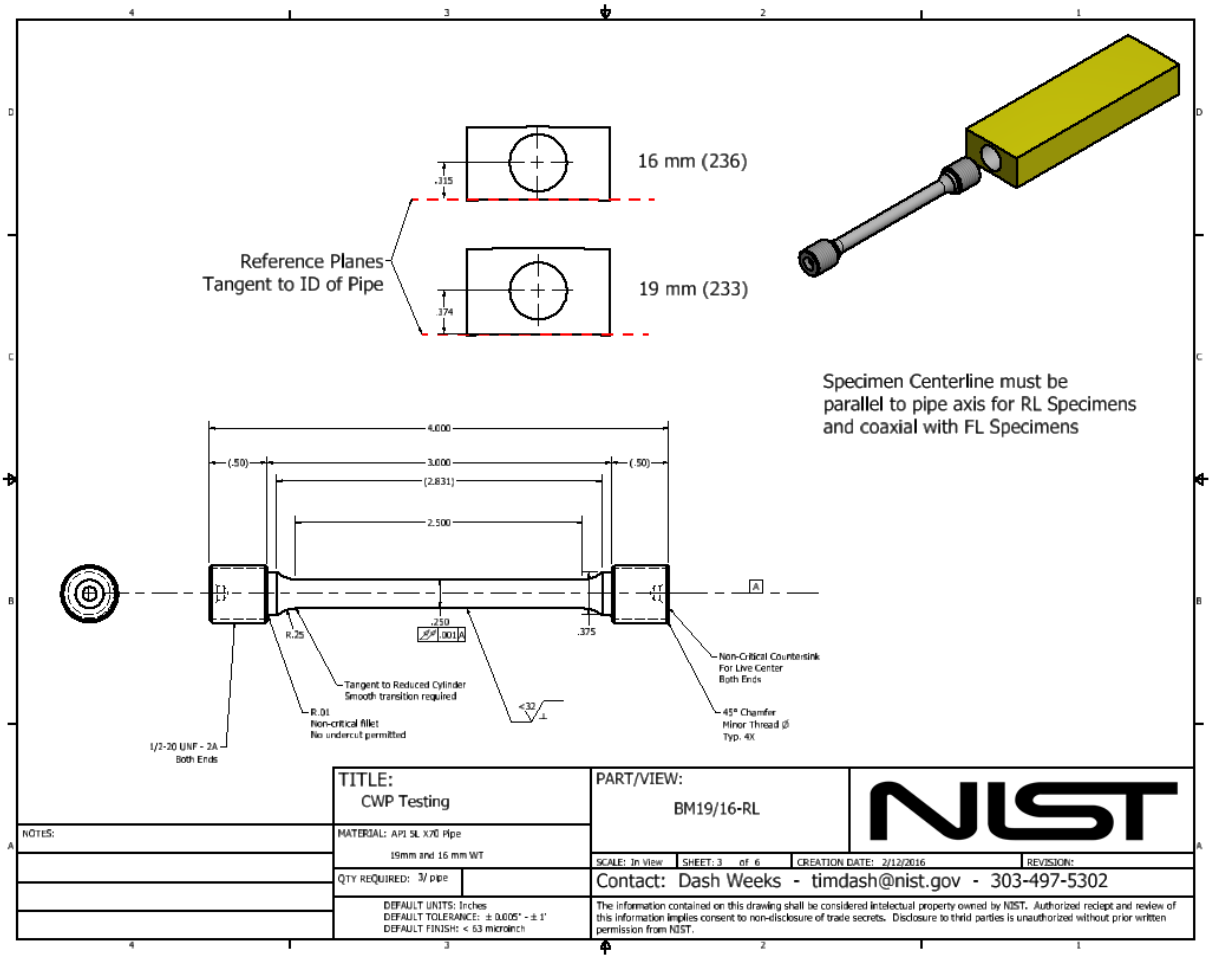

Figure B6 Machine drawing of base metal longitudinal round tensile specimens

Base metal round tensile tests were performed according to ASTM E8/8M. The tests were performed in displacement control at a rate of 0.8 mm/min and was maintained until failure of each specimen. A class B2 extensometer with a 50.8 mm (2 in) gauge length was installed on each specimen. Each specimen was tested in a servo-hydraulic universal test frame equipped with threaded connections and a universal joint to reduce specimen bending. The cross-sectional area was calculated from the average of five diameter measurements along the reduced gauge section of each specimen by use of a micrometer equipped with flat anvils.

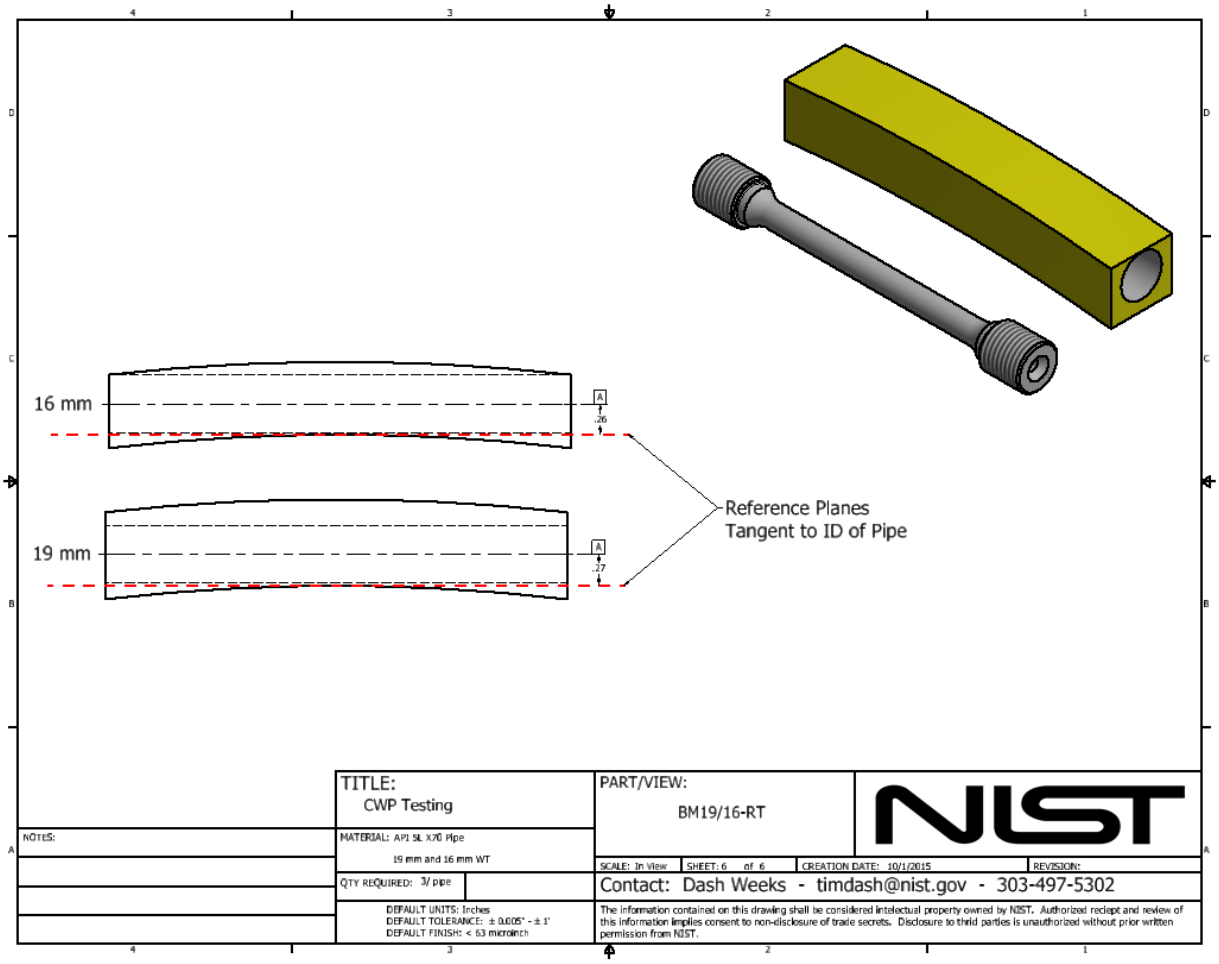

Figure B7 Machine drawing of base metal transverse round tensile specimen sectioning, the specimen was machined according to dimensions already provided.

B.5 All Weld Metal Round Bar Tensile Tests

Weld metal round tensile specimens were machined by engine lathe from blanks according to the machine drawings in Figure B8 and Figure B9.

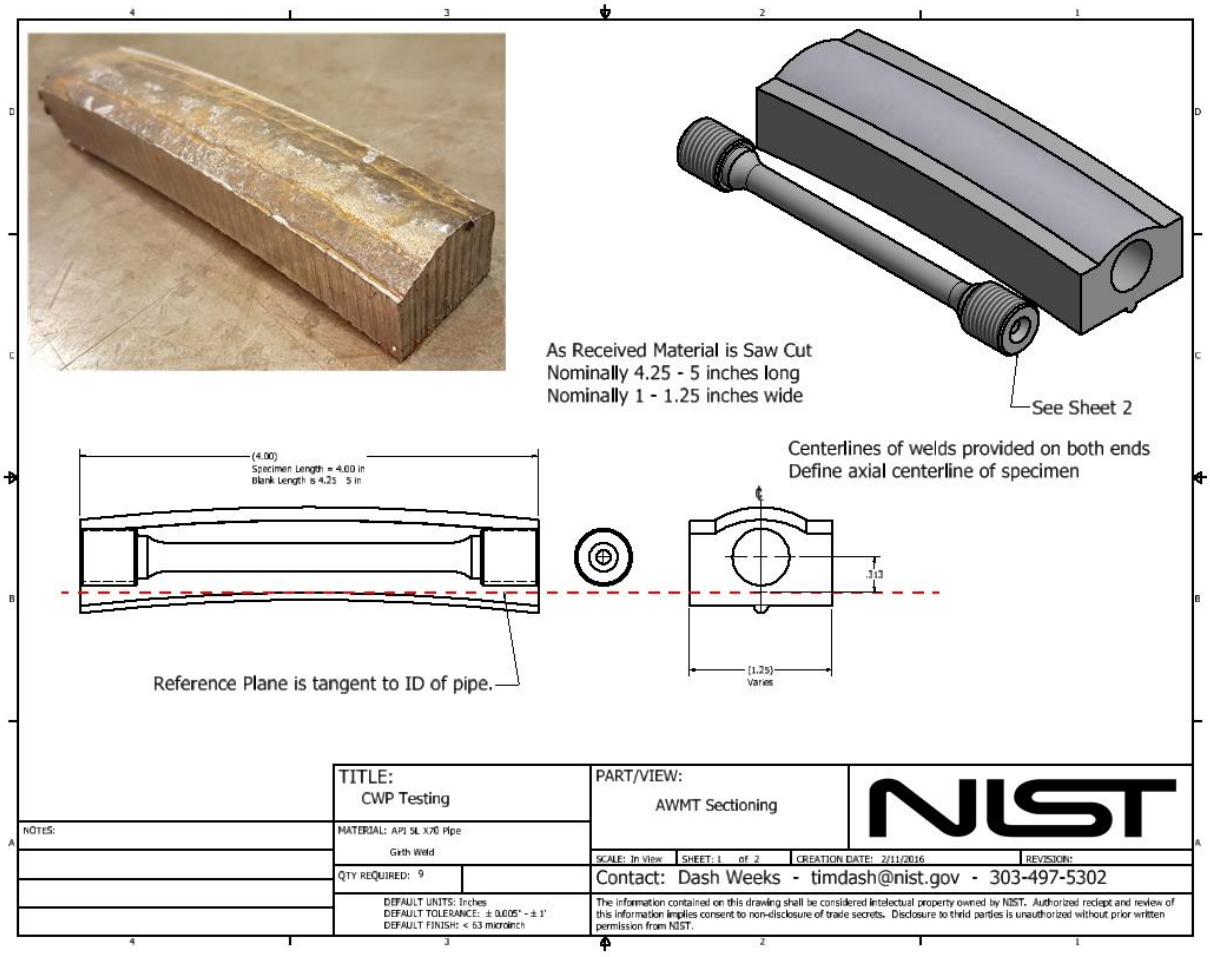

Figure B8 Machine drawing of weld metal round tensile specimen sectioning

Weld metal round tensile tests were performed according to ASTM E8/8M. The tests were performed in displacement control at a rate of 0.8 mm/min and was maintained until failure of each specimen. A class B2 extensometer with a 50.8 mm (2 in) gauge length was installed on each specimen. Each specimen was tested in a servo-hydraulic universal test frame equipped with threaded connections and a universal joint to reduce specimen bending. The cross-sectional area was calculated from the average of five diameter measurements along the reduced gauge section of each specimen by use of a micrometer equipped with flat anvils.

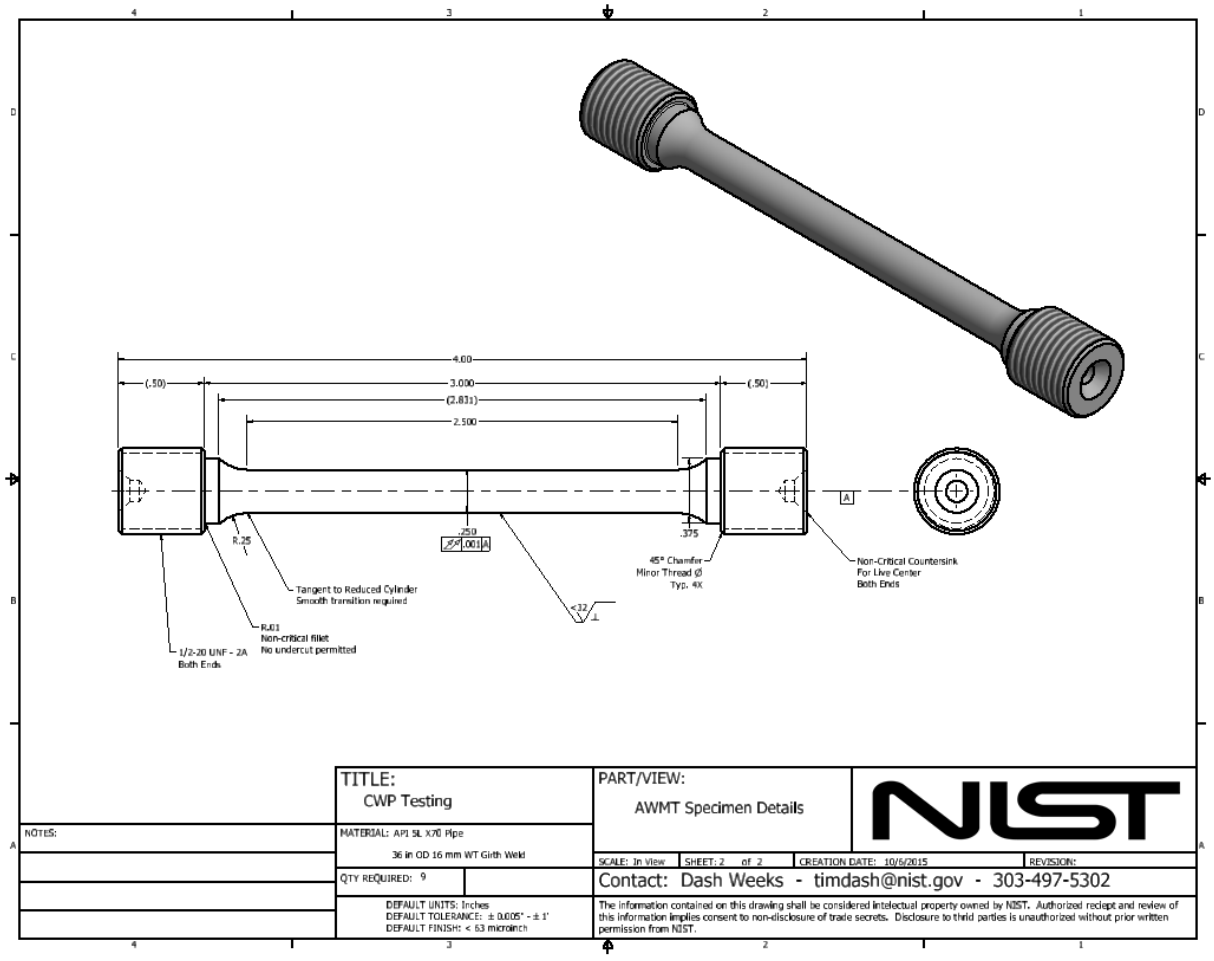

Figure B9 Machine drawing of weld metal round tensile specimen dimensioning.

B.6 Metallography and Microhardness Tests

Four full-thickness sections were cut from pieces adjacent to each of the CWP specimens (i.e., different clock positions) to characterize the two multi-pass girth pipe welds. The metallographic specimens were sectioned to allow the entire weldment to be evaluated. Each specimen was mounted in epoxy, and after initial grinding they were prepared by use of automated polishing techniques. The specimens were etched in a 2 % Nital solution to reveal details of the microstructures of the pipe base metal, heat affected zone (HAZ) and weld metal (WM). With multiple full cross-sections of the girth welds, the variations in the fusion line profile, and microstructural details were characterized by light optical microscopy.

A light optical microscope (LOM) was used to create high-quality digital macrographs of each weld section. This required a series of micrograph images taken at 25X magnification and compiled using the mosaic option available with the LOM and dedicated software package.

A series of digital micrographs were taken at a range of higher magnifications to characterize different regions within the pipe girth welds, as shown in Figure B10**.** The locations of interest

included the as-deposited weld metal of the cap passes, general microstructures near the Charpy notch positions, *i.e.*, WMC CVN and HAZ CVN locations. Additional images were obtained from the mid-wall pipe steel base metal and in the area for the targeted EDM notches (HAZ CWP and WMC CWP) to be cut from the ID of selected CWP pipe girth weld specimens.

Microhardness testing was performed to characterize the girth welds by completing a through-thickness scan at the WMC and three cross-weld traverses that were biased to the OD, mid-thickness, and ID, as illustrated in Figure B11. The microhardness testing was performed by used of a Vickers diamond pyramid indenter with a 300g load and nominal spacing of ~500 μm between adjacent indents.

Representative macrographs of full-thickness sections cut from different clock positions of the respective girth welds are shown in Figure B12 and Figure B13. The images provide detail of the weld joint high-low misalignment, weld pass sequences, fusion line profile, variation in weld metal as-deposited and reheated regions and the extent of the HAZ. The images also provide some further detail of the variations that may be encountered in the placement of notches for CVN specimens, (which were just below the cap passes), and the targeted notch tip (into the hot/fill passes) for both the SE(T) and CWP specimens. In the latter case, Figure B15 and Figure B16 show details of the targeted notch positions, including the structures of the HAZ near the fusion line and WM just beneath the first fill pass.

Representative optical micrographs in Figure B16 show that the X70 pipe steel microstructure contains a mixture of phases with some banded regions evident. The narrow-elongated grains composed of irregular ferrite/granular bainite have transformed from pancaked austenite. While equiaxed/ polygonal ferrite grains also formed along with some degenerate pearlite as shown in the high magnification image presented in Figure B16(b).

The cap pass as-deposited microstructure is shown in Figure B17. Since these passes were deposited with a different wire (slightly different chemistry) than the underlying fill passes it was the first region to be characterized. The microstructure in the final cap pass was very fine and dominated by a high fraction of acicular ferrite with some very limited discontinuous grain boundary ferrite and ferrite-with-second phase (bainite).

The girth weld multi-pass welding procedure resulted in through-thickness variation in the proportion of as-deposited and reheated weld metal because of the two-pass per layer fill pass sequence. This was important in terms of the location of the weld metal CVN specimen, which was notched at the centerline and therefore sampled a mixture of as-deposited and reheated weld metal, as shown in Figure B18(a). Figure B18(b) shows the microstructure at 1/3 thickness of the CVN specimen, while Figure B19, reveals the structure at 1/2 thickness of the CVN specimen. In both cases, a fine, mainly acicular ferrite microstructure was observed even in what appears to be coarse grain reheated WM.

The weld metal microstructures of the hot and root passes were also characterized. The upper portion of the hot pass exhibited a reheated structure that was formed from deposition of the first fill pass. In this case, an inter-critically reheated weld metal microstructure (with dark etching phase delineating prior austenite grains) was obtained, as shown in Figure B20. The grain interiors had more course acicular ferrite with occasional polygonal ferrite grains. The root pass

weld metal consisted of a more course acicular ferrite microstructure with some grain boundary and polygonal ferrite also present, as shown in Figure B21.

The heat affected zone (HAZ) microstructures near the targeted notch position of the CVN and CWP specimens were also evaluated. For the CVN location, the HAZ adjacent to the fusion line consisted of both single and multiple cycled regions, as evident in Figure B22. The grain coarsened (GC) HAZ exhibited relatively coarse prior austenite grains with packets of fine and coarse bainite, as shown in Figure B23. In the ½ thickness position of the CVN specimen, some inter-critically reheated GCHAZ was observed with the prior austenite grain boundaries partially delineated by a dark etching second phase, as shown in Figure B24. The overall microstructure appeared considerably coarser than the GCHAZ mentioned above, although deeper etching may have revealed more details of the bainitic-ferrite laths.

The final region to be characterized was the HAZ near the targeted notch of the CWP specimen. In this case, the area adjacent to the fusion line near the targeted 5 mm depth of the notch (from the ID) contained mainly reheated HAZ regions, as shown in Figure B25 and Figure B26. The variation in grain size is shown in Figure B25(b), while the detailed features of the microstructure are shown in Figure B26. The fine grained reheated HAZ structure consists of polygonal ferrite grains and bainite dispersed throughout the structure.

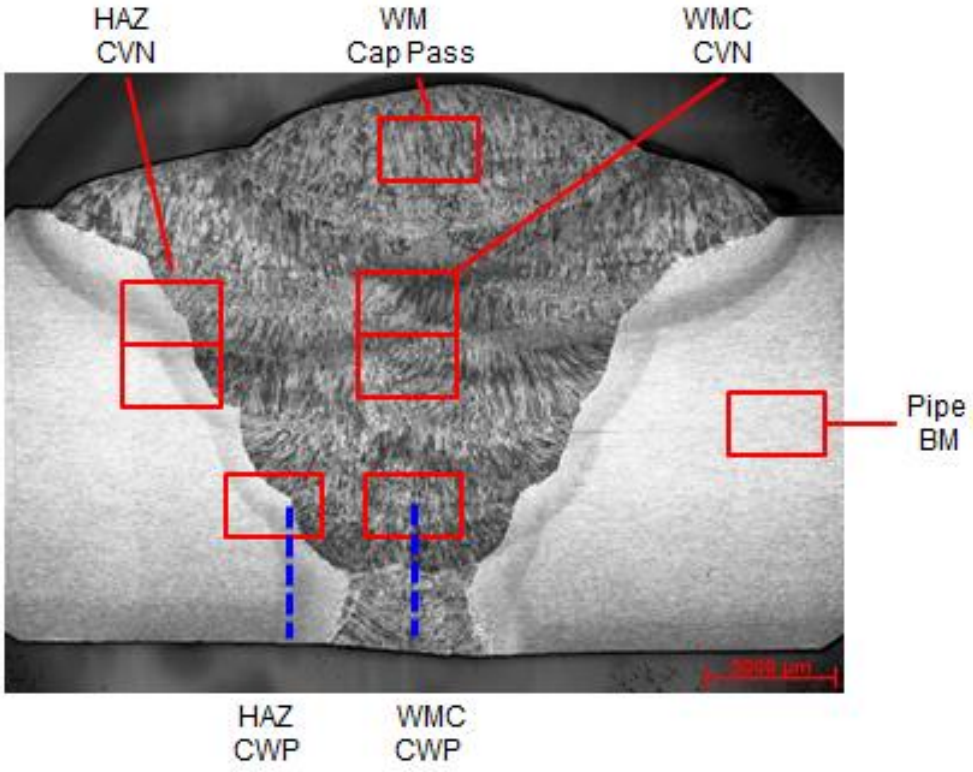

Figure B10 Locations (red rectangular boxes) of microstructural characterization of weld metal and HAZ regions for pipe girth Welds 236 and Weld 233 (Weld-2). Blue dashed vertical lines indicate targeted 5 mm location of notches in CWP for the HAZ and WMC.

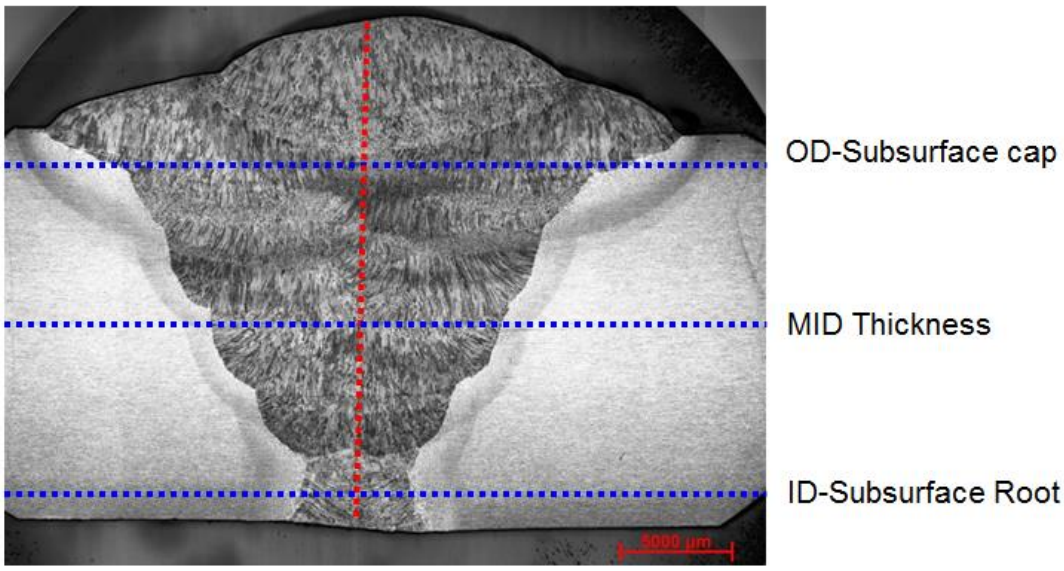

Figure B11 Locations (dashed blue lines) of cross weld microhardness traverses along with through-thickness (red dashed line) WMC traverse Welds 236 and Weld 233 (Weld-2).

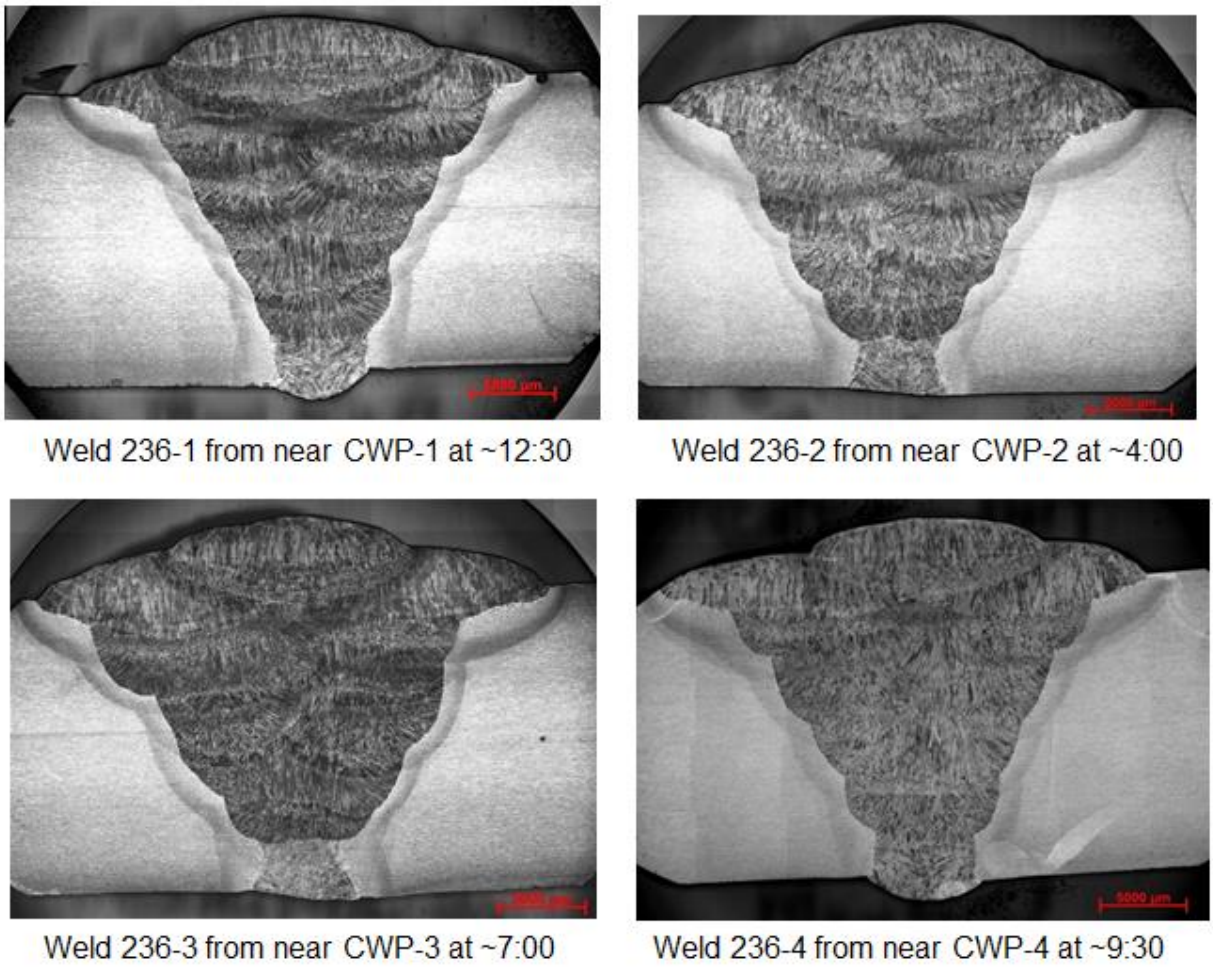

Figure B12 Macrographs of different sections cut from near CWP specimens in Weld 236 (Weld-1)

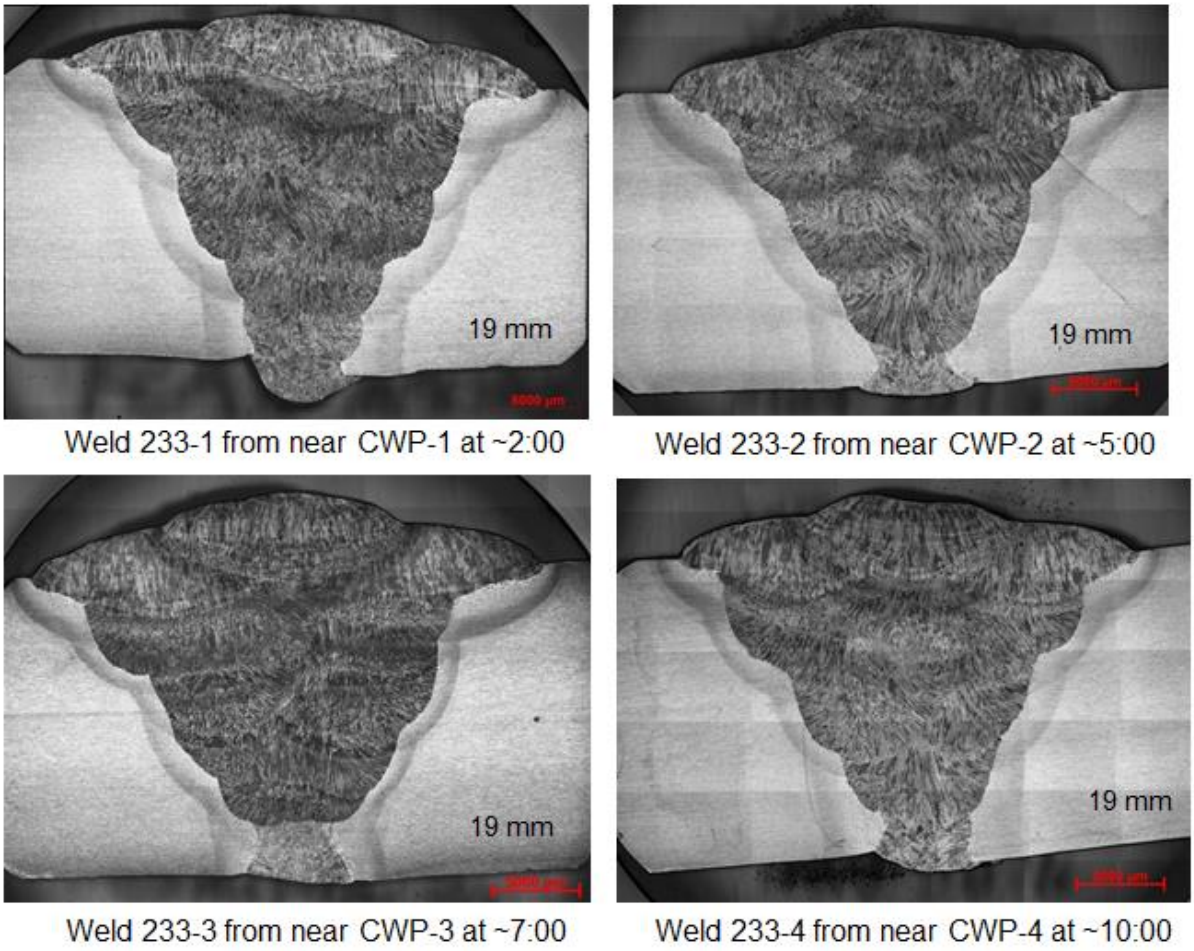

Figure B13 Macrographs of different sections cut from near CWP specimens in Weld 233 (Weld-2)

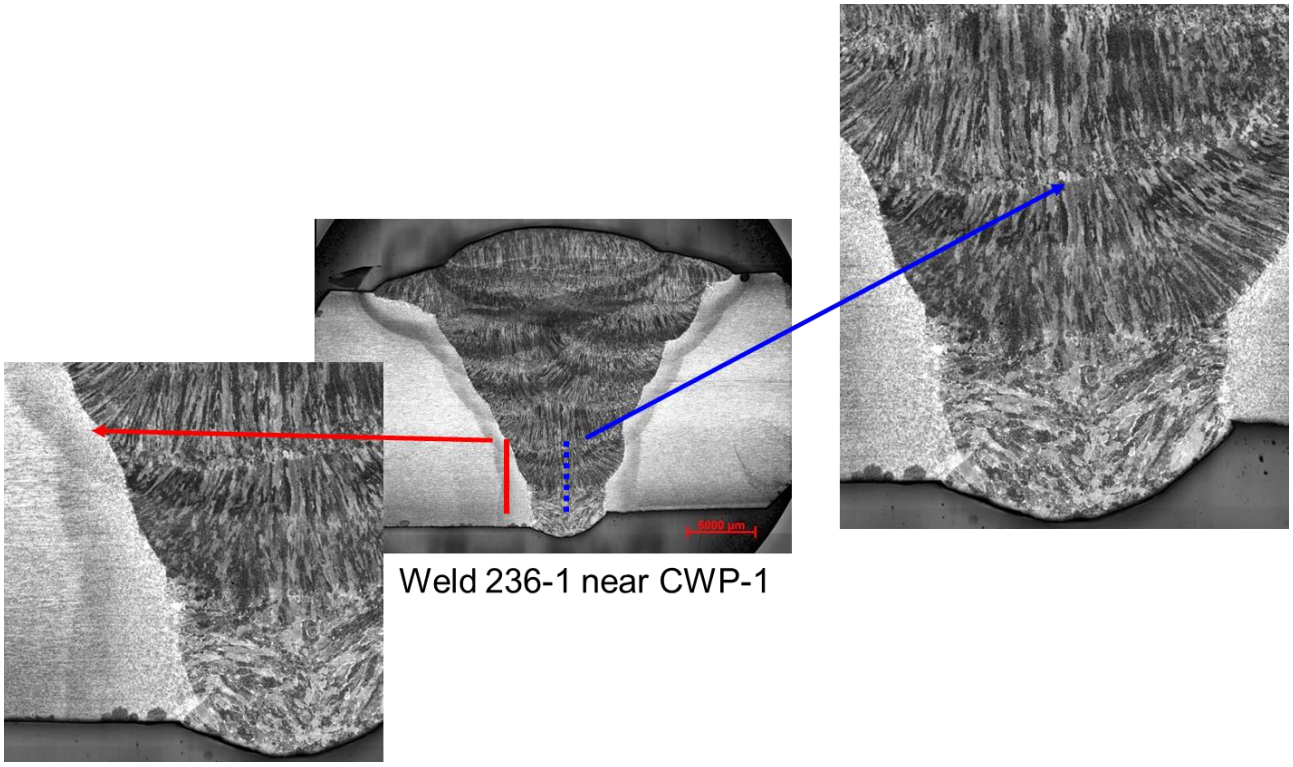

Figure B-14 Macrographs showing the targeted ID location (dashed red and blue vertical lines) of HAZ and WM flaws. Insert images show detail of HAZ and WM regions for CWP specimens from Weld 236 (Weld-1).

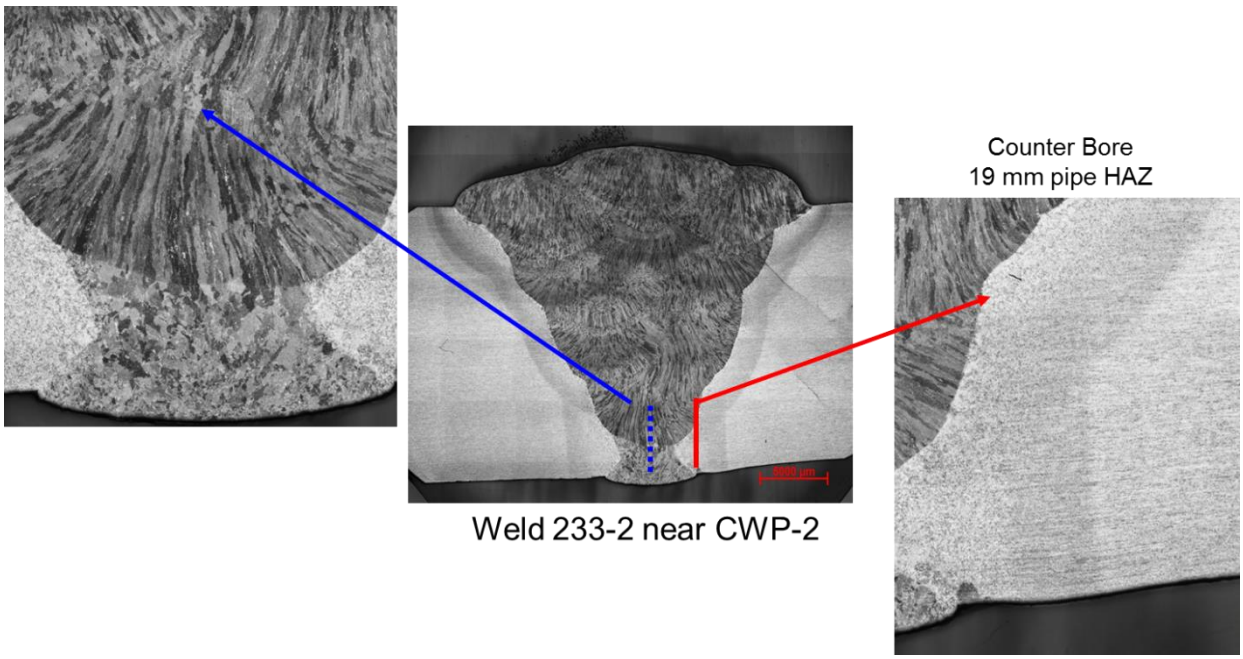

Figure B15 Macrographs showing the targeted ID location (dashed red and blue vertical lines) of HAZ and WM flaws. Insert images show detail of HAZ and WM regions for CWP specimens from Weld 233 (Weld-2).

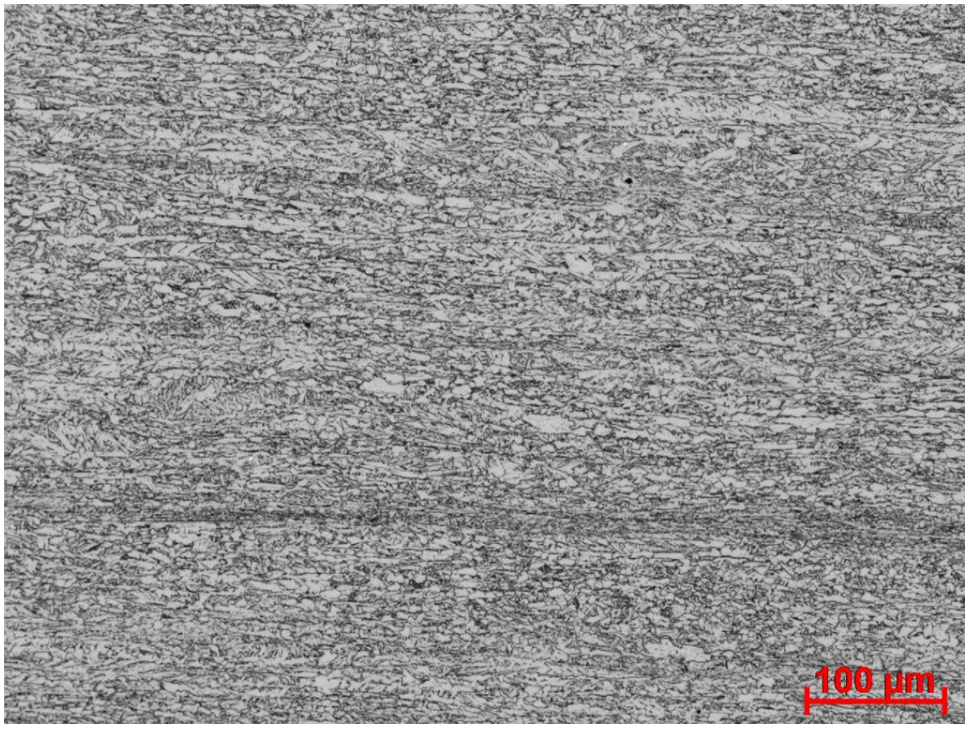

(a)

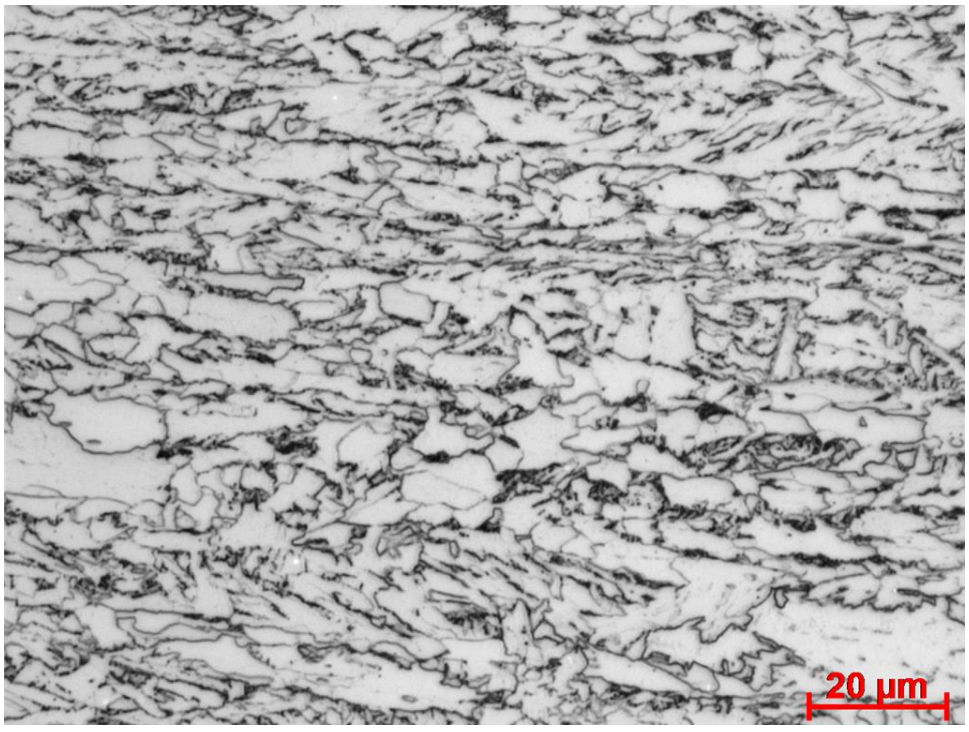

(b)

Figure B16 Microstructure of base metal at mid-thickness of cross-section of Weld-236-1

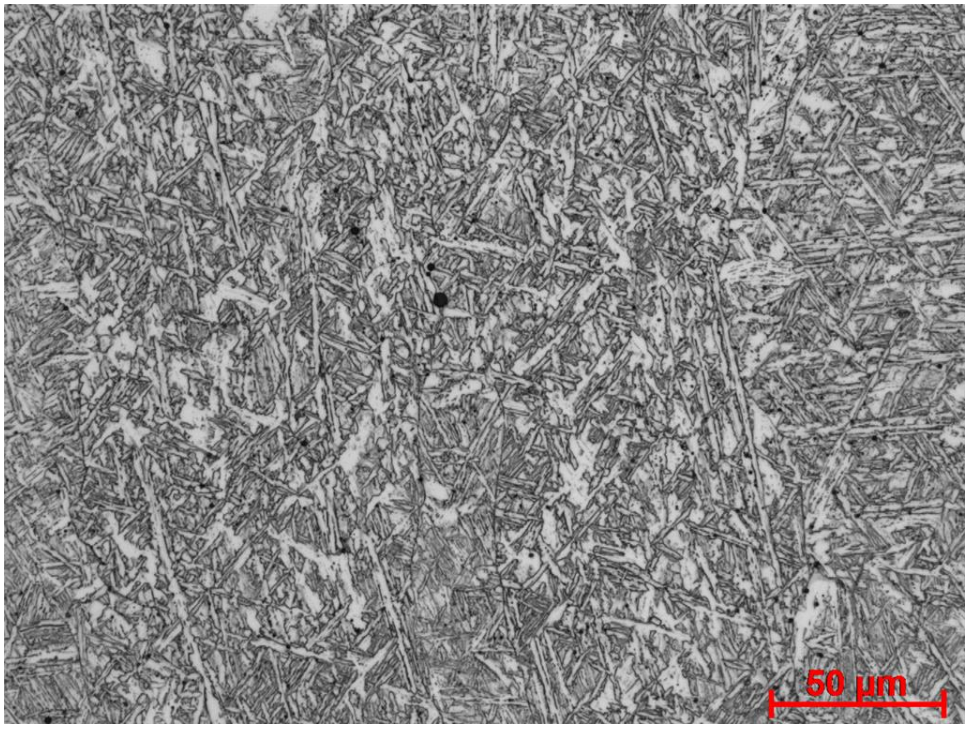

(a)

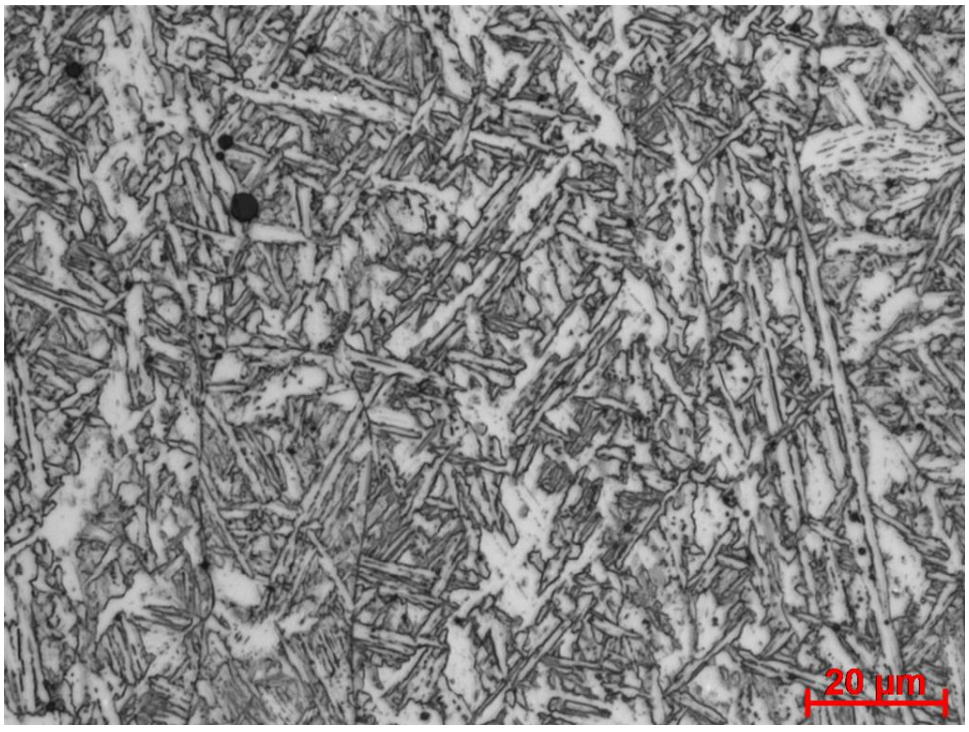

(b)

Figure B17 Microstructure of cap pass as-deposited region of Weld-236-1

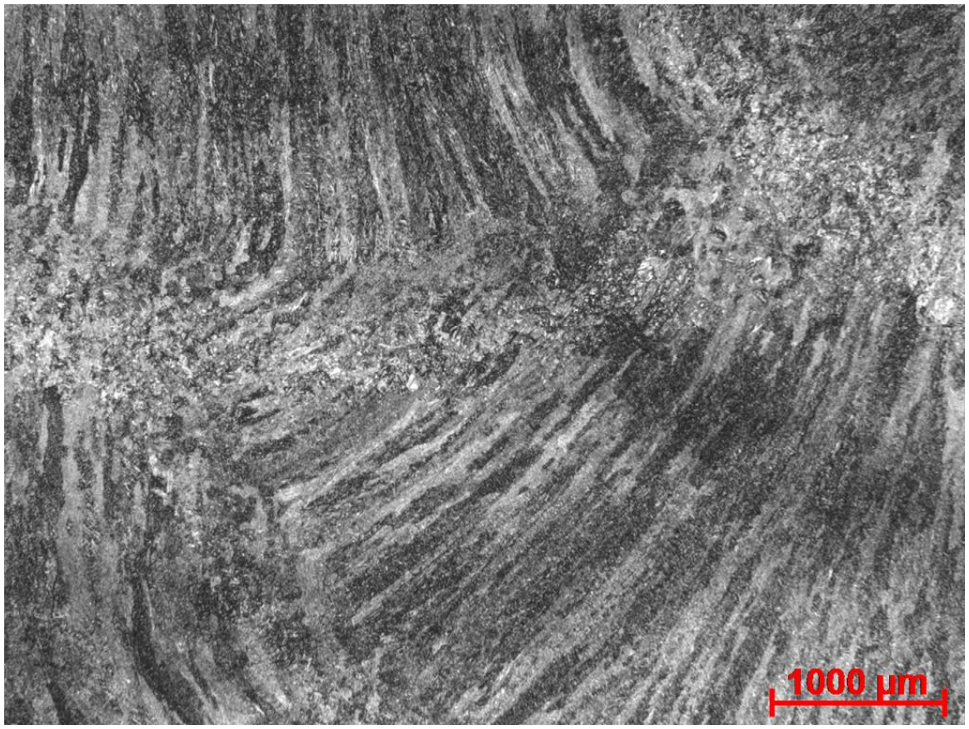

(a)

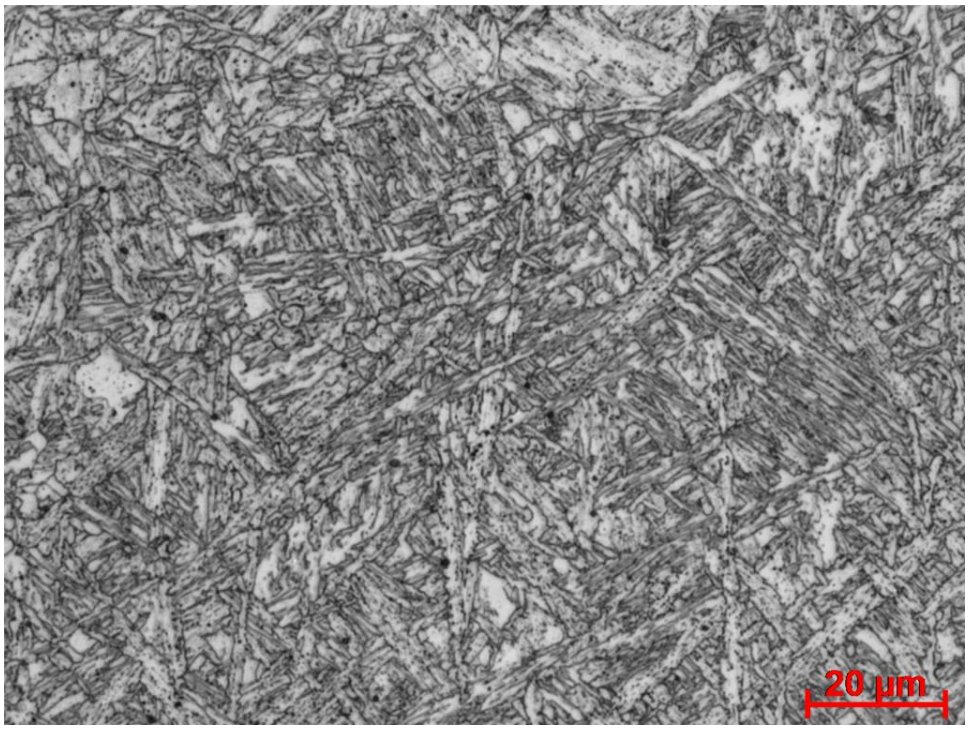

(b)

Figure B18 Weld metal microstructure at 1/3 thickness of CVN specimen for Weld-236-1

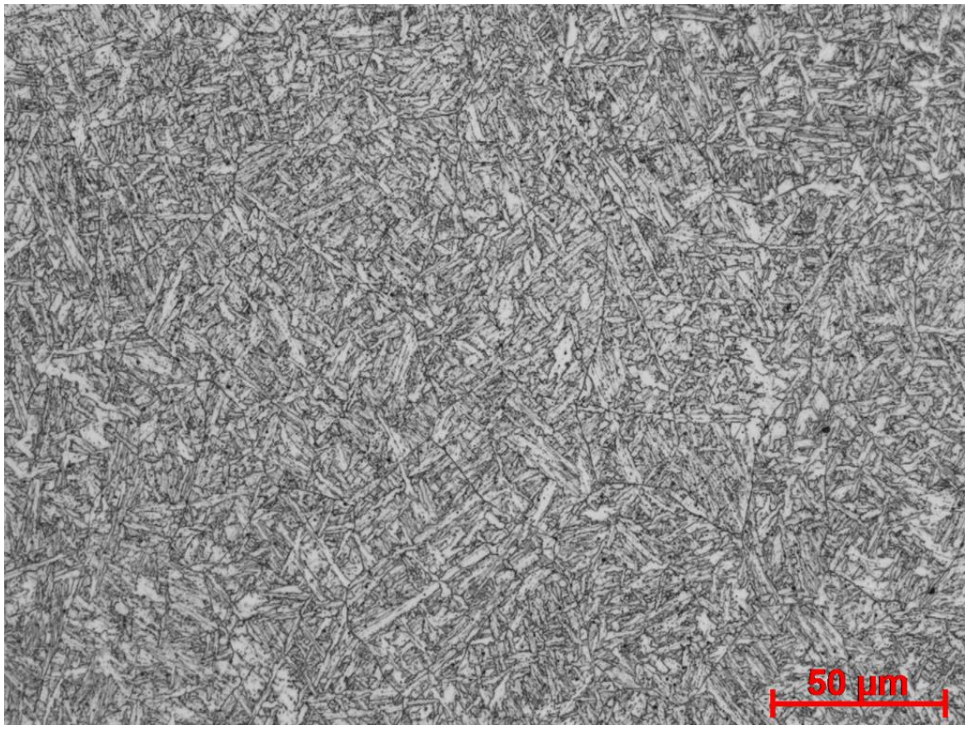

(a)

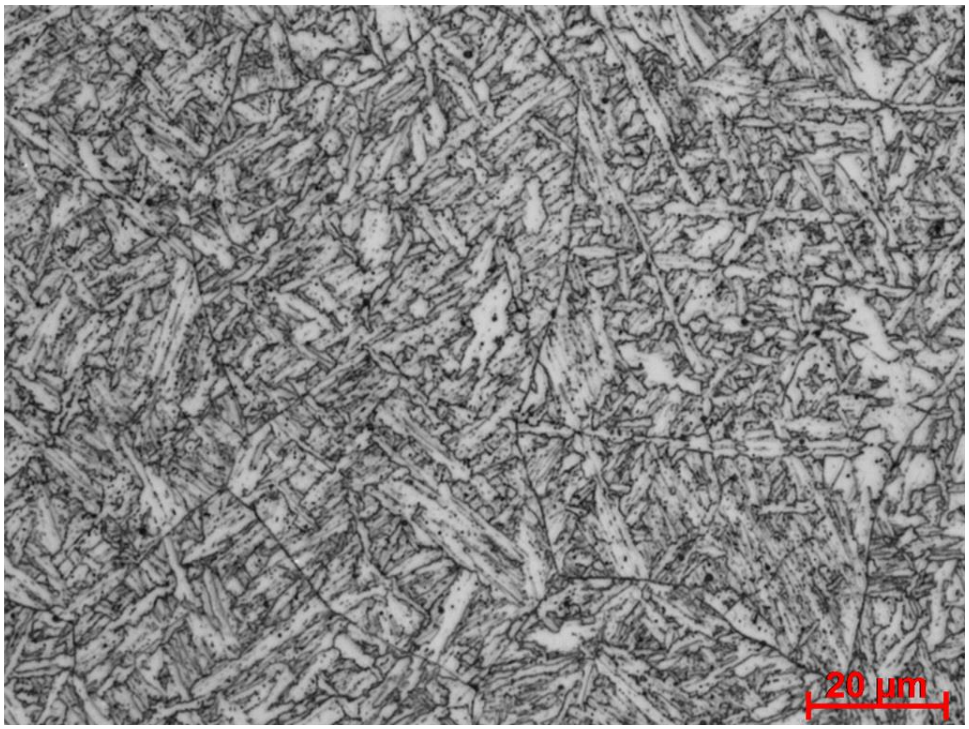

(b)

Figure B19 Weld metal microstructure at 1/2 thickness of CVN specimen for Weld-236-1

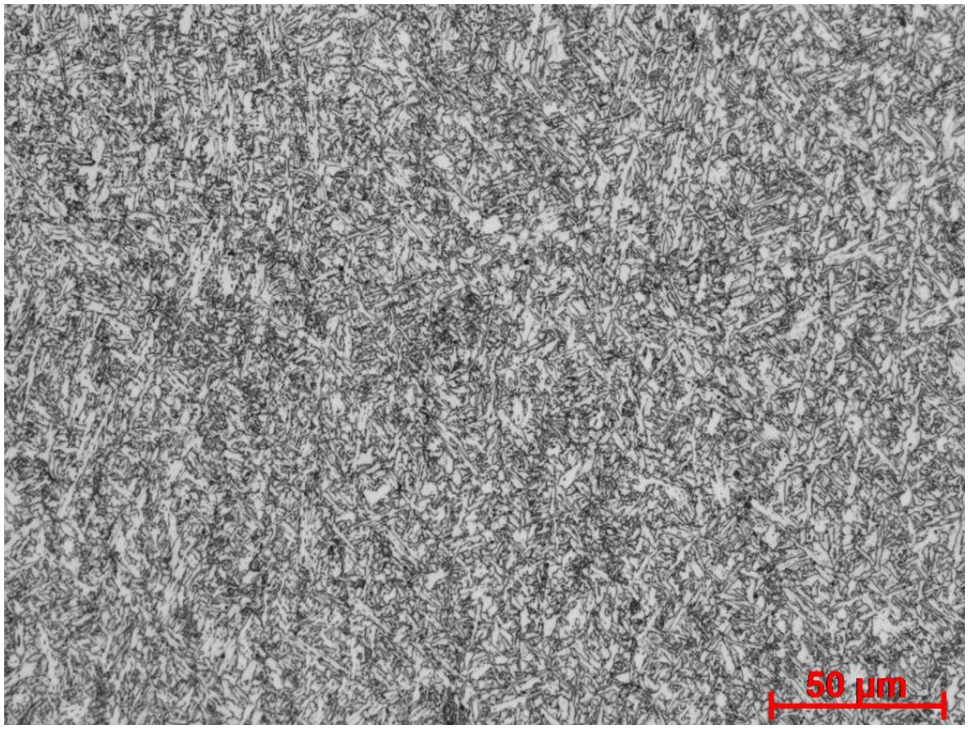

(a)

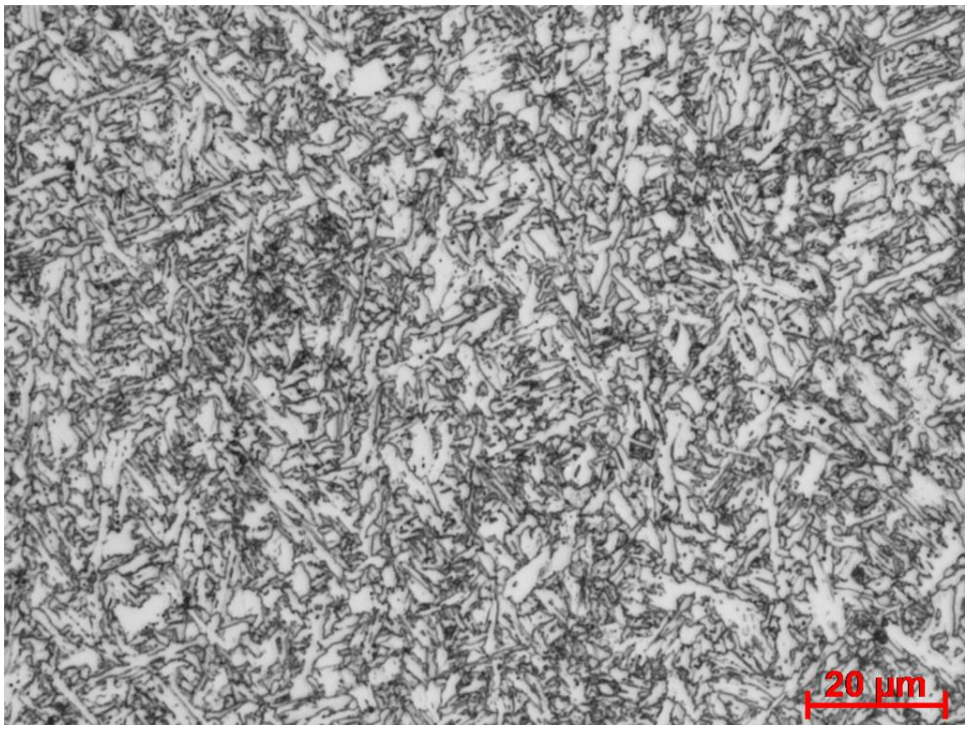

(b)

Figure B20 Microstructure of hot pass of cross-section of Weld-236-1

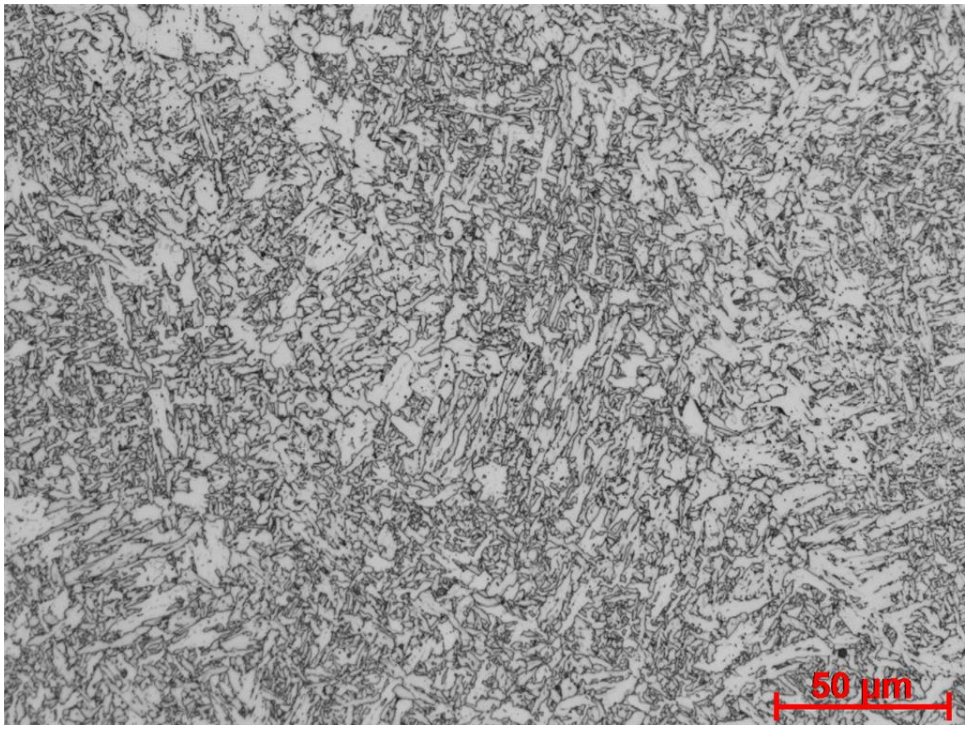

(a)

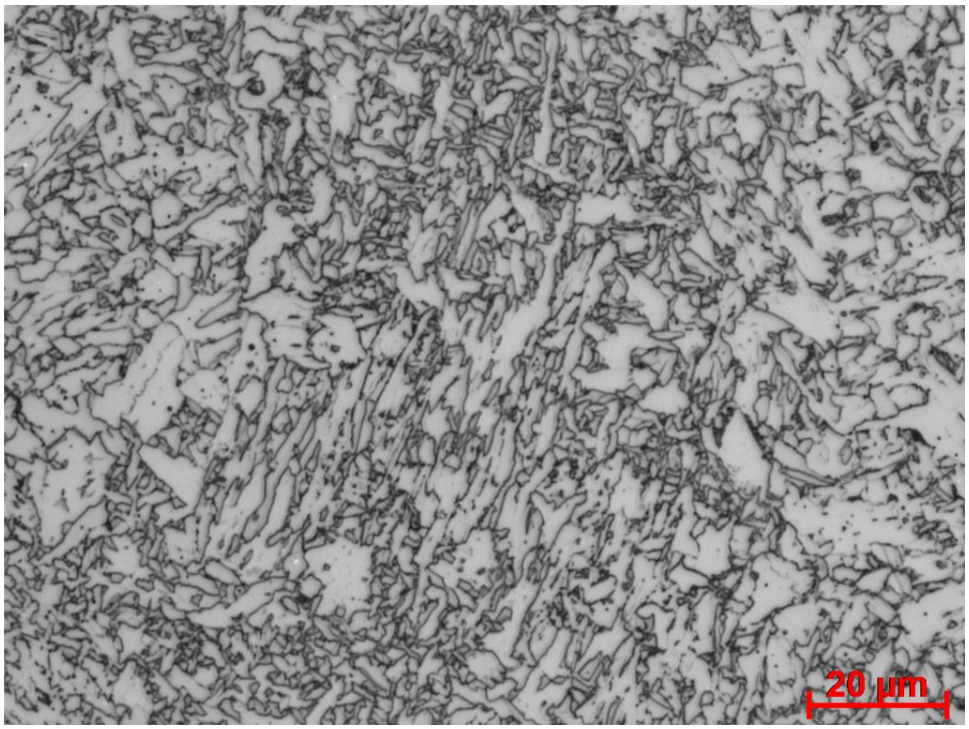

(b)

Figure B21 Microstructure of root pass region of cross-section of Weld-236-1

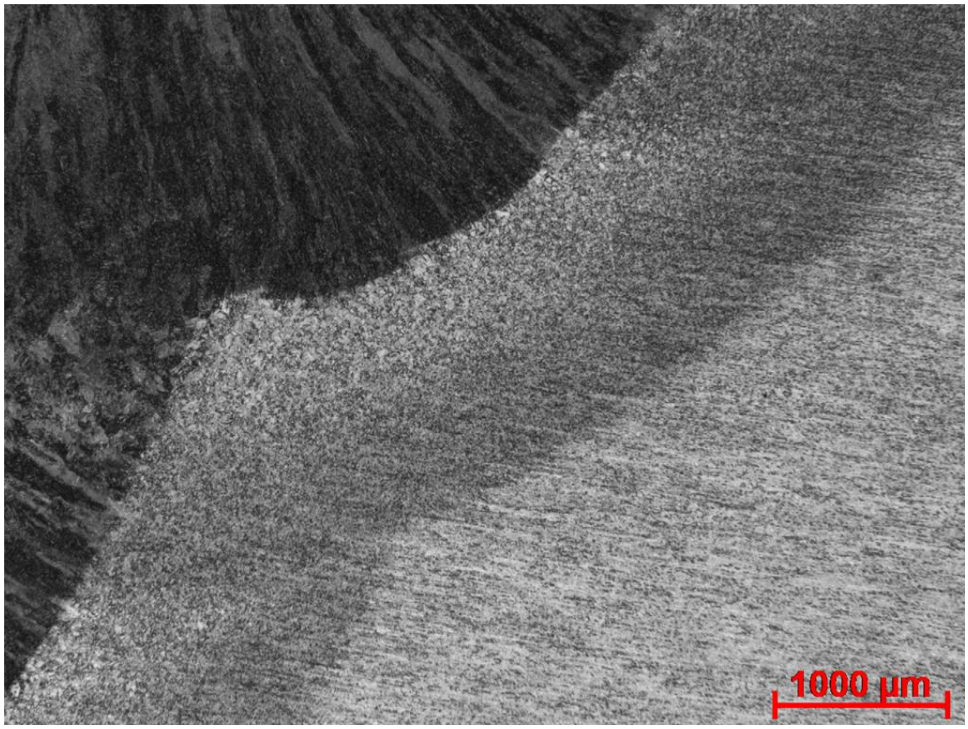

(a) 1/3 thickness of CVN specimen

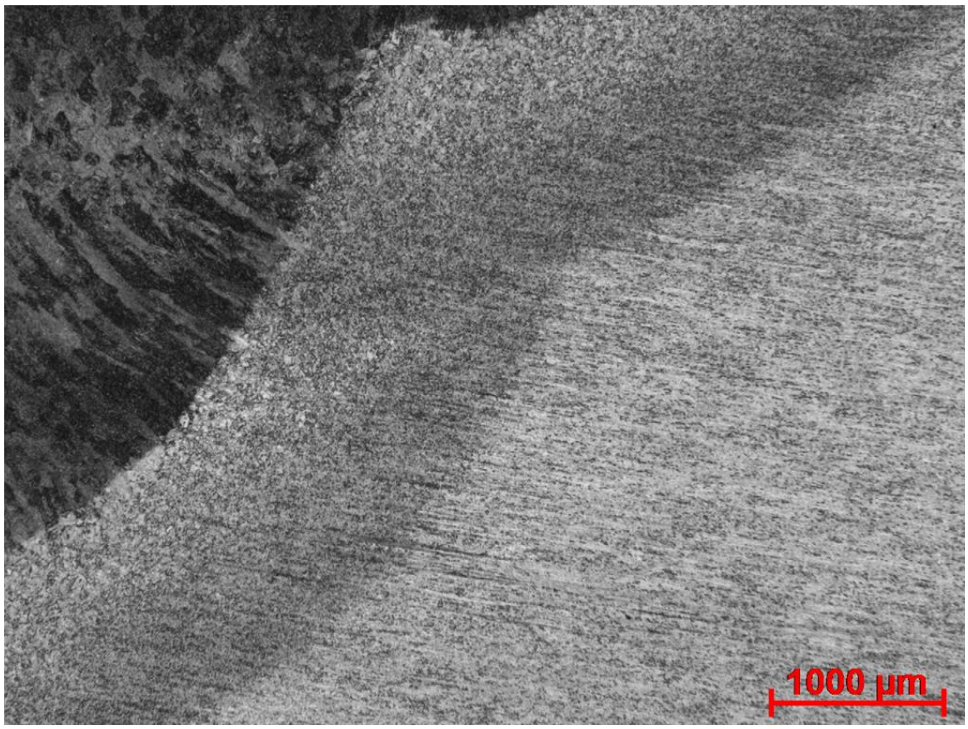

(b) 1/2 thickness of CVN specimen

Figure B22 HAZ microstructure in the vicinity of CVN specimen for Weld-236-1

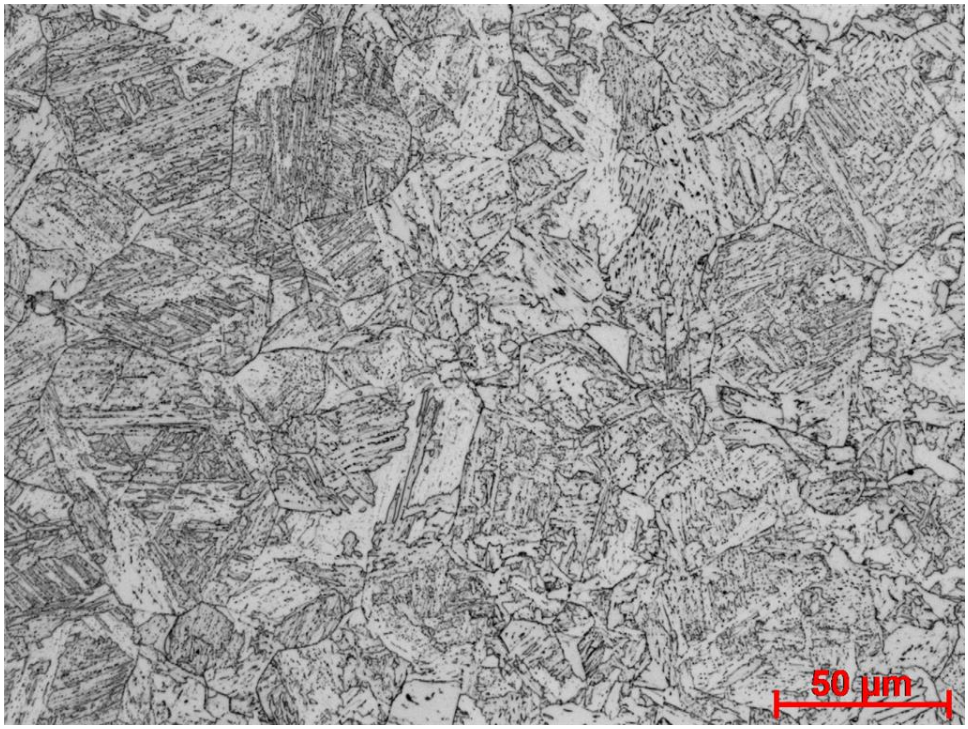

(a)

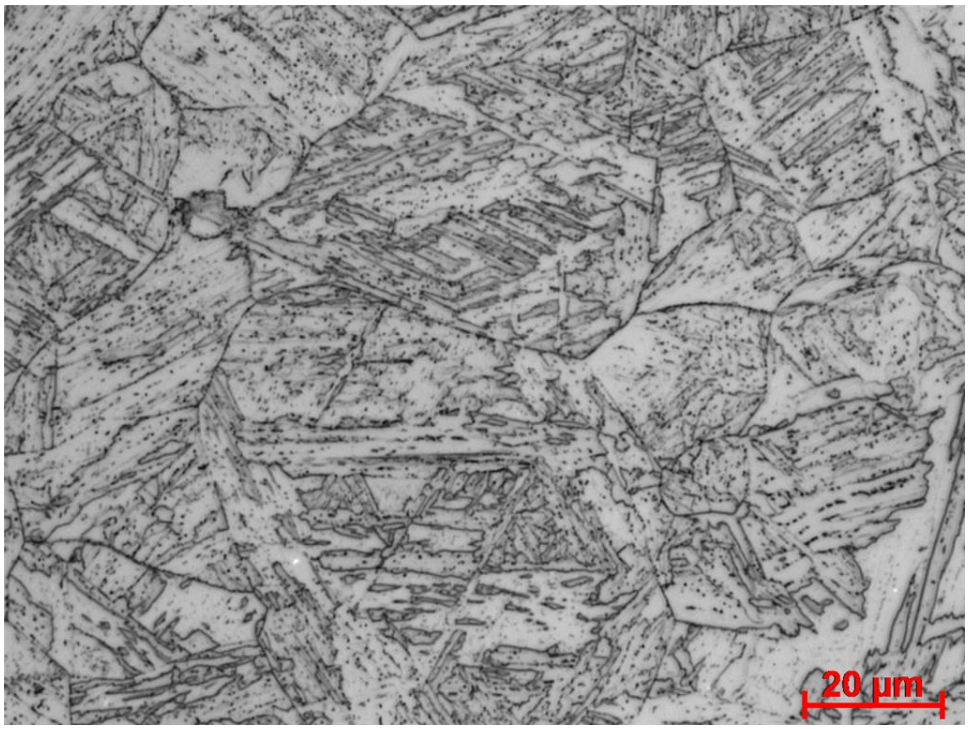

(b)

Figure B23 GCHAZ microstructure at 1/3 thickness of CVN specimen for Weld-236-1

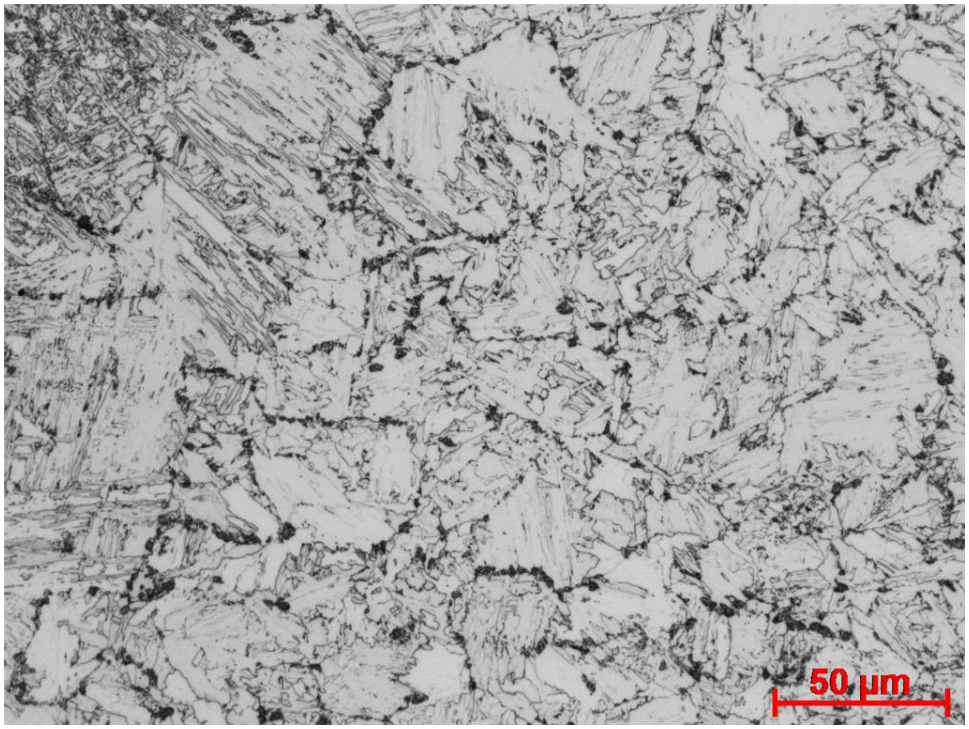

(a)

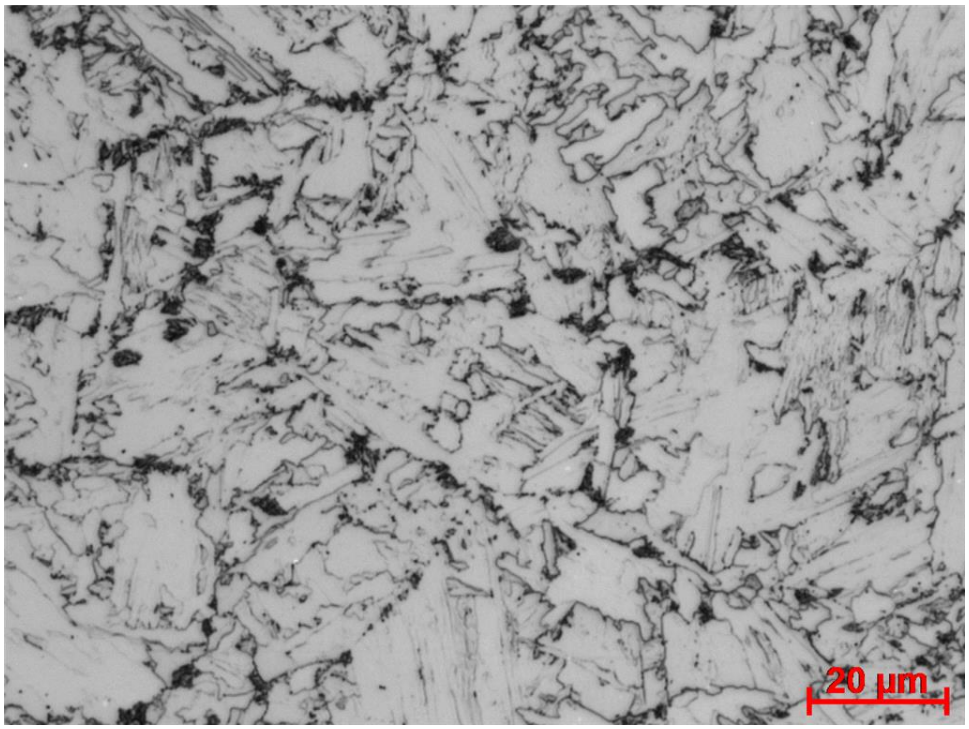

(b)

Figure B24 ICRGCHAZ microstructure at 1/2 thickness of CVN specimen for Weld-236-1

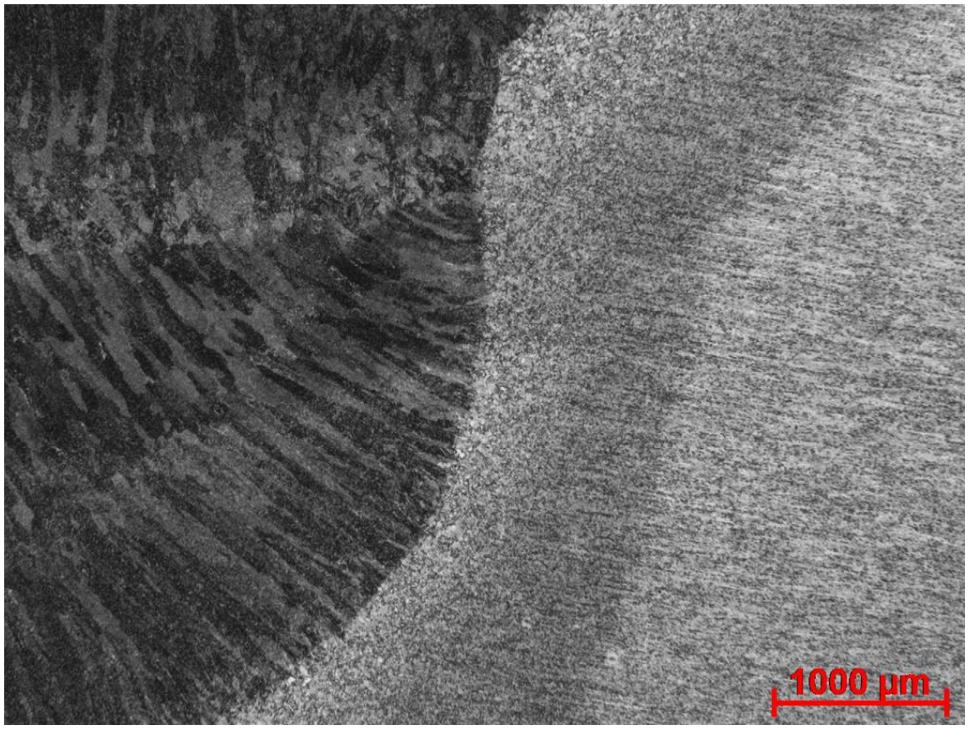

(a)

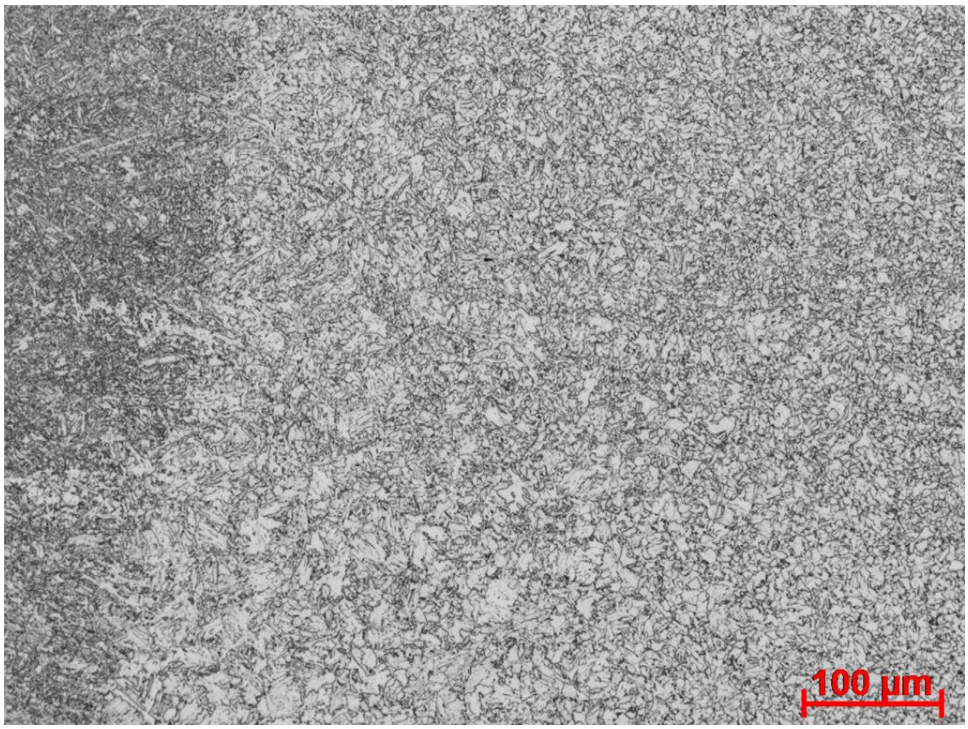

(b)

Figure B25 HAZ microstructure near 5 mm targeted notch depth for CWP from Weld 236-1

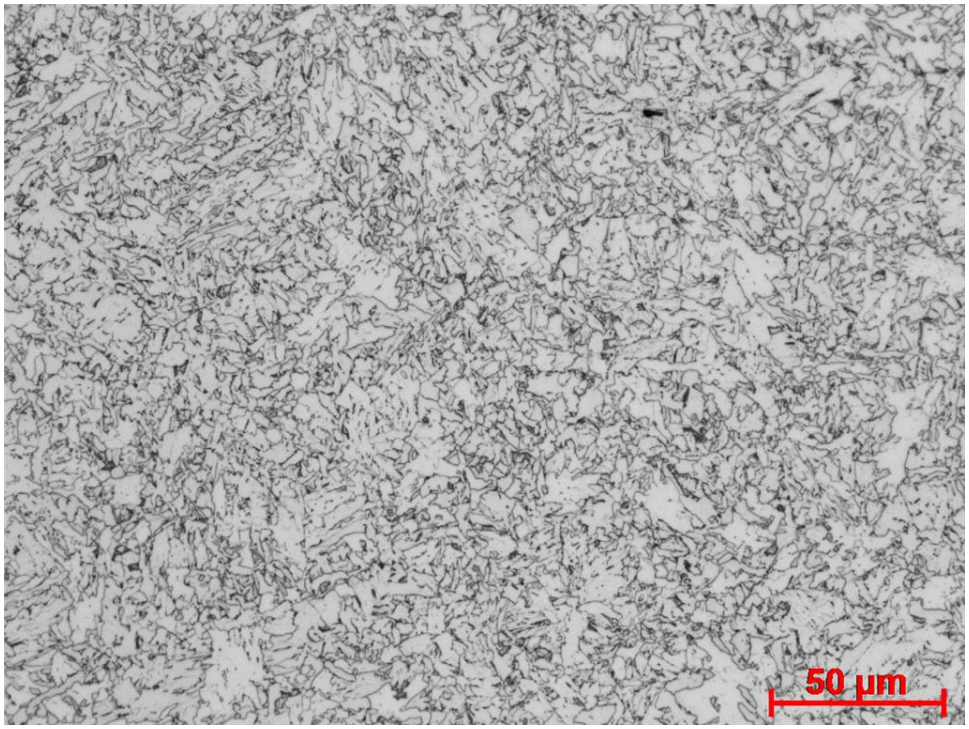

(a)

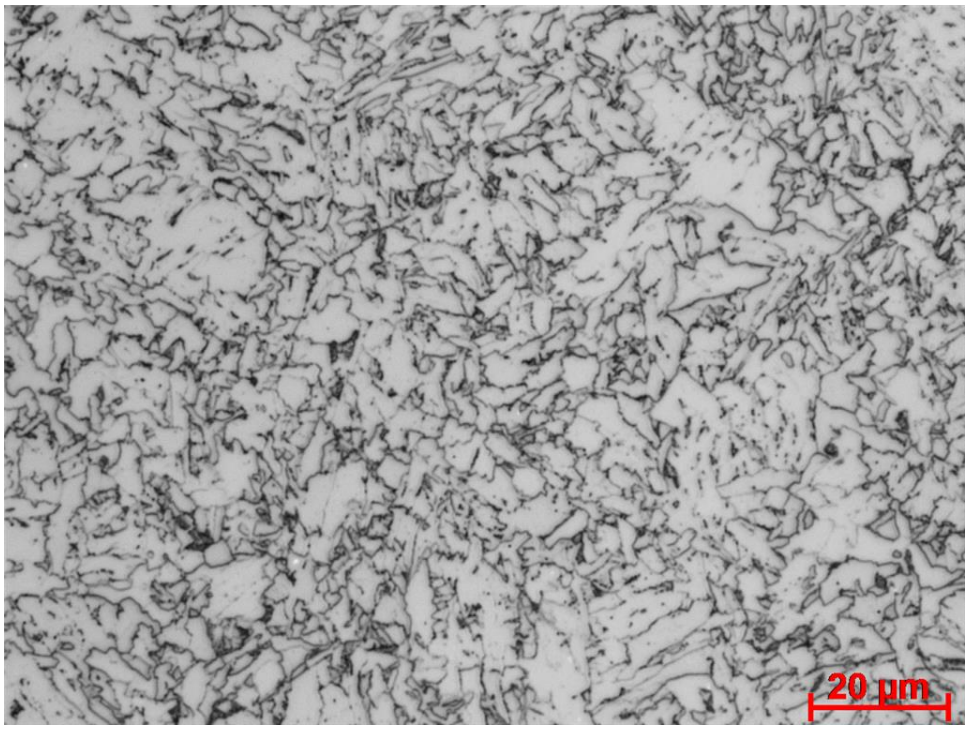

(b)

Figure B26 Reheated HAZ microstructure near 5 mm targeted notch depth for CWP from Weld-236-1

The microhardness results obtained from full-thickness sections (different clock positions) of the girth welds provided valuable insight regarding the consistency of welding procedures used to fabricate the respective girth welds. Figure B27 provides a comparison of the through-thickness (TT) WMC traverses for the two pipe girth welds (Weld 236 (Weld-1) and Weld 233 (Weld-2)). In both cases, there were some variations as a function of clock position observed (e.g., specimens labelled Weld 236-1, 236-2 and 236-4). The plots revealed a similar saw-tooth pattern with a noticeably high hardness spike seen at a depth of ~4 mm that was followed by a gradual decrease in hardness until a more pronounced decrease occurs entering the root pass. The spike in hardness is believed to be related to multiple reheating and cooling of the adjacent cap passes that had weld metal from a more alloyed wire.

The differences observed between the through-thickness WM and HAZ microhardness profiles for Weld 236 (Weld-1) and Weld 233 (Weld-2) are shown in Figure B28 and Figure B29**,** respectively. It is clear from Figure B30 that the hardness profiles follow similar trends, but also clearly show that Weld 236 (Weld-1) exhibited consistently higher hardness values compared to Weld 233 (Weld-2). In contrast, the HAZs had similar hardness profiles, except for a high and low spike near the cap of Weld 236 (Weld-1) and the higher hardness values beyond a 15mm depth.

The cross-weld traverses were also plotted for the three full-thickness sections cut from the respective girth welds (Figure B30 to Figure B38). There were obvious differences and variations as a function of through-thickness profile locations, e.g., Sub-Cap, Mid-Thickness, and Root that relate to specific HAZ and WM structure that are intersected for a given traverse. For Weld 236 (Weld-1), (Figure B30 to Figure B33) there were more marked variations for sub-cap and root profiles compared to the mid-thickness. For example, the 236-2 sub-cap profile exhibited significant softening, while the mid-thickness remained largely unchanged and the root displaying very low constant hardness profile (Figure B31). The profile for Weld 236-4 revealed major softening of the sub-cap with variation at the mid-thickness and intermediate root pass profile. Figure B33 provides a comparison of the mid-thickness profiles for Weld 236 (Weld-1) with consistent trends for all three sections except for some increased softening in the WM for 236-4.

For Weld 233 (Weld-2) the plots presented in Figure B34 to Figure B36 indicate that more consistent through-thickness profiles are observed although variations still exist for the sub-cap profiles, while very consistent profiles were measured for the mid-thickness as in Figure B37.

The overall differences between the two welds are evident in the combined plot in Figure B38, where the profiles are very similar, except that higher WM hardnesses was obtained for Weld 236 (Weld-1) compared to Weld 233 (Weld-2). This agrees with the AWMT data that indicated the trend with both the yield and ultimate tensile strengths being higher for Weld 236 (Weld-1).

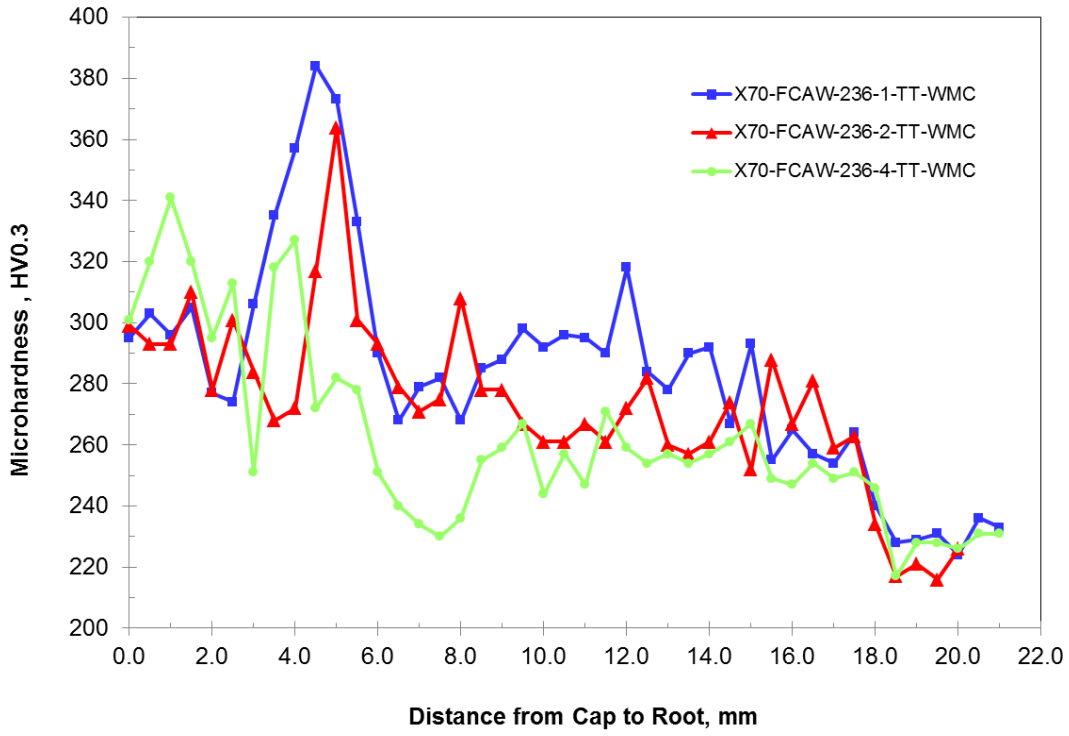

(a)

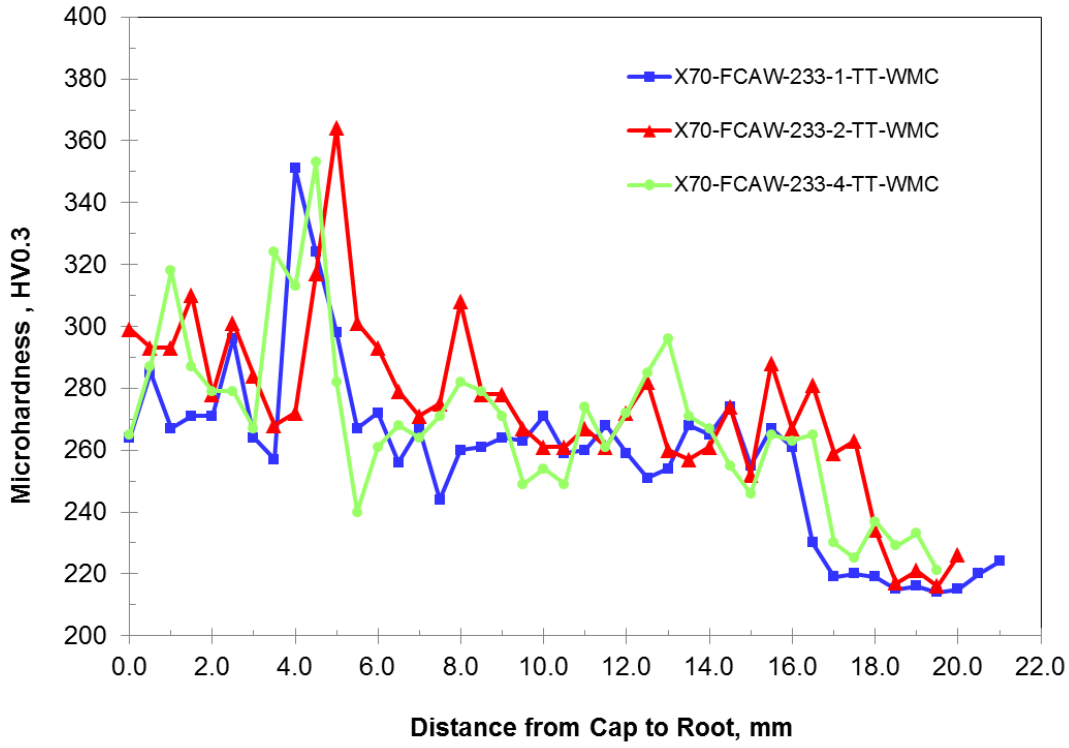

(b)

Figure B27 Comparison of through-thickness weld metal centerline microhardness for three different positions around girth Welds 236 and 233

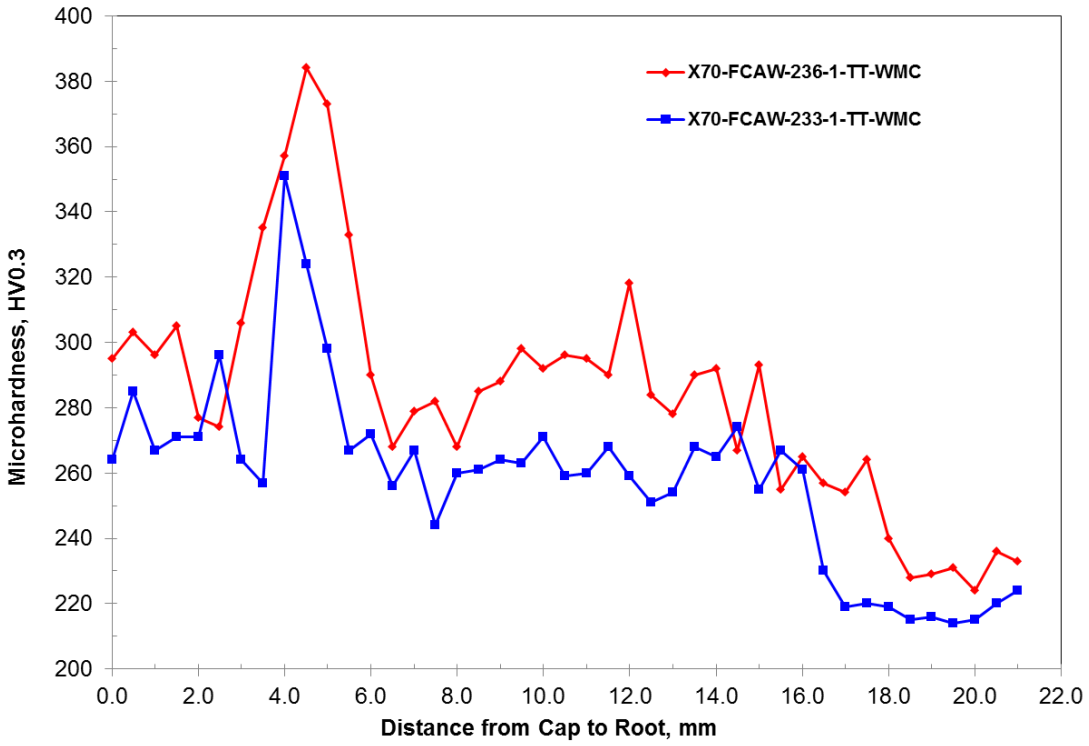

Figure B28 Through-thickness WMC microhardness surveys for Welds 236-1 and 233-1

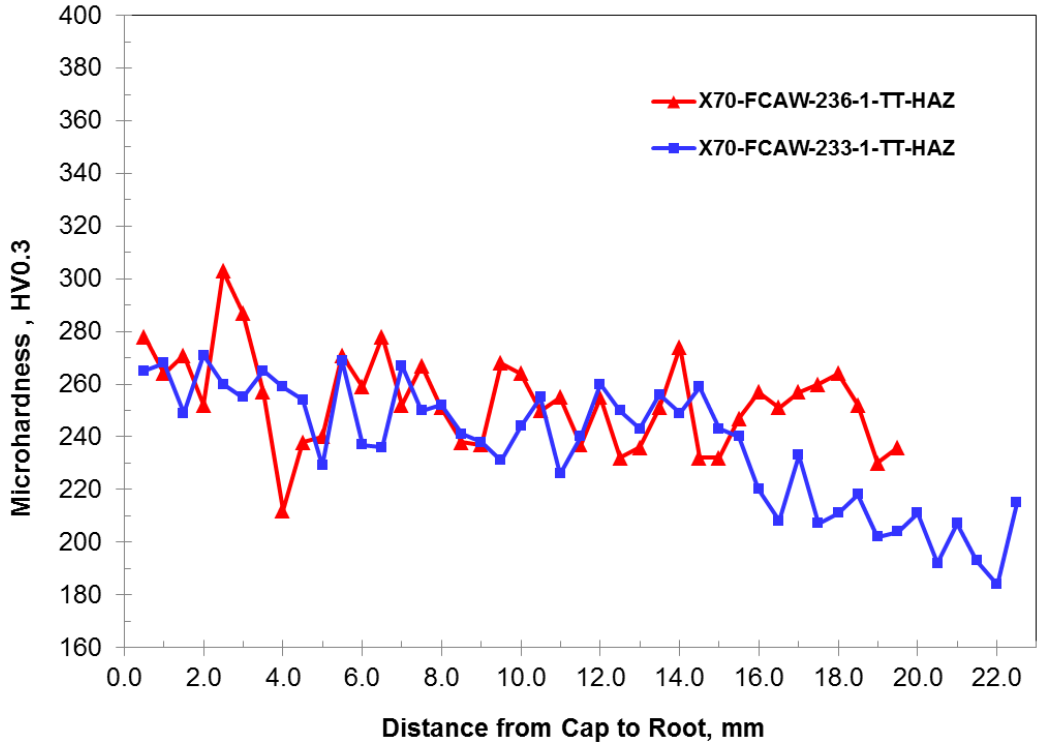

Figure B29 Through-thickness HAZ microhardness surveys for Welds 236-1 and 233-1

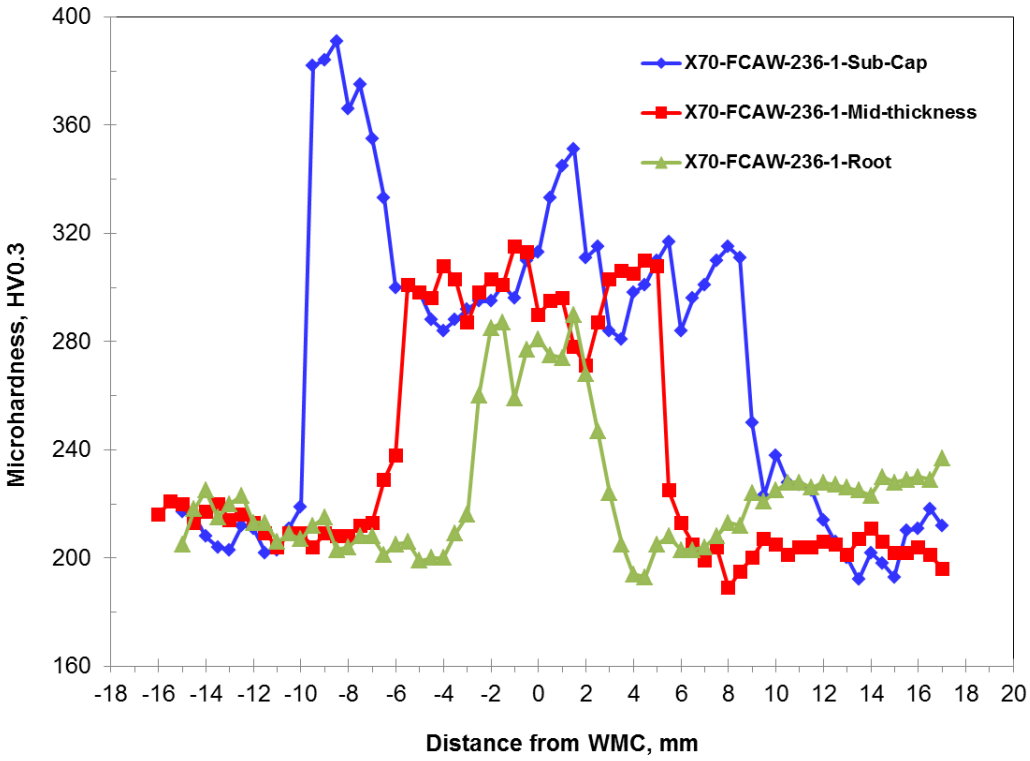

Figure B30 Cross-weld microhardness traverses for cap, mid-thickness and root of Weld 236-1

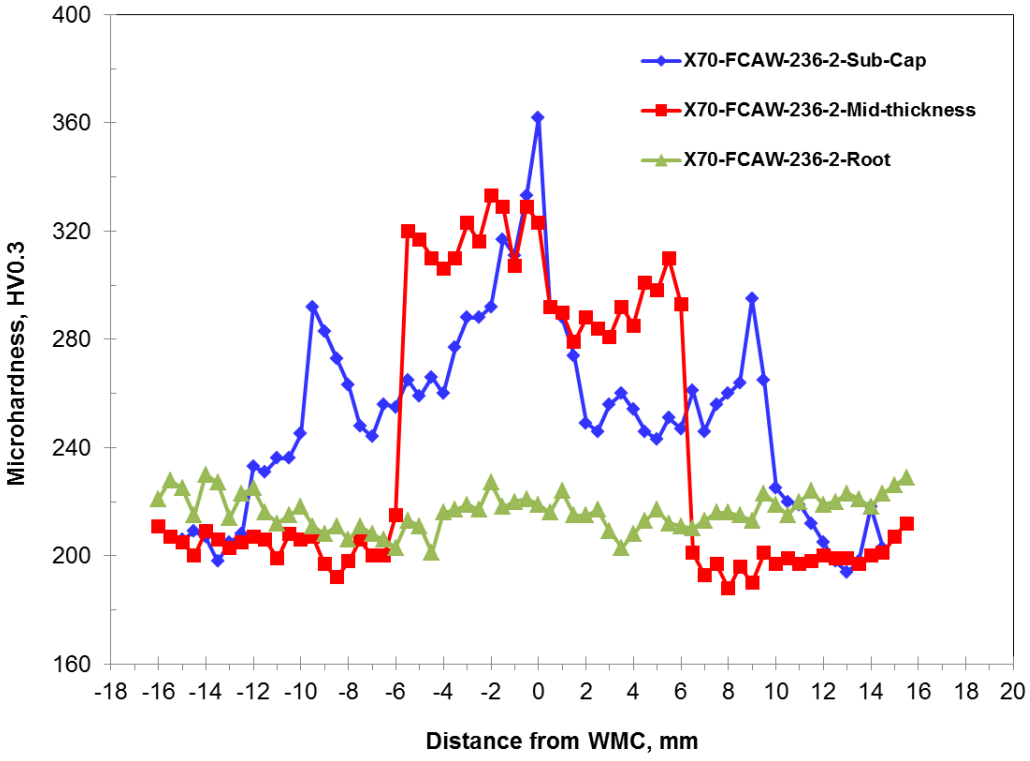

Figure B31 Cross-weld microhardness traverses for cap, mid-thickness and root of Weld 236-2

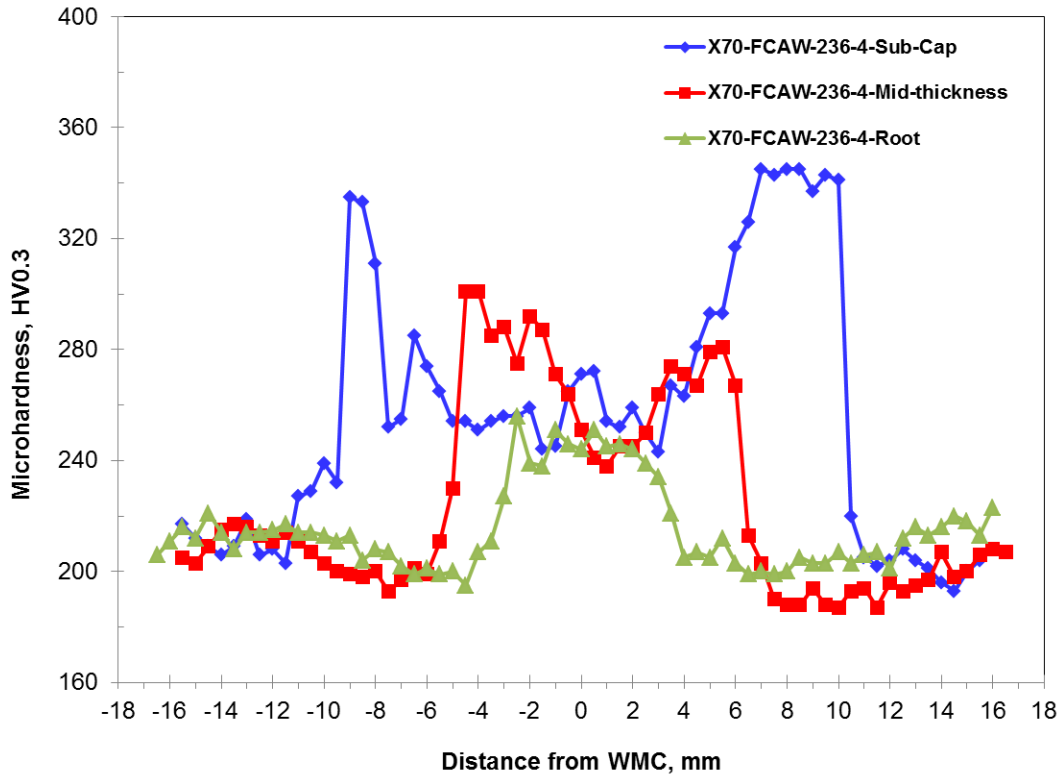

Figure B32 Cross-weld microhardness traverses for cap, mid-thickness and root of Weld 236-4

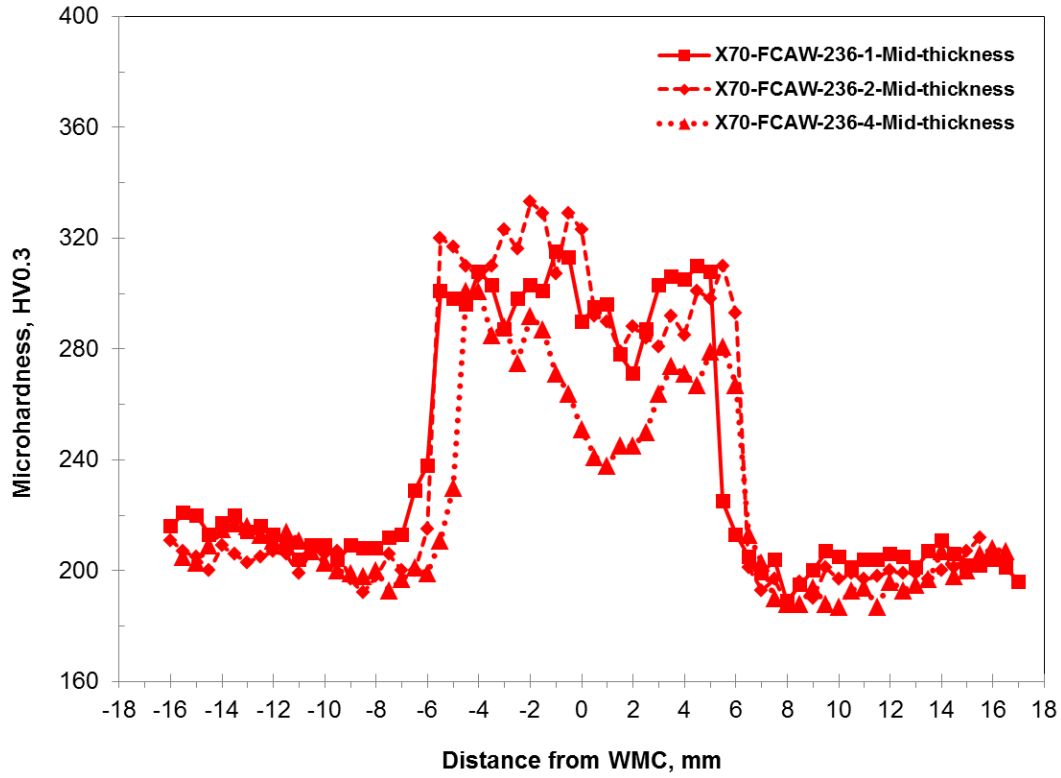

Figure B33 Comparison of cross-weld microhardness for mid-thickness of Weld 236

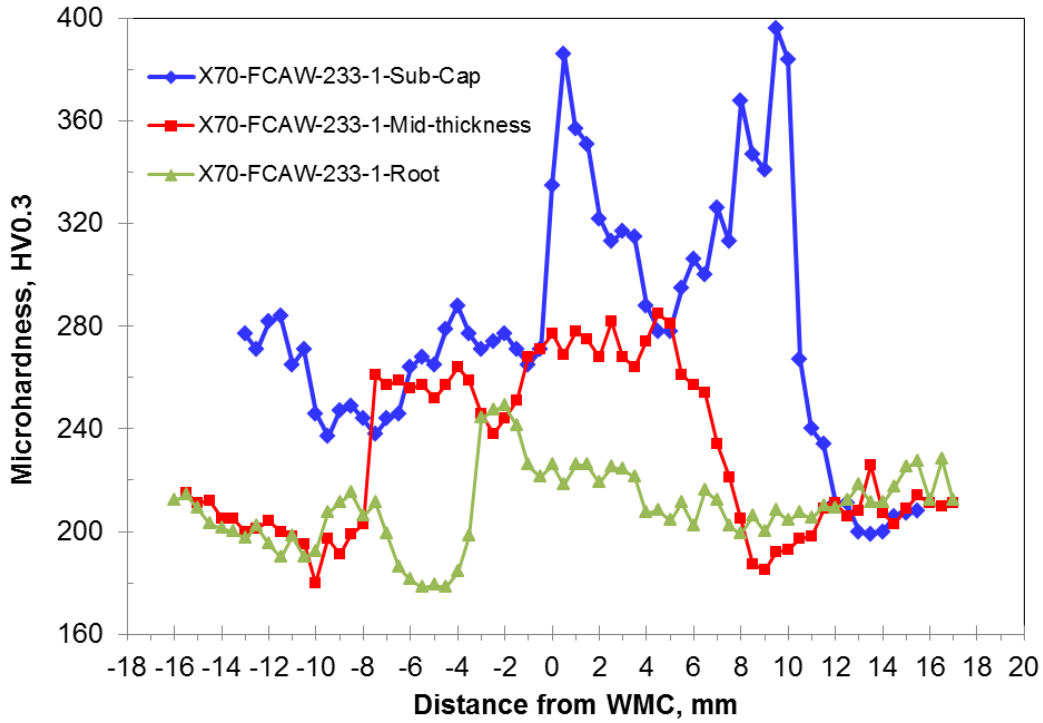

Figure B34 Cross-weld microhardness traverses for cap, mid-thickness and root of Weld 233-1

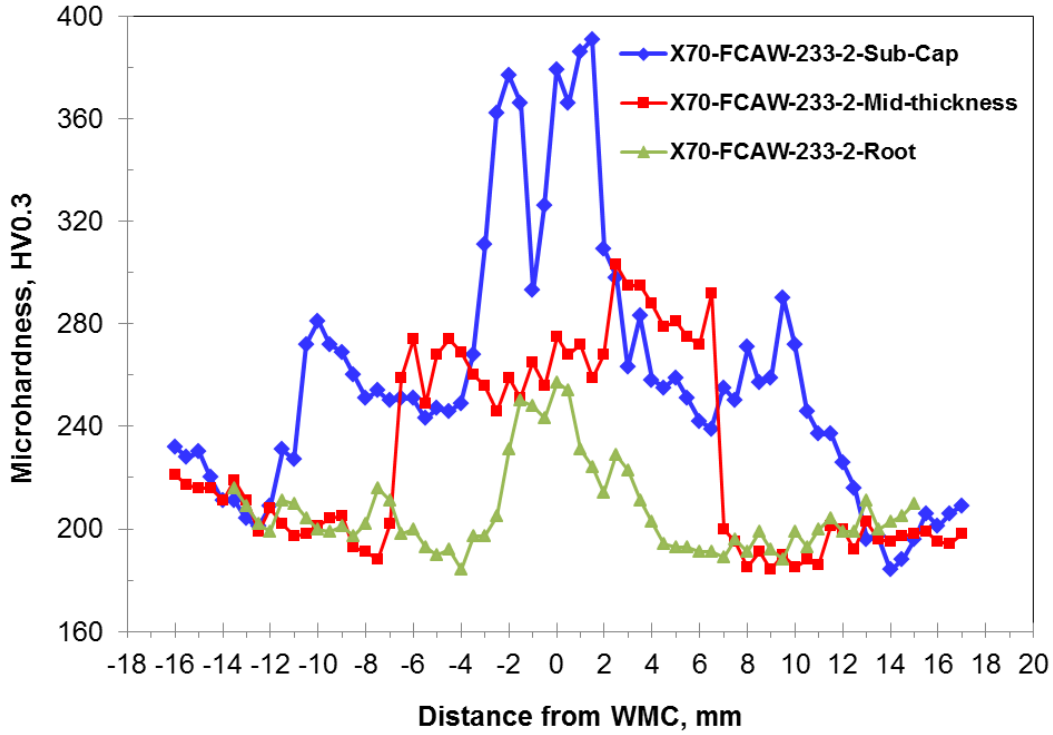

Figure B35 Cross-weld microhardness traverses for cap, mid-thickness and root of Weld 233-2

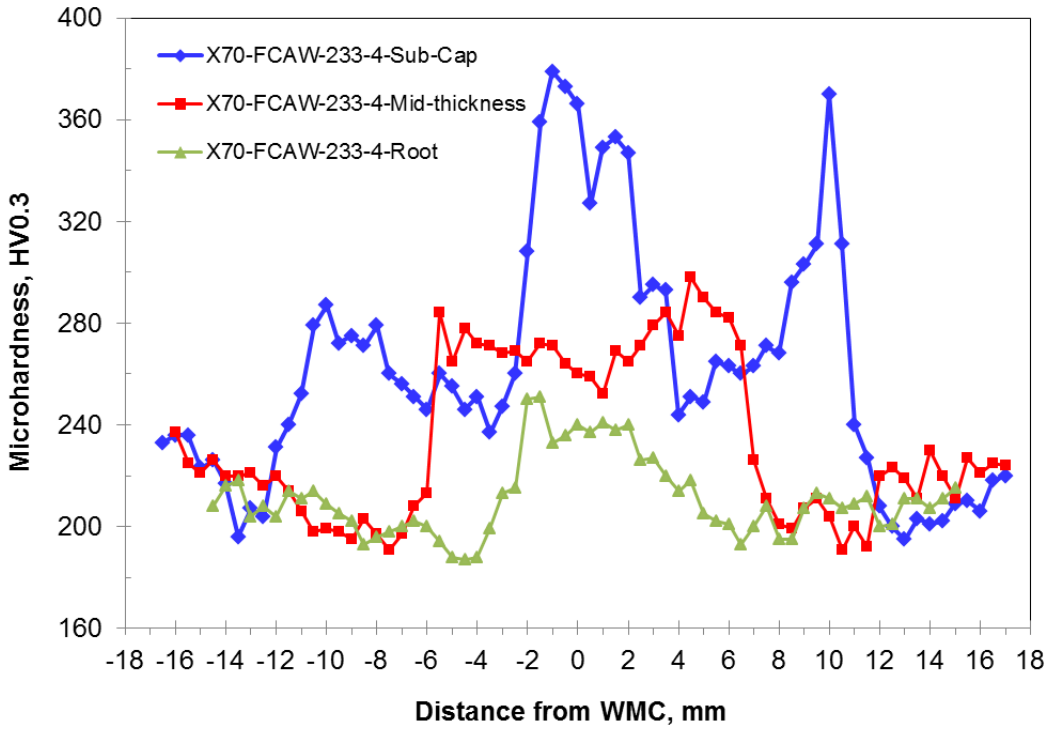

Figure B36 Cross-weld microhardness traverses for cap, mid-thickness and root of Weld 233-4

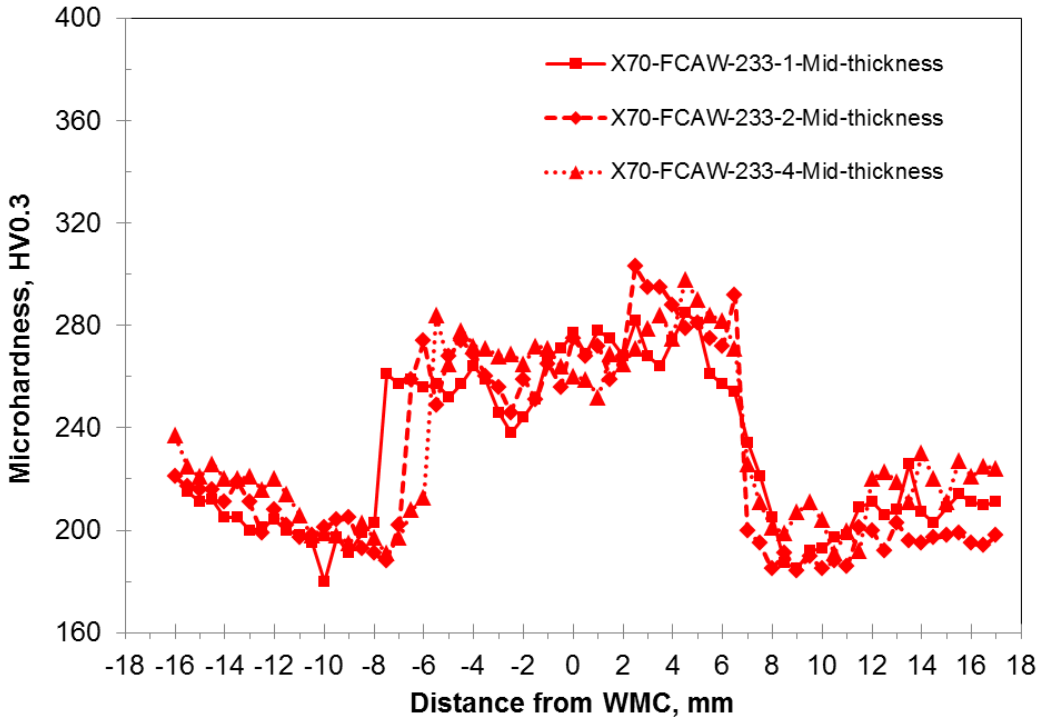

Figure B37 Comparison of cross-weld microhardness for mid-thickness of Weld 233 (Weld-2)

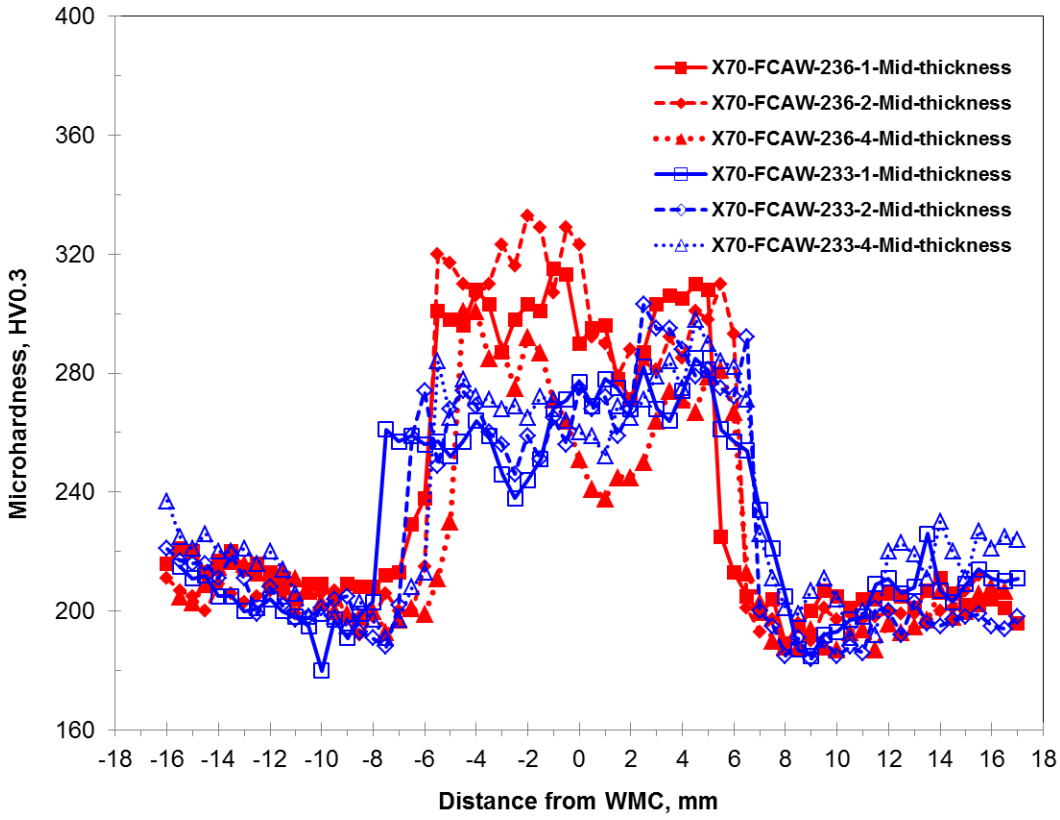

Figure B38 Cross-weld microhardness profiles for the mid-thickness of Welds 236 and 233

B.7 Charpy V-Notch Tests

As outlined in the cutting layout plan in Section B.1 multiple pipe girth weld sections, cut from regions between the CWP specimens, were used to prepare the large number of Charpy-V-notch (CVN) test specimens from each girth weld. A total of 33 and 36 CVN test specimens were machined from the girth Weld 236 (Weld -1) and Weld 233 (Weld-2), respectively. Since the specimens were from different circumferential positions around each of the pipe girth weld, the totals were divided so that the even numbered specimens were allocated to test the weld metal and the odd numbered specimens were used for HAZ tests. The specimens were cut transverse to the girth weld per the guidelines in API 1104 and illustrated in the drawing and macrograph shown in Figure B39. As a result, the CVN specimens were located just beneath the cap passes at a position ~2 mm below the pipe OD surface. All specimens were etched in a 3% Nital solution to reveal the weld metal and fusion line adjacent to the HAZ to facilitate accurate scribing of the through-thickness targeted notch locations. For the weld metal, the specimens were scribed at center of weld width at the top (toward the cap passes) and bottom (towards the hot pass) of individual specimens. Figure B39(a) shows, the HAZ targeted notch position which was determined by marking a parallel line that crossed the fusion line at a distance 1/3 below the

OD biased surface. For the counter bore girth weld (Weld 233 [Weld-2]) the 19mm wall thickness pipe that was previously tracked and marked was used for testing.

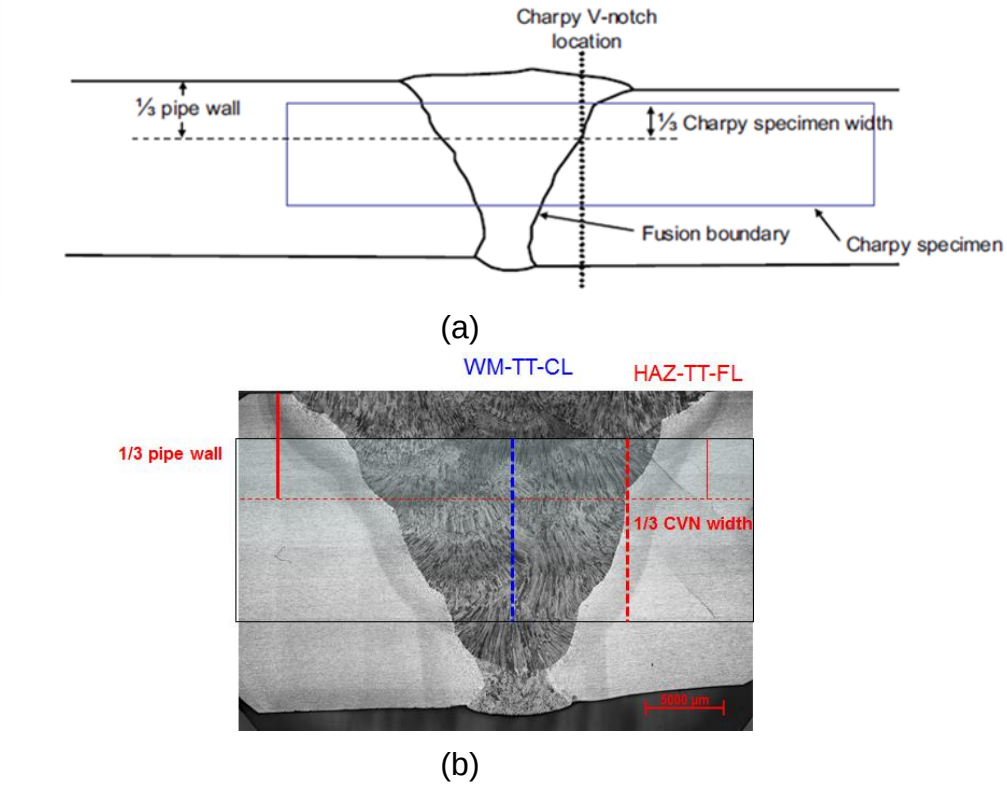

Figure B39 (a) Drawing showing position of a CVN test specimen and notch location for the HAZ and (b) typical notch locations for WMC and HAZ tests superimposed on a macrograph of the girth weld.

Triplicate tests were used to establish the transition behavior of the weld metal and HAZ of the respective girth welds, by testing over a wide range of test temperatures from -75 °C to 25 °C. For the sub-zero tests, the groups of specimens were cooled to the targeted temperatures and held for a minimum of 15 minutes. All tests were completed using a 750 J capacity pendulum impact tester equipped with an instrumented striker.

The average and individual CVN impact energies are provided in Table B5, Table B6 and Table B7, along with photographs taken of the facture surfaces for each set of three test specimens. Results for the weld metals were reasonably consistent for tests at a given temperature, exhibiting nearly fully ductile upper shelf energies at 24 °C with much lower impact energies and little if any percentage shear fracture at the lowest test temperature of -60 °C (Table B5).

Table B5 CVN results for WMC of Weld 236 (Weld-1) and Weld 233 (Weld-2)

Weld and Specimen Description	Test Temperature, ^{o}C	Absorbed energy, J avg. (individual values)	CVN Fracture Appearance
Weld-236-WMC	24	117 (114, 110, 128)	
	0	68 (64, 73, 67)	
	-18	55 (56, 50, 59)	
	-45	31 (43, 19, 32)	
	-60	24 (24, 19, 29)	
Weld-233-WMC	24	104 (107, 107, 97)	
	0	96 (101, 98, 89)	
	-18	94 (81, 96, 104)	
	-45	45 (47, 43, 44)	
	-60	33 (31, 32, 35)	

There were some differences in CVN impact toughness between the two girth welds that may be explained based on the variations in welding procedure, the difference in specimen clock positions and the final notch placements.

The results obtained for the HAZ tests conducted on Weld 236 (Weld-1) revealed similarly high average upper shelf impact energies at both -45 °C and -18 °C, while at lower temperatures there was some significant scatter in results observed.

Table B6 CVN results for HAZ testing of Weld 236 (Weld-1) (16 mm to 16 mm)

Weld and Specimen Description	Test Temperature, °C	Absorbed energy, J avg. (individual values)	CVN Fracture Appearance
Weld-236-HAZ	-18	259 (261, 267, 249)	
	-45	258 (261, 255, 258)	
	-50	113 (49, 231, 60)	
	-60	55 (48, 55, 61)	
	-75	28 (28, 216*, 29)	
	-75	44 (272*, 51, 38)	

Note: *High values recorded at -75 °C were excluded from average due to possible inconsistent notch positioning.

For Weld 233 (Weld-2), although higher upper shelf energies (> 300 J) were observed, there was a dramatic decrease and significant scatter in the results obtained at lower test temperatures, *i.e.*, 198 J at -30 °C and 193 J at -45 °C. At the -50 °C and -60 °C test temperatures variation in the impact energies influenced the averages values. At the -75 ° C test temperature an average of 41 J was obtained.

Table B7 CVN results for HAZ testing of Weld 233 (Weld-2)

Weld and Specimen Description	Test Temperature, °C	Absorbed Energy, J avg. (individual values)	CVN Fracture Appearance
Weld-233-HAZ	-18	317 (348, 304, 300)	
	-30	198 (129, 258, 207)	
	-45	193 (66, 284, 228)	
	-50	79 (58, 58, 121)	
	-60	92 (91, 36, 149)	
	-75	41 (40, 30, 54)	

As mentioned above, the observed differences in impact energies for Weld 236 (Weld-1) were also considered to be potential factors, (variation in welding procedures including the

number and sequence of weld passes, differences in specimen clock positions, and notch placements) that contributed to the variation in impact toughness for Weld 233 (Weld-2).

B.8 Charpy-V-Notch Test Results

The individual transition curves for Welds 236 and 233 are shown in Figure B40 and Figure B41 and for comparison purposes in Figure B42. Both weld metals exhibited almost fully ductile fracture (% shear) at the 24 °C test temperature, with some differences in the transition region where Weld 233 (Weld-2) displayed higher toughness values and a low energy transition temperature that may in part be attributable to the lower weld metal hardness and strength for Weld 233 (Weld-2), which in term may be explained based on the variation in welding procedure, including the number of passes used.

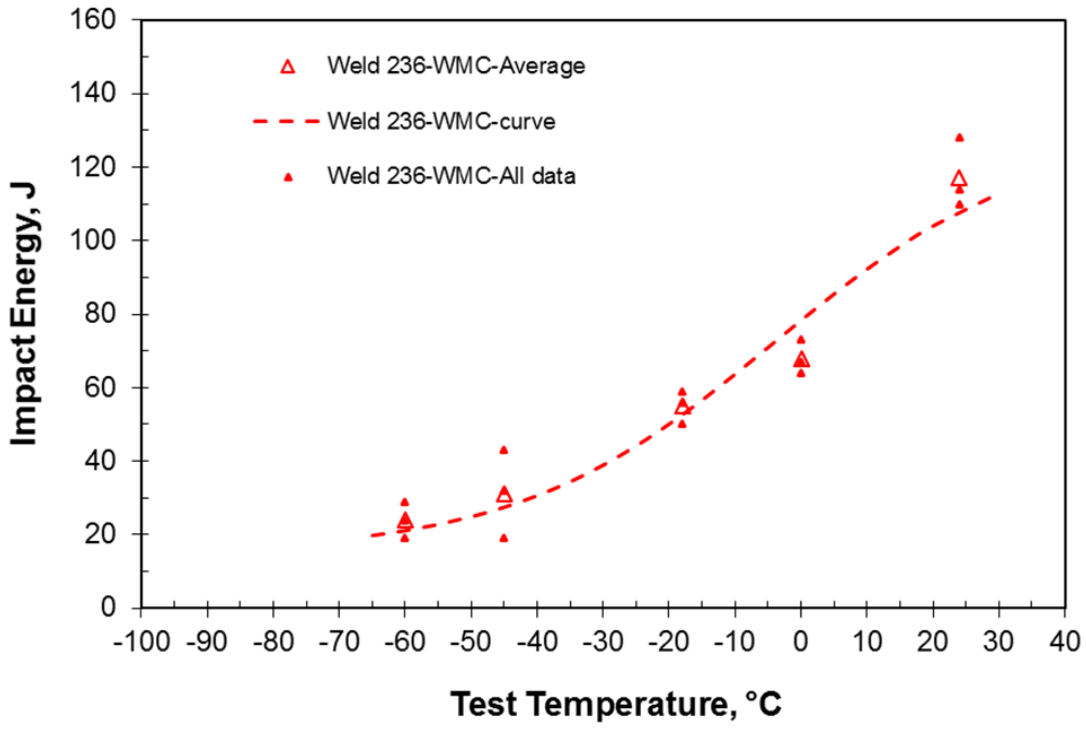

Figure B40 Charpy impact transition curve for the WMC of Weld 236 (Weld-1)

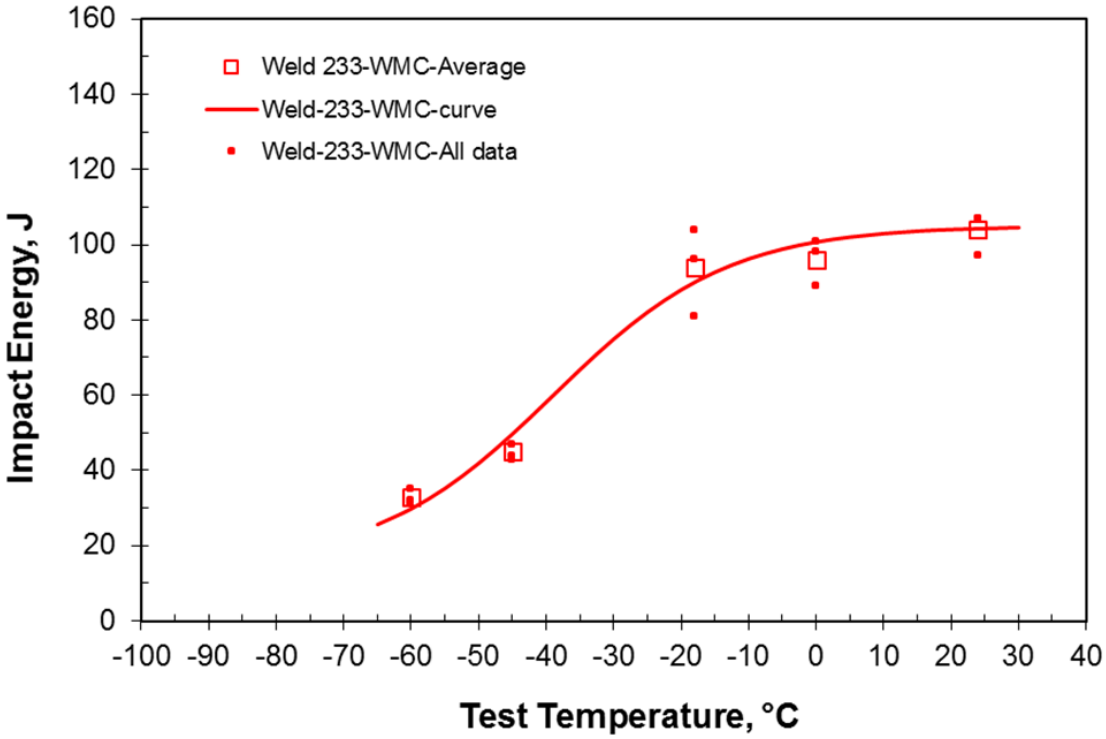

Figure B41 Charpy impact transition curve for the WMC of Weld 233 (Weld-2)

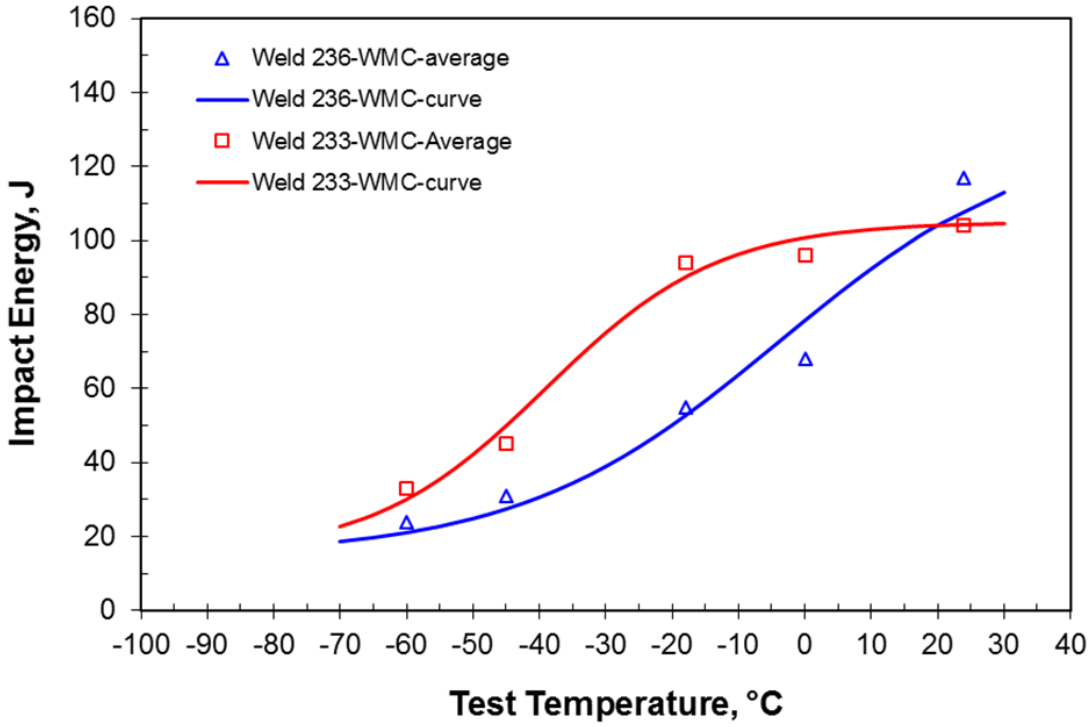

Figure B42 Comparison of Charpy impact transition curves for the WMC of Weld 236 (Weld-1) and Weld 233 (Weld-2)

The HAZ transition curves for Welds 236 and 233 are shown in Figure B43 and Figure B44 and reveal the degree of scatter observed for respective HAZs. Although there was much less scatter and a steeper transition was observed for Weld 236 (Weld -1) compared to Weld 233 (Weld-2) the estimate energy transition temperatures were quite similar at -45 °C and -49 °C, respectively (see Figure B45). Again, there are known factors that may have contributed to the observed HAZ CVN impact toughness, including the small fraction of HAZ sampled, variation in notch placement that may have occurred for specimens taken from different clock positions.

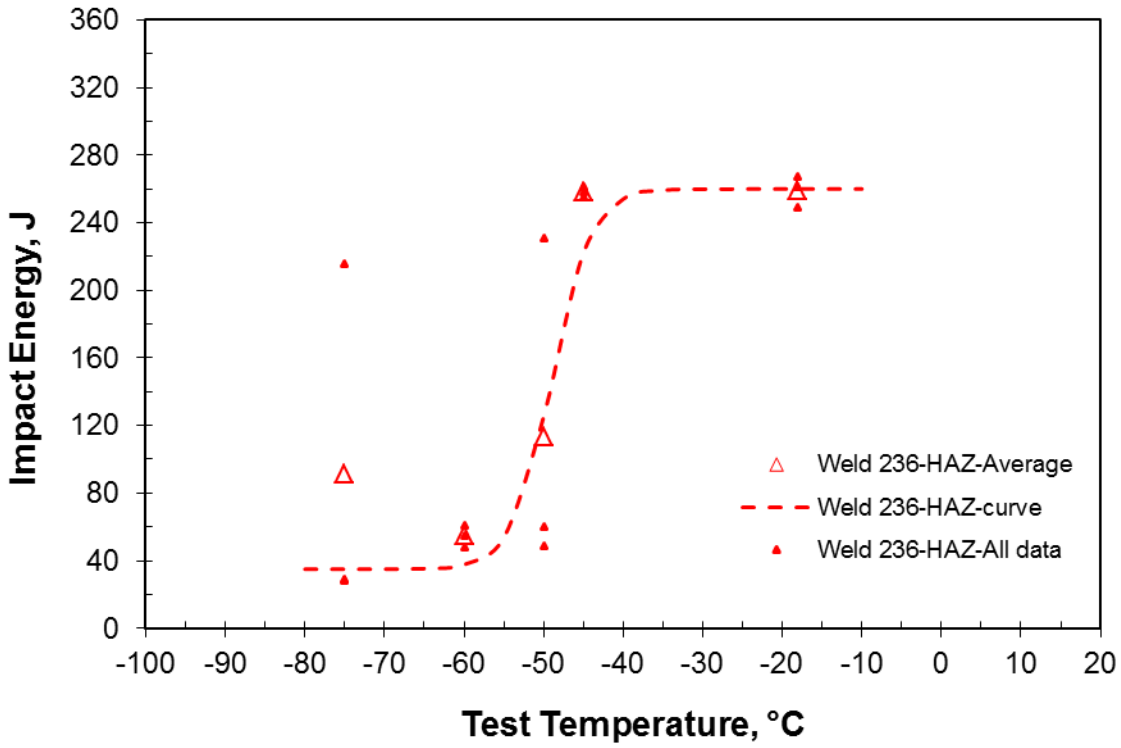

Figure B43 Charpy impact transition curve for the HAZ of Weld 236 (Weld-1)

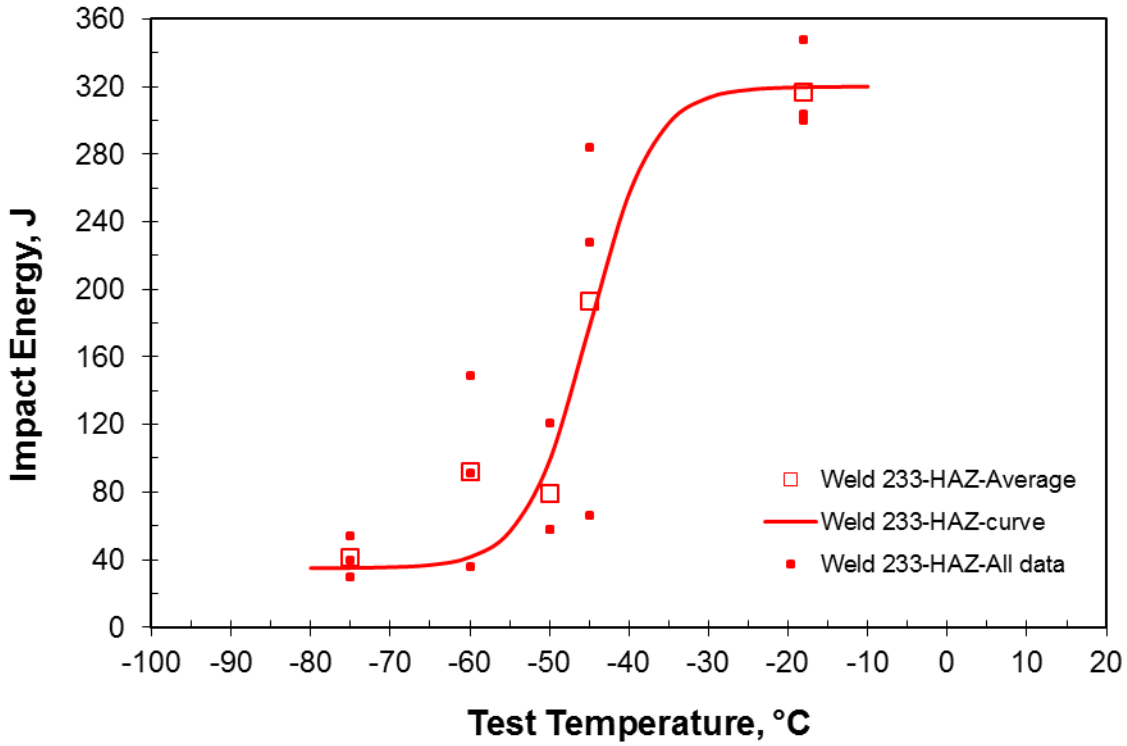

Figure B44 Charpy impact transition curve for the HAZ of Weld 233 (Weld-2)

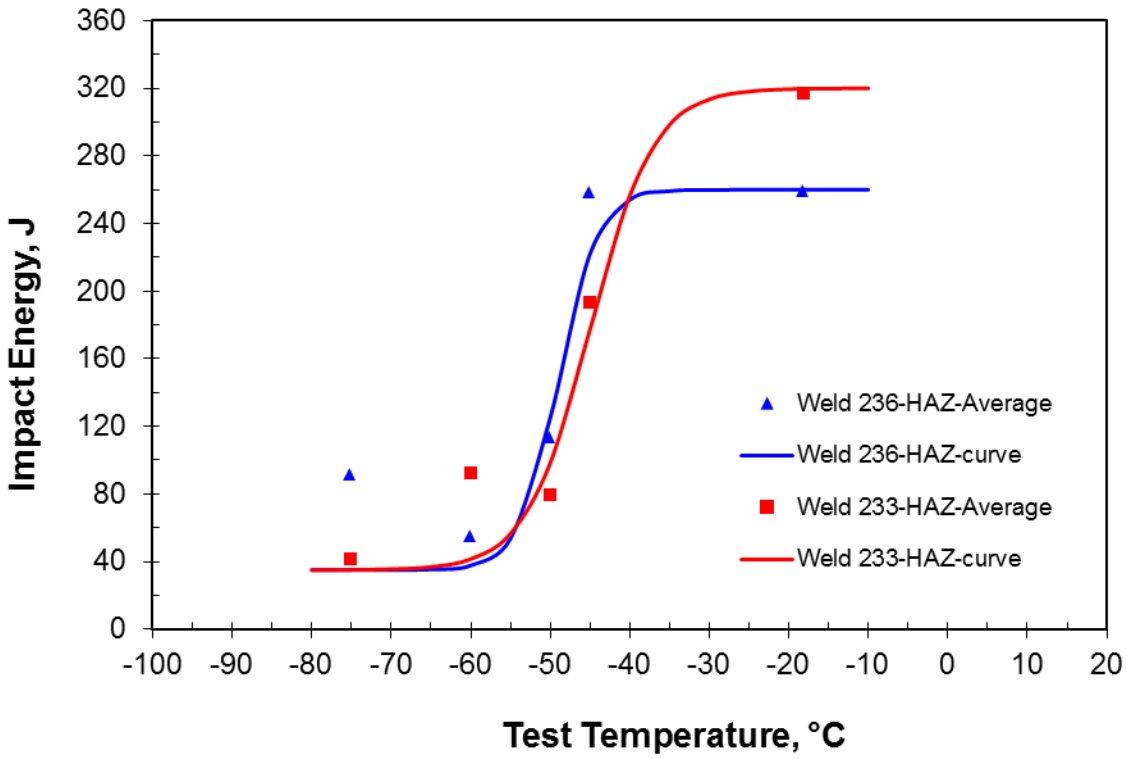

Figure B45 Comparison of Charpy impact transition curves for the HAZ of Weld 236 (Weld-1) and Weld 233 (Weld-2)

B.9 Single Edge Notch Tension Tests

Single Edge Notch Tension [SE(T)] specimen sections were cut according to Figure B2, the progression of machining processes began with milling and grinding each specimen according to the machine drawing shown in Figure B46. The specimen dimensions were initially targeted at 14 mm by 14 mm in cross-section but the machine shop was instructed to minimize material removal for the through-thickness dimension (W) and match that dimension in the normal direction (B) to achieve the square cross section (BXB, W=B).

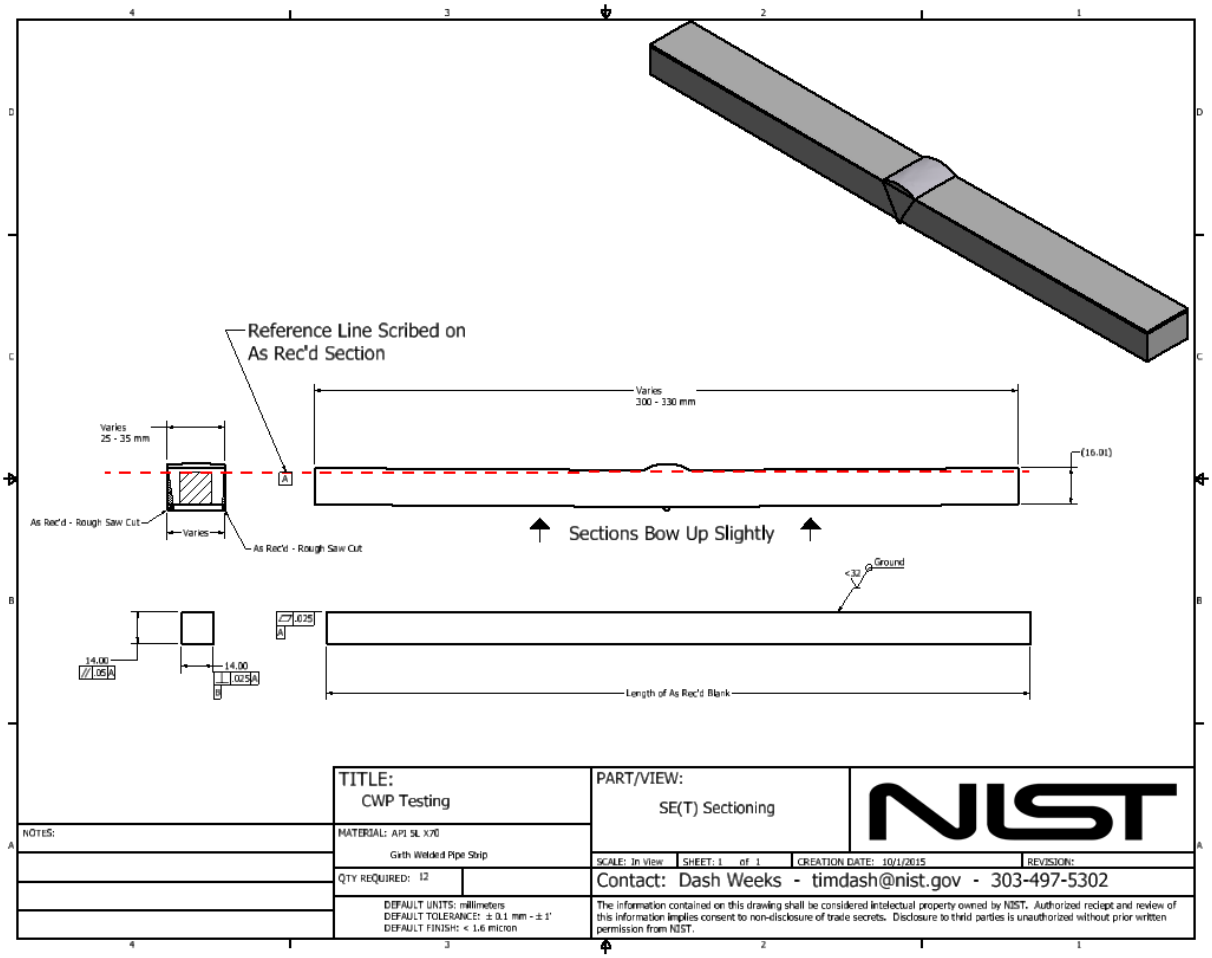

Figure B46 Machine drawing detailing the references and nominal dimension requirements for SE(T) blanks

Machined blanks were returned to NIST for polishing and etching to reveal the cross-section of the weld. Reference lines were scribed onto the specimen surfaces and were then prepared for wire EDM. The specimen details for wire EDM are shown in Figure B47 and Figure B48.

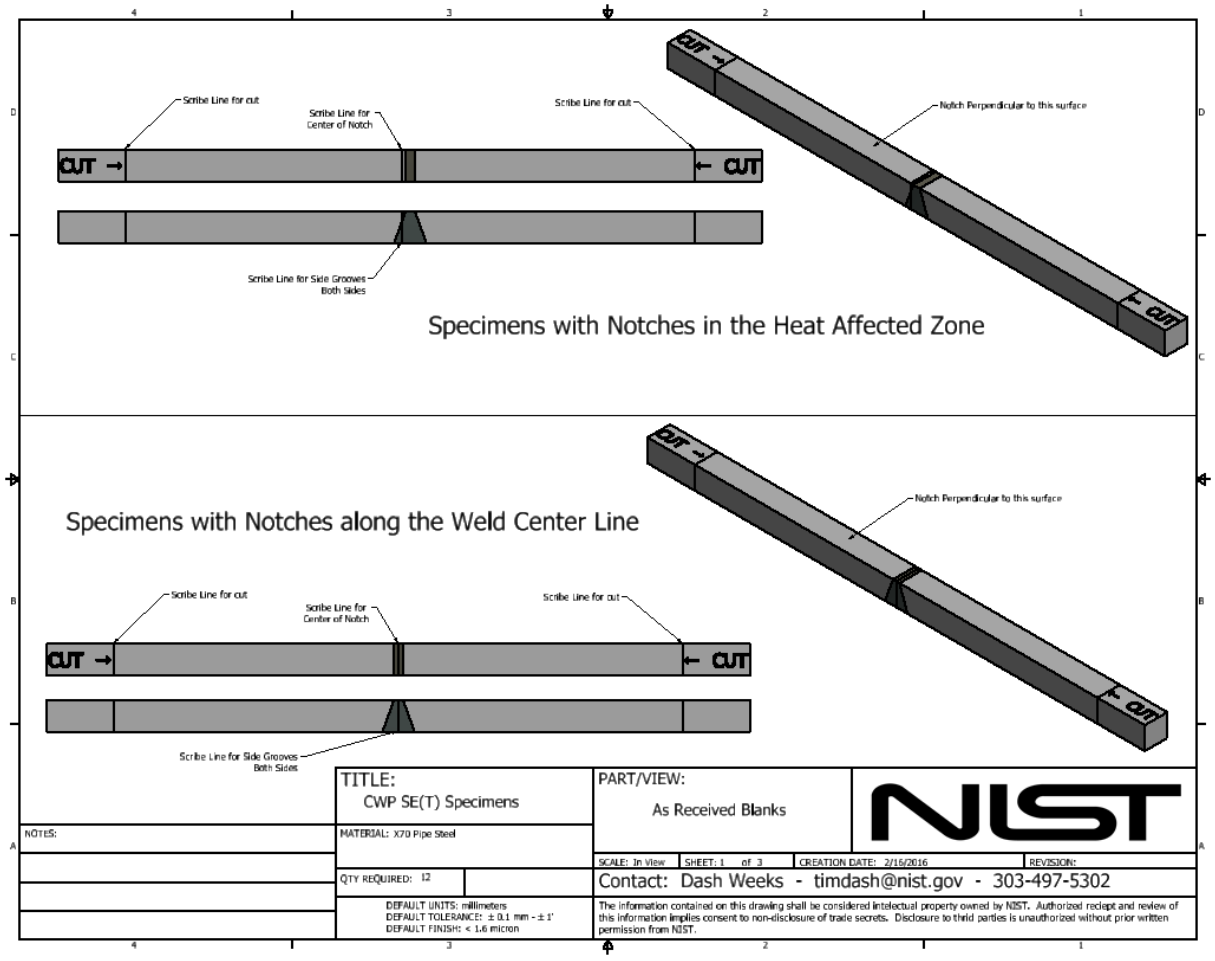

Figure B47 Machine drawing detailing the notching setup references and final length cut lines

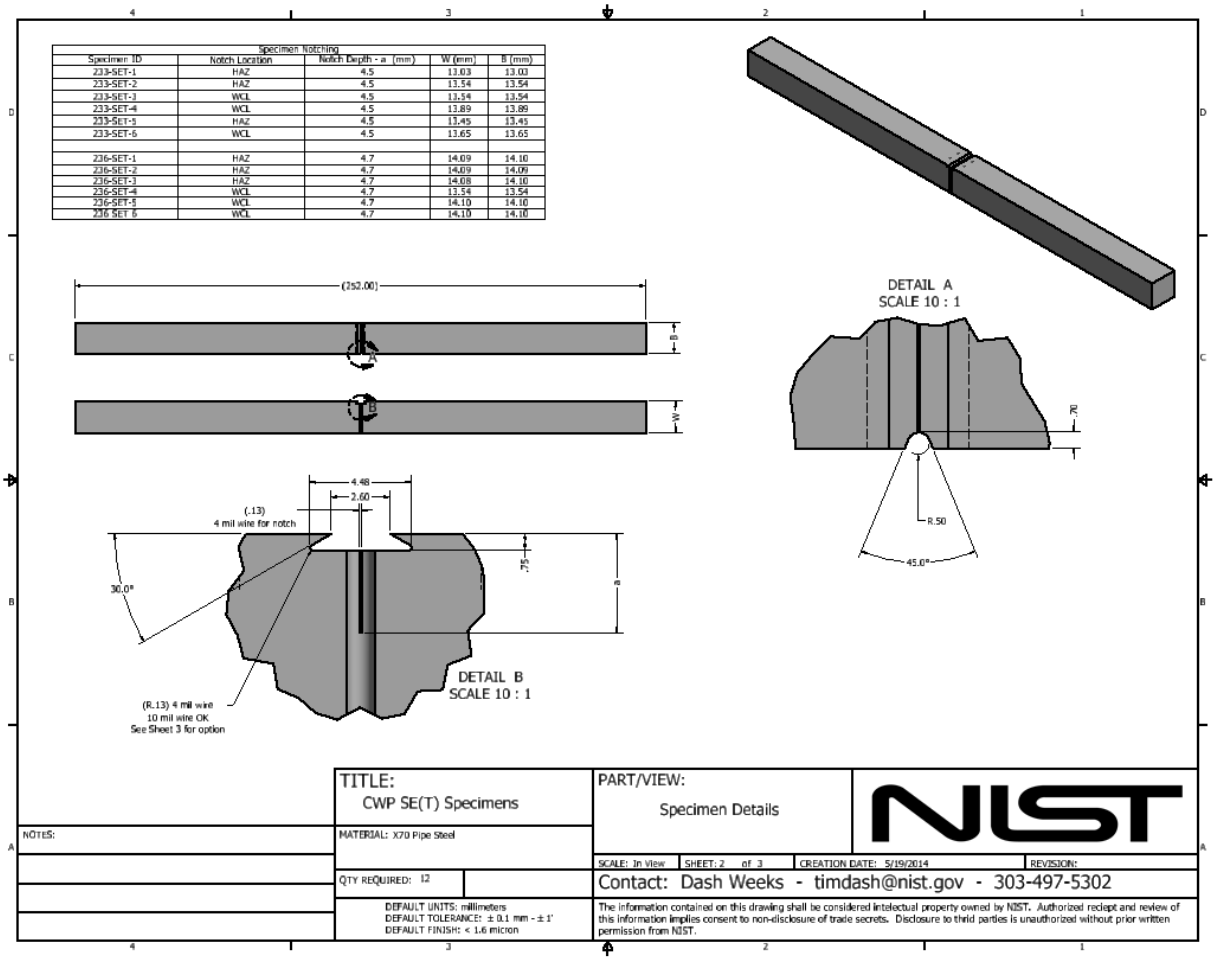

Figure B48 Machine drawing detailing the integral knife edge, notch depths and side groove geometries for each specimen to be machined by wire EDM

The last machining step required for each SE(T) specimen was to drill and tap the holes needed to mount the double clip gauge fixture. The double clip gauge method to determine CTOD-R was included for each of the SE(T) tests but were not required for this project and results are not included in this report. However, the machining details are reported here to fully document the condition of the specimens that were tested. Specimen details for this machining step are shown in Figure B49 and a photograph of all the completed specimens is shown in Figure B50.

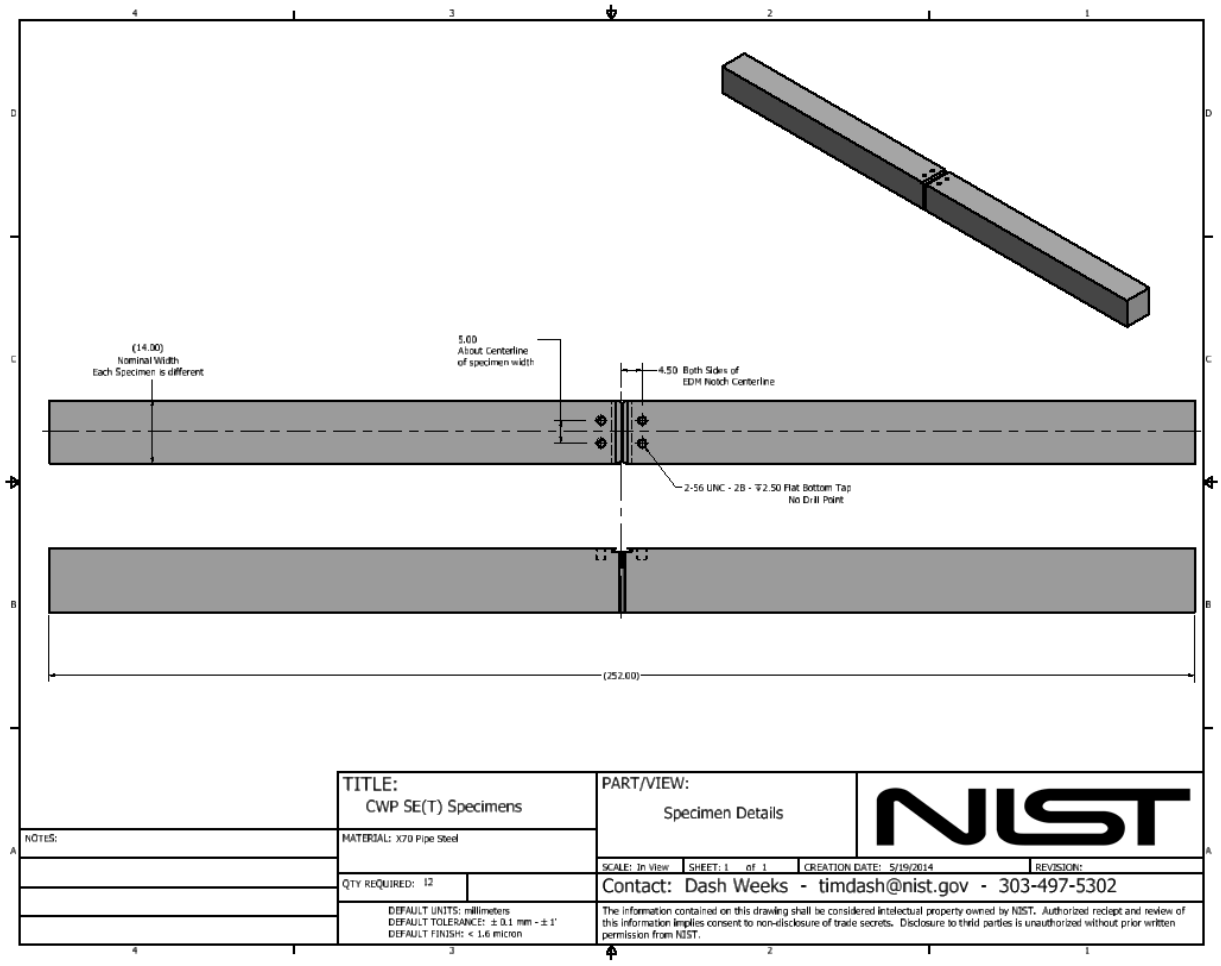

Figure B49 Machine drawing detailing the integrated mounting holes required for the double clip gauge fixture

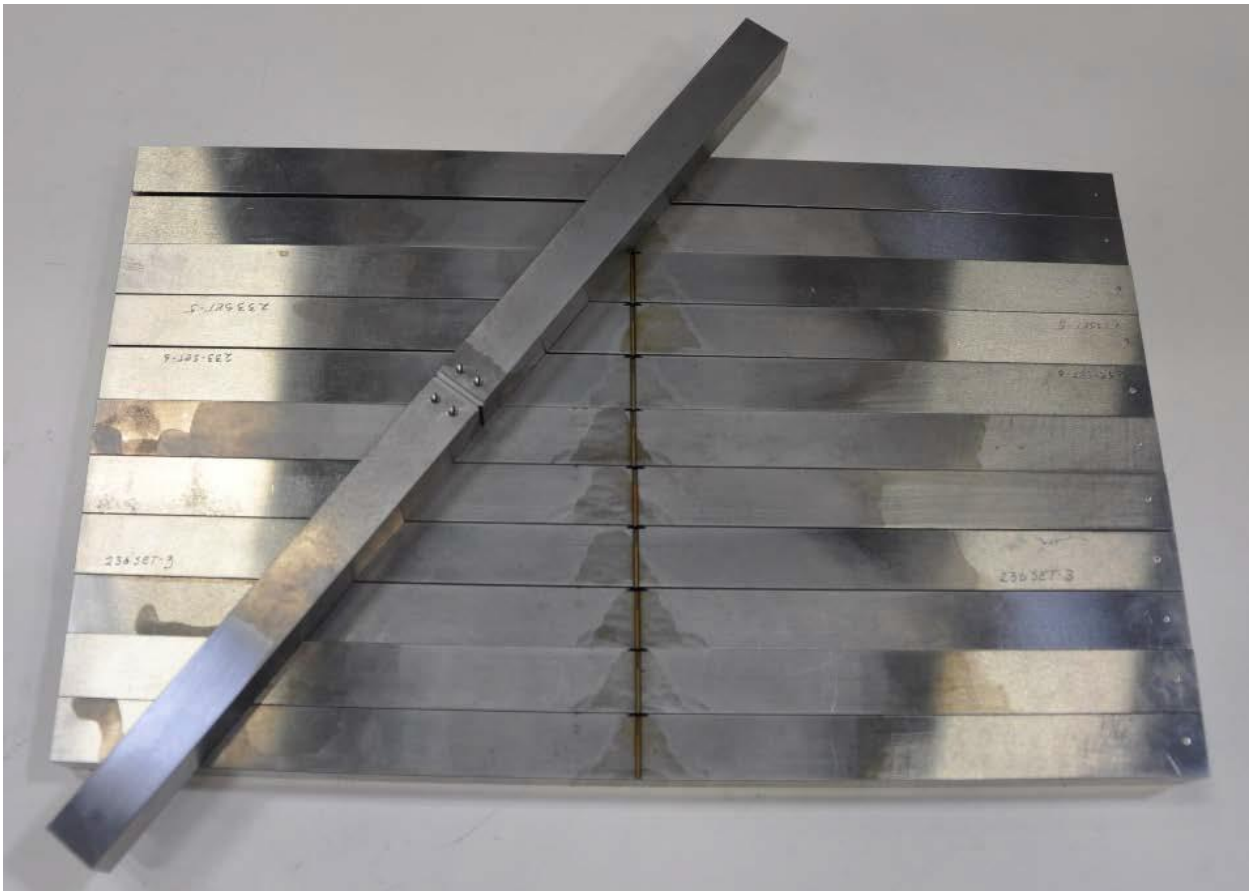

Figure B50 Photograph showing all the completed SE(T) specimens.

Once the SE(T) specimen machining was completed, an inspection process was conducted to dimension the key features of each specimen. Specifically, the key dimensions required for analysis were measured by use of digital calipers and an optical comparator. Measurement results along with the tensile properties necessary for analysis are provided in Table B8. The tensile properties for each specimen are based on base metal strap tensile results and all weld metal tensile tests. Specimens with notches in the HAZ were analyzed with base metal properties. Cross-weld tensile data are not available for these welds.

Each specimen was speckled to employ the DIC measurement technique for future analysis. Each specimen was also instrumented with Direct Current Potential Drop (DCPD) for comparison of crack length estimates between the crack mouth opening displacement (CMOD) unloading compliance (UC) technique and DCPD measurements. The applied current was 3.0 Amps-DC and the current leads were installed 10 mm from each end of the specimen on opposite faces. Neither of these techniques were required as part of the project and results are not reported herein.

Table B8 Single Edge Notched Tension (SE(T)) Specimen Measurements

914 mm (36 in) Outside Diameter – API-5L X70

Weld	Specimen ID	W X B (mm)	a_0 (mm)	B_N (mm)	σ_{YS} (MPa)	E (GPa)
16 mm – 19 mm (Weld 233 [Weld-2])	233-SET-1	13.03 X 13.03	4.51	11.67	508	195
	233-SET-2	13.54 X 13.54	4.50	12.17	508	195
	233-SET-3	13.54 X 13.54	4.52	12.16	716	208
	233-SET-4	13.54 X 13.54	4.71	12.16	716	208
	233-SET-5	13.45 X 13.45	4.54	12.07	508	195
	233-SET-6	13.65 X 13.65	4.52	12.26	716	208
16 mm – 16 mm (Weld 236 [Weld-1])	236-SET-1	14.09 X 14.10	4.72	12.75	510	195
	236-SET-2	14.09 X 14.09	4.72	12.72	510	195
	236-SET-3	14.08 X 14.10	4.76	12.71	510	195
	236-SET-4	13.89 X 13.89	4.52	12.51	782	204
	236-SET-5	14.10 X 14.10	4.74	12.72	782	204
	236-SET-6	14.10 X 14.10	4.75	12.74	782	204

Each specimen was tested in a servo-hydraulic test frame equipped with hydraulic grips. The grip separation for each specimen was set at 140 mm which is nominally 10W for all specimens and was not changed to accommodate small dimensional differences from the nominal 14 mm specimen width.

Each specimen was electrically isolated from the grips and load frame by use of fiber-reinforced polymer (FRP) tabs, 3 mm thick and approximately 14 mm wide by 75 mm long. Electrical isolation improved the DCPD measurements by reducing electrical noise. Hydraulic wedge grips with diamond serrated faces set to a pressure of 13.7 MPa (2000 psi) were used to clamp the specimen. The specimen was installed so that the grip spacing was symmetric about the specimen centerline or crack plane. The specimen axial centerline was carefully aligned with the load-line center to avoid bending or shear stresses in the specimen ligament.

All tests were carried out at ambient room temperature ($\approx 21\ ^{o}$C). The loading profile was programmed into the controller of the servo-hydraulic test frame. Three grip-seating cycles between 5 kN and 10 kN were applied to each specimen, followed by unloading the specimen to 0.2 kN prior to beginning the test. The loading profiles were separated into two sections,

delineated approximately by the proportional limit. The goal was to complete eight unloading cycles before the net section stress reached approximately 75 % of the yield strength. All loading, unloading and reloading commands were executed in displacement control at a rate of 0.025 mm/s. The loading program incorporated pre-programmed force limits to reverse the direction of the actuator. The unloading-reloading sequence prior to the proportional limit did not include a pause before unloading, whereas a three-second hold was programmed for the unloading-reloading sequences after the proportional limit.

The next unloading-reloading sequence was at an absolute load limit close to the net-section yield-load of the specimen based on reported yield strength. Due to the uncertain nature of the yielding event and low slope of the post-yield Force-CMOD data, the operator had the option of interrupting this loading cycle and manually initiating the next sequence if it appeared that the pre-programmed increment would have lost data in the transition.

The next section of the test involved unloading/reloading cycles in the plastic range, where the specimen was also unloaded and reloaded in displacement-control at a rate of 0.025 mm/s. The limits defining the start and stop of each unload/reload cycle used the CMOD signal as a limit; a software loop was programmed to iterate the entire process. Beginning at the incremental load maximum (P^i_{Max}) of the current (i-th) loading segment, specimens were held in displacement control for three seconds prior to unloading to a load 25 kN lower than P_{iMax} and then reloaded by 23 kN. Reloading the specimen by 23 kN ensured that the specimen was reloaded nominally elastically. Deformation was then continued until the CMOD had increased by a relative 0.1 mm. When the CMOD increment was reached, a new P^i_{Max} value was defined (based on the load achieved at the end of the increment) and the loop was iterated. A schematic view of this control method is shown in Figure B51. The CMOD increment effectively defines the number of unloadings in the plastic portion of the test, with a goal of acquiring 20-30 CMOD-UC measurements prior to the specimen attaining a maximum in the applied force. The test continued past the maximum force and was terminated when the CMOD reached 3.5 mm or when the P^i_{Max} was 80% of P_{Max}.

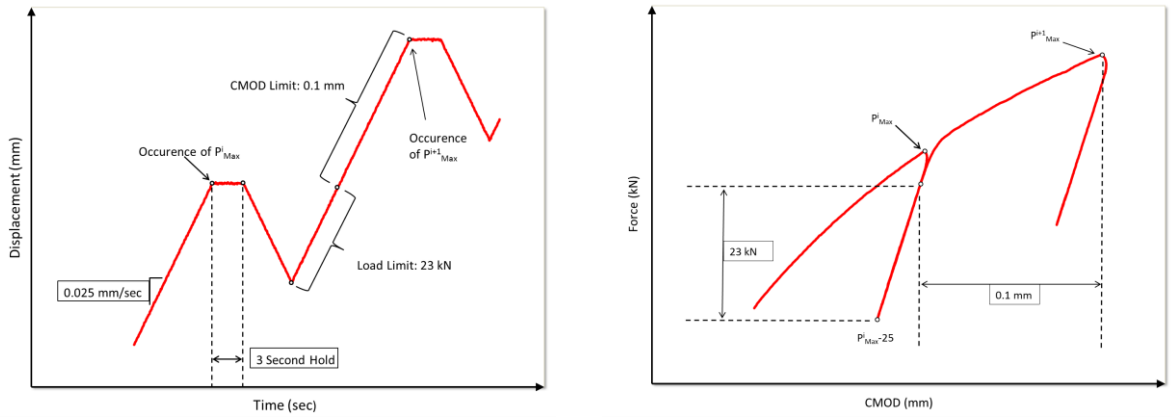

(a) (b)

Figure B51 Schematic plot of the control method used after the proportional limit of the specimen. Each unloading-reloading cycle was done in displacement-control; plot (a) shows the displacement vs. time of an unload-reload and unload cycle with a typical resulting load vs. CMOD plot shown in plot (b).

After testing, the specimen was placed in a furnace at a temperature of 300 °C for approximately 30 minutes to heat-tint the exposed crack surfaces. Crack surfaces were liberated by brittle fracture by cooling with liquid nitrogen and then bending to fracture. Fractographs were taken of both sides of each fracture surface. The fractographs were analyzed and final crack sizes (a_f) were measured optically by use of the nine-point average method. Note that the pre-test measurement of a_0 was used in the analysis as presented in Table B8, post-test measurements of a_0 of six specimens were compared to the pre-test measurements and no significant differences were found. Therefore, optical measurements of a_0 are not presented. Post-test optical measurement of a_0 is only important for specimens that have been fatigue pre-cracked and to verify that the fatigue pre-crack meets validity requirements.

Specimen 236-SET-5 had no crack growth, this evidence is shown in the post-test photographs and is also evident in the Load vs. CMOD data record. The extreme overmatch properties of the weld as compared to the base metal properties resulted in net section necking of the base metal in the grips. Despite some apparent increase in CMOD, this change is attributed to blunting at the notch tip and is not associated with crack extension. Furthermore, initiation of a crack was not evident in the post-test photographs of each side of the specimen. Post-test photographs of each specimen are shown in Figure B52 and Figure B53. Specimen 236-SET-2 failed from the OD side of the weld after some stable ductile crack extension. This made it difficult to differentiate the delineation between crack growth and the typical brittle fracture surface after heat tinting. Careful observation of the surfaces showed the expected stable crack, front making it possible to obtain final crack length measurements for the nine-point average. Another examination of the fracture surface of 236-SET-2 shows that a lack-of-fusion flaw with porosity was the reason why the specimen failed in such a manner. A closer view of that fracture

surface is shown in Figure B54. Referring to Figure B2 and Table B2, specimen 236-SET-2 was sectioned from material adjacent to known NDE indications. The indications on the NDE inspection report only indicate porosity in that area but it is clear in this fracture surface that a lack of fusion is also present.

Specimens with notches in the HAZ were also photographed perpendicular to the notch plane to determine the out of plane crack growth, and is presented as "corrected crack growth". The results of the post-test measurements are presented in Table B9.

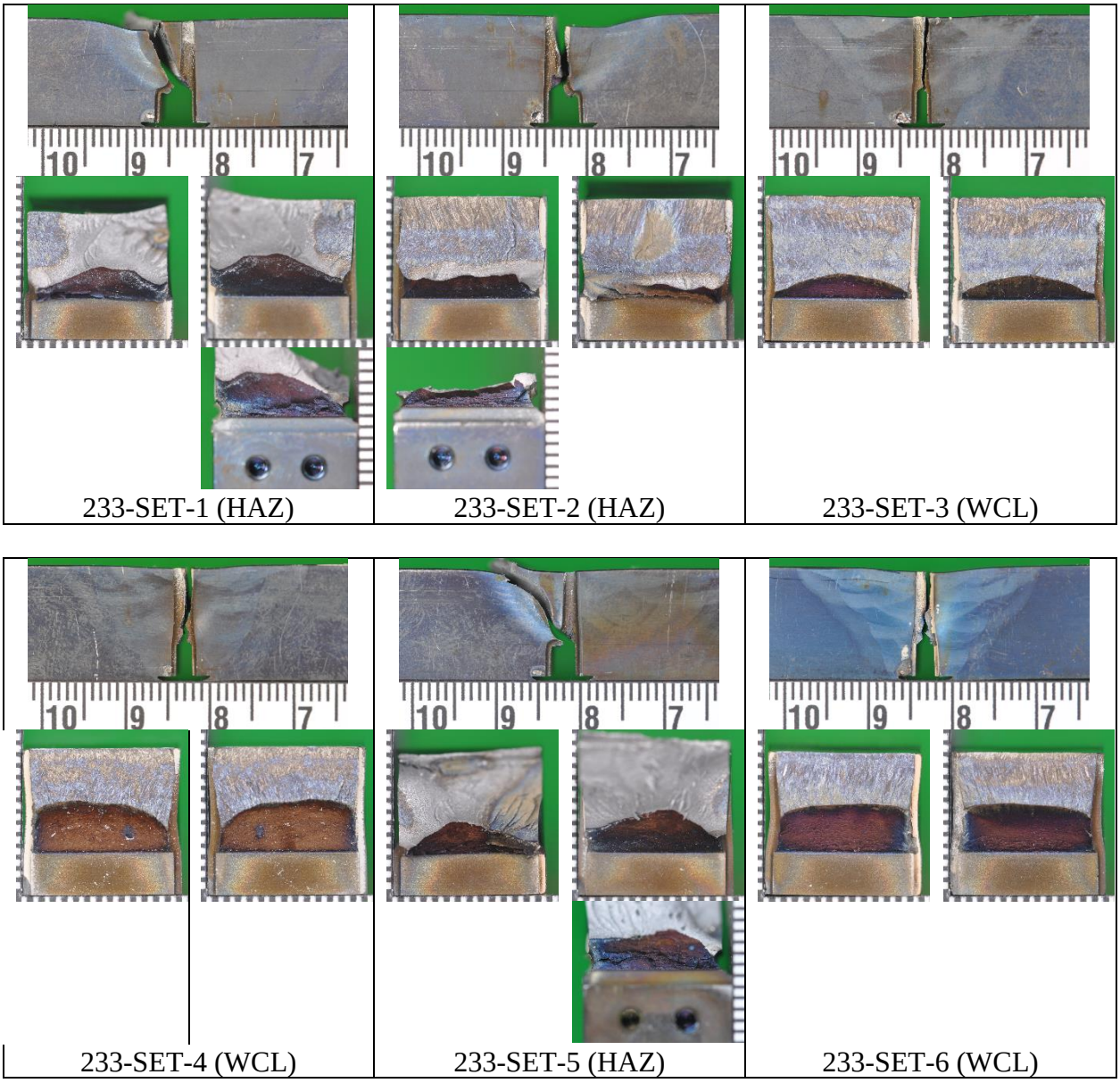

Figure B52 Post-test photographs of SE(T) specimens from the 16 mm – 19 mm WT weld (Weld-2)

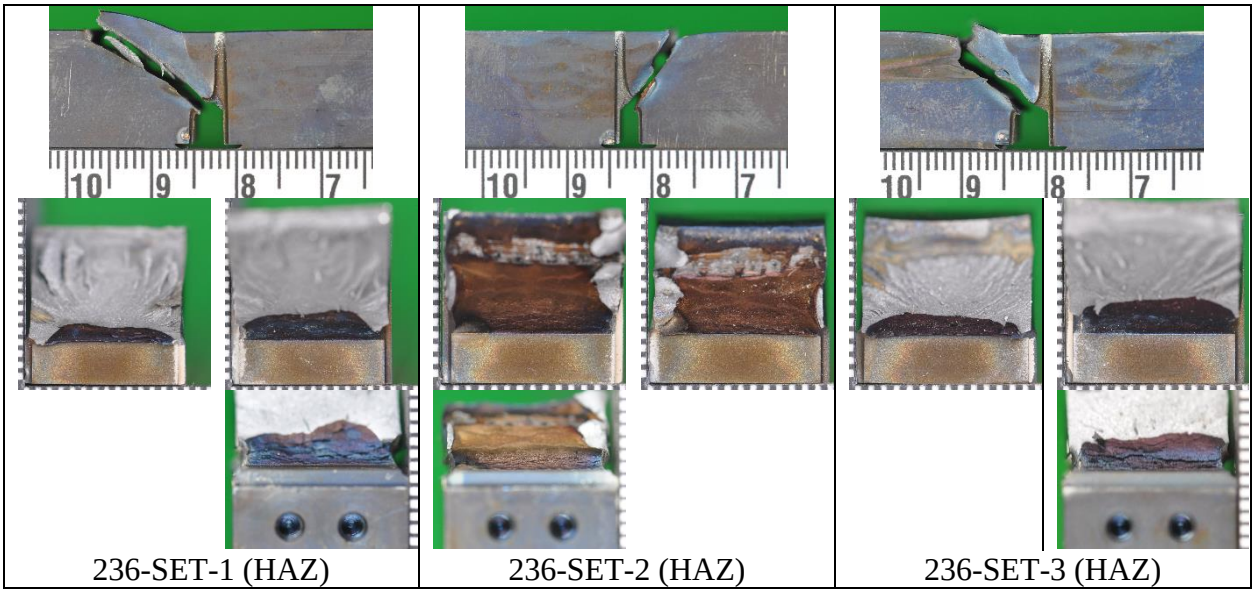

Figure B53 Post-test photographs of SE(T) specimens from the 16 mm – 16 mm WT weld (Weld-1)

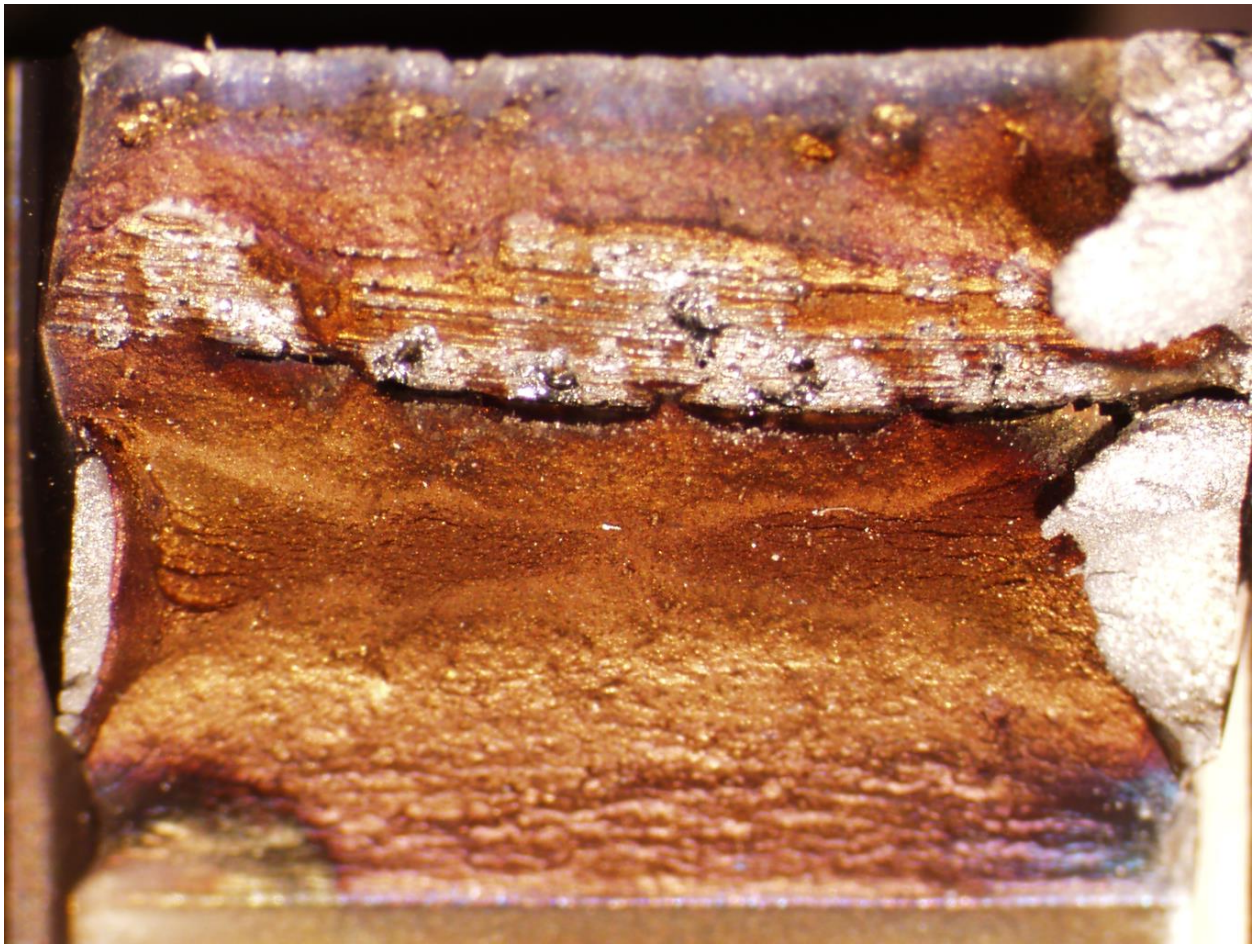

Figure B54 Post-test photograph of 236-SET-2 showing the area associated with lack of fusion and porosity. The OD surface of the specimen is shown at the top of the photograph.

Table B9 Post-Test SE(T) Specimen Measurements

914 mm (36 in) Outside Diameter – API-5L X70

Weld	Specimen ID	Initial a_0 (mm)	Post Test a_f (mm)	Crack Growth Δa (mm)	Corrected Crack Growth Δa (mm)
16 mm – 19 mm (Weld 233 [Weld-2])	233-SET-1	4.51	7.39	2.88	4.57
	233-SET-2	4.50	6.19	1.69	2.38
	233-SET-3	4.52	6.07	1.55	N/A
	233-SET-4	4.71	8.48	3.77	N/A
	233-SET-5	4.54	7.31	2.77	4.21
	233-SET-6	4.52	8.48	3.96	N/A
16 mm – 16 mm (Weld 236 [Weld-1])	236-SET-1	4.72	6.77	2.04	3.45
	236-SET-2	4.72	7.59	2.87	3.60
	236-SET-3	4.76	7.05	2.30	3.59
	236-SET-4	4.52	6.66	2.15	N/A
	236-SET-5	4.74	4.74	0	N/A
	236-SET-6	4.75	7.72	2.97	N/A

A representative Force-CMOD plot for Specimen 236-SET-1, notched in the HAZ, is shown in Figure B55. This test was run with a CMOD limit increment of 0.05 mm instead of 0.1 mm and resulted in more unloadings than necessary.

Since specimen 236-SET-5 showed no crack growth it warrants a closer examination of the data. The Force-CMOD plot for this specimen is shown in Figure B56.

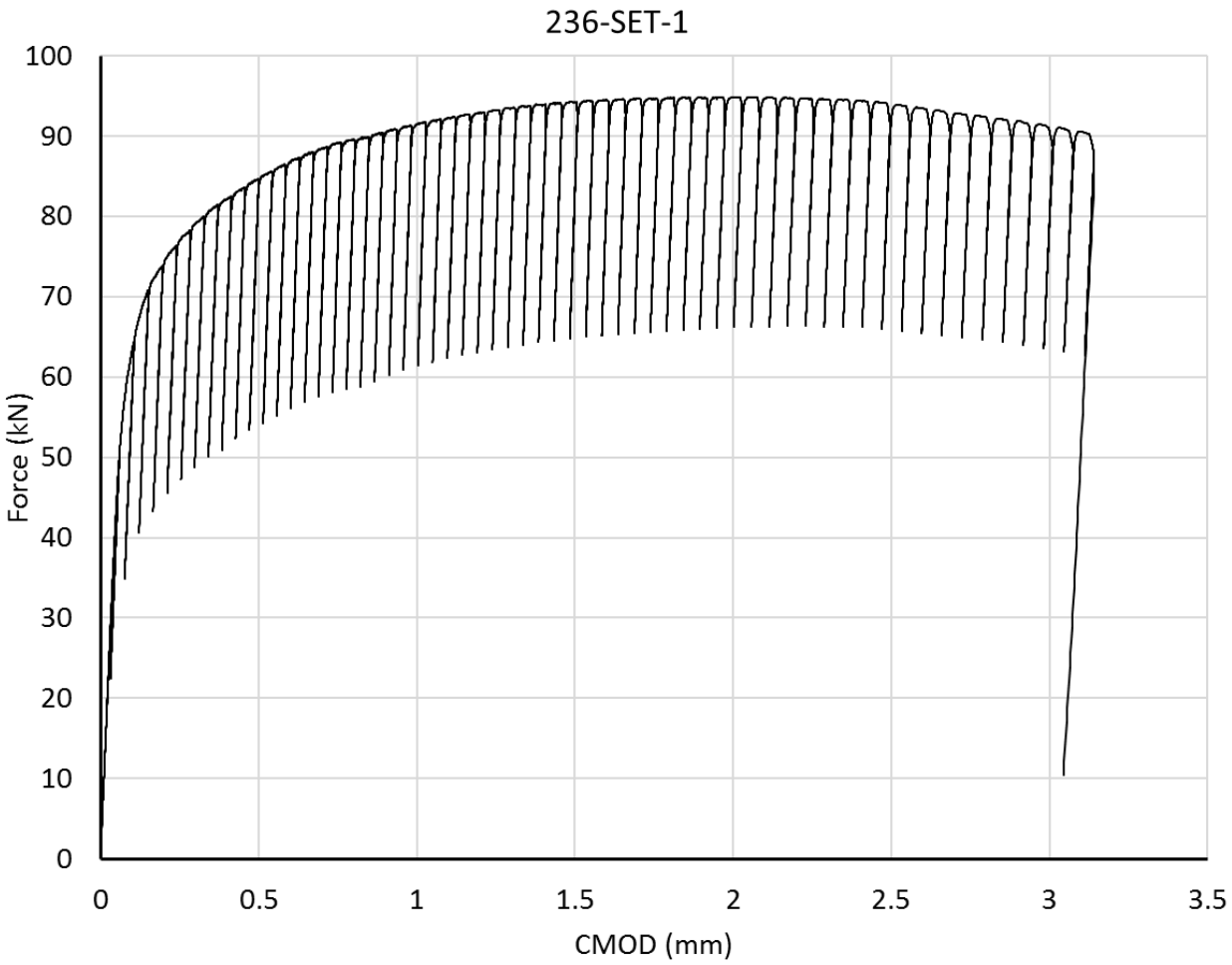

Figure B55 Plot of Force vs. CMOD for SE(T) specimen 236-SET-1. It is from these data that the CMOD-UC method will be used to generate the CTOD-R (δ-Δ*a*) curves.

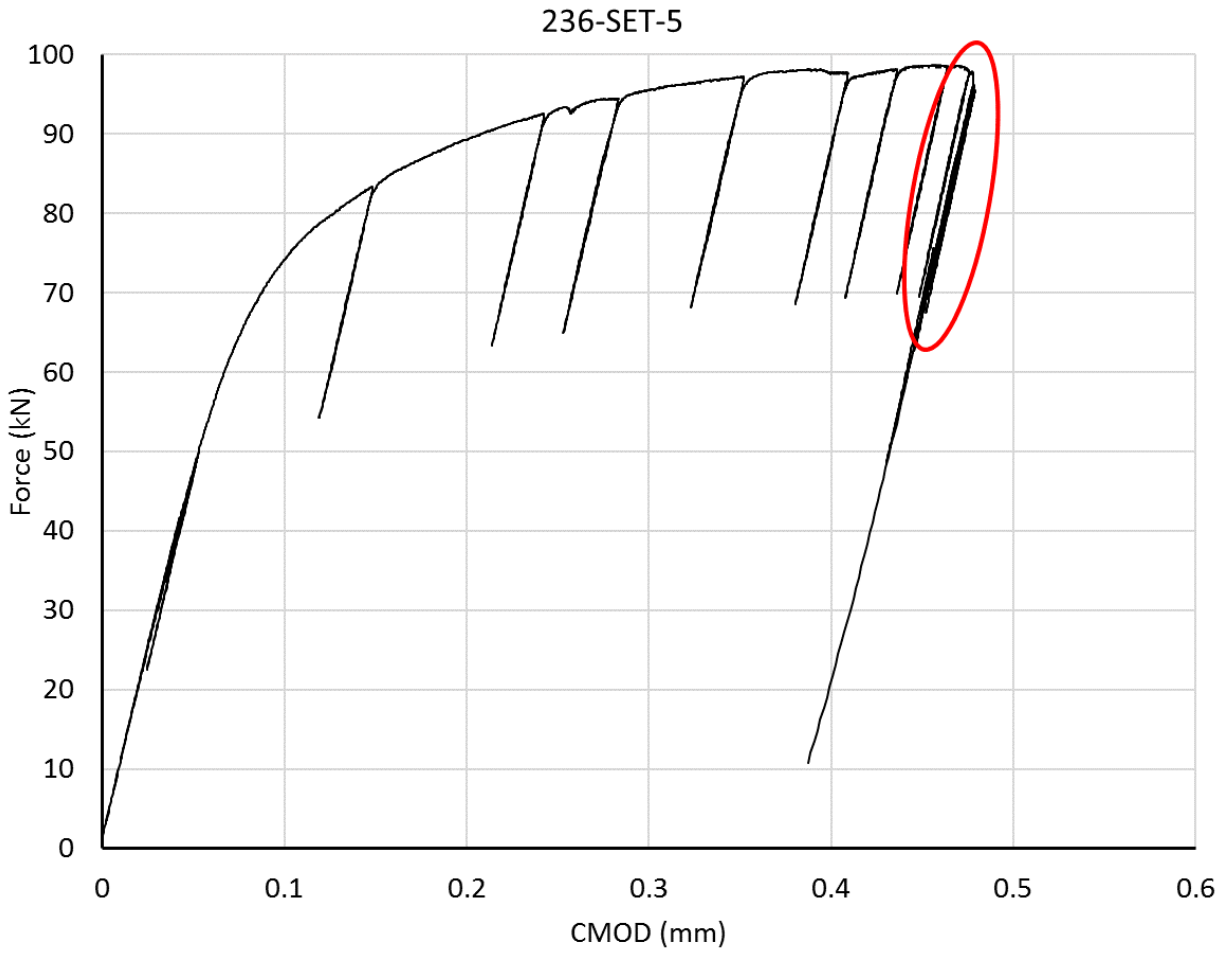

Figure B56 Plot of Force vs. CMOD for SE(T) specimen 236-SET-5. This plot shows multiple load drops associated with yielding and necking in the net section of the base metal. The region highlighted at the end of the data record included multiple unloadings with no change in CMOD. This range of CMOD data is typically associated with blunting and initiation. However, initiation of a crack was not evident on the fracture surface.

B.10 Single Edge Notched Bend Tests

A total of six preferred geometry Bx2B single edge notch bend (SENB) test specimens were cut from the supplied small sections of girth weld (Weld-1 and Weld-2) that were saved from between the CWP specimens. Thus, the specimen blanks came from different clock positions to evaluate both weld metal and HAZ fracture toughness. The specimen blanks were cut transverse to the girth weld and machined to the maximum thickness possible due to any hi-low misalignment or the final counter bore wall thickness. In the end, there was a one millimeter difference in the B dimensions, *i.e.*, B=15 mm for Weld 236 (Weld-1) and B=14 mm for Weld 233 (Weld-2). After machining the specimen blanks to size, they were etched by use of 3% Nital to reveal the weld metal and the HAZ regions and to accurately scribe the targeted region for subsequent notching, as shown in Figure B58. The weld metal centerline was found by bisecting

the weld width near the bottom root pass region of the specimen and then scribing a line along the through-thickness direction. For the HAZ specimen blanks, the targeted notch position was established within the central half of the through-thickness B dimension to maximize the amount of HAZ sampled (See Figure B57 for examples of the notch placements). The through-thickness notching of individual specimens was completed using small 0.25 mm diameter wire electrical discharge machining (EDM). The starter notch was cut to the required depth (13 mm for Weld 236 (Weld-1) and 12 mm for Weld 233 [Weld-2]) and incorporated an integral knife edge with 2 mm wide opening for attachment of a single clip gauge. Prior to fatigue pre-cracking a controlled local compression technique was used to meet crack front straightness requirements by compressing the remaining unnotched ligament using hardened platens to a total strain between 0.5 % and 0.7 %. This was followed by fatigue pre-cracking each specimen by about 2 mm to achieve a final targeted crack length ratio of $a/W = 0.5$.

All specimens were tested at -10 °C in a universal testing machine after stabilizing the temperature for approximately 15 mins prior to testing. Yield and ultimate tensile strengths for pre-cracking and for calculation of CTOD were obtained using the room temperature all weld metal and longitudinal pipe base metal test data obtained by NIST. The values for the sub-zero test temperature were derived from the test data from NIST per the methods outlined in ISO 15653 Section 12.1. Load-CMOD displacement curves were recorded for each test and used to determine the significance of any pop-ins as well as in the calculations of crack-tip opening displacement as outlined in the standard.

After testing the all specimens were subjected to heat tinting in an oven set at 300 °C for 30 mins. Each of the specimens was cooled in liquid nitrogen prior to being broken apart to facilitate measurement of the final crack length and to determine if the associated crack front validity requirements were met. A photograph from one half of the fracture surfaces of each test specimen is presented in Figure B59.

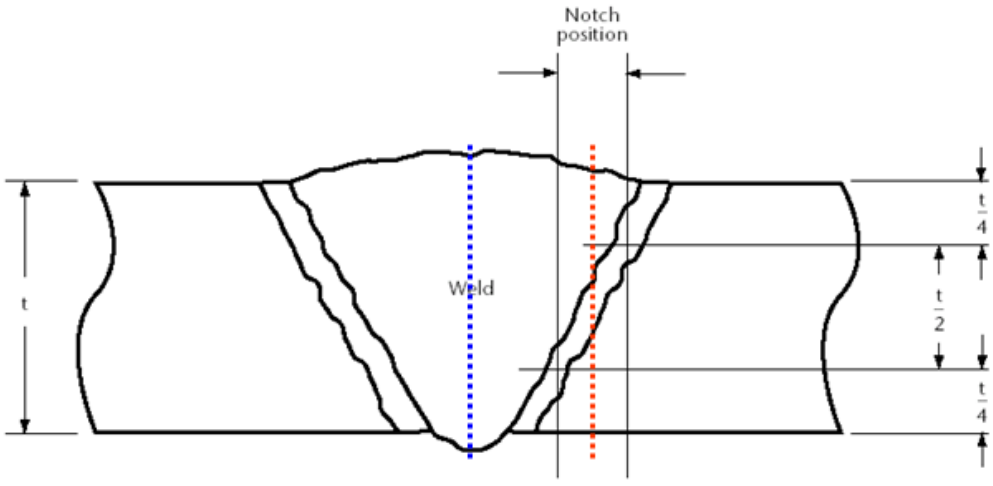

Figure B57 Schematic diagram showing the notch position for (a) WMC (dashed blue vertical line) and (b) HAZ (dashed red vertical line) for CTOD fracture specimens.

A summary of the CTOD test results are presented in Table B10 as well as graphically in the bar chart shown in Figure B60.

From the data listed in the table it clear that the WMC tests exhibited reasonably consistent fracture toughness with a similar range of δc, δu and δm values obtained, e.g., lower bound δc values of 0.012 mm and 0.010 mm, while the δm values of 0.21 mm and 0.15 mm for Welds 236 (Weld-1) and Weld 233 (Weld-2), respectively. These results are consistent with a large pop-in fracture for the former and smaller thumb nail shaped fracture for the latter, as shown in individual photographs in Figure B59.

In contrast, there were considerable differences in fracture toughness observed for the HAZ test conducted on Weld 236 (Weld-1). In this case, two very low δc values = 0.02 mm and one δm value = 0.77 mm were obtained. In the former case, isolated pop-ins (see photographs in Figure B59) resulted in low values, while the much higher result may have resulted from inconsistent notch placement and/or the fracture deviating towards the base metal, although this would require more detailed investigations to confirm that this was the case. For the Weld 233 (Weld-2), the HAZ CTOD results were generally more consistent with two δm values of 0.36 mm and 0.48 mm and one δc value of 0.18 mm. Another factor that was considered to influence the HAZ fracture toughness was the change in fusion line profile and ultimately the fraction of coarse grain HAZ that is sampled for a given test specimen.

(a) Weld 236-WMC-2

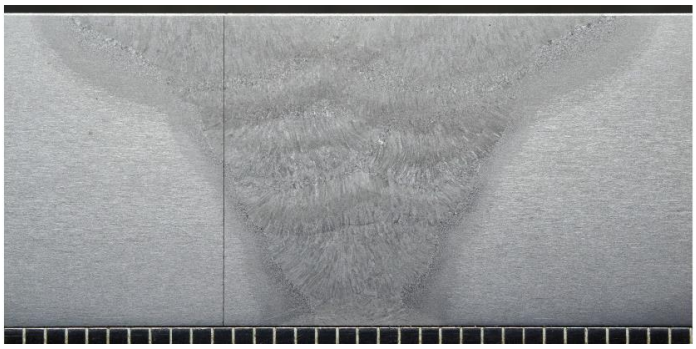

(b) Weld 236-HAZ-3

(c) Weld 233-WMC-3

(d) Weld 233-HAZ-4

Figure B58 Representative macrographs showing the notch position for WMC and HAZ test specimens from Welds 236 and 233

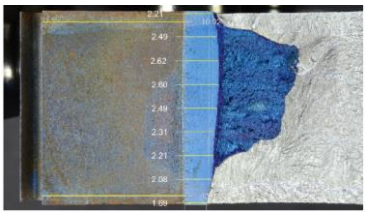

236-WMC-2

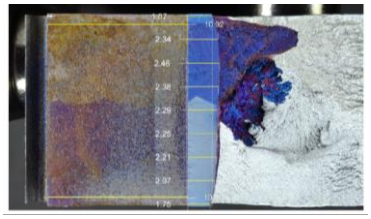

236-HAZ-1

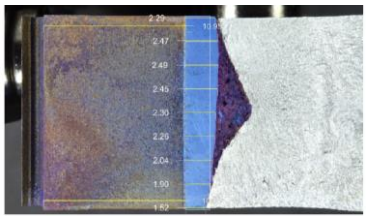

236-WMC-4

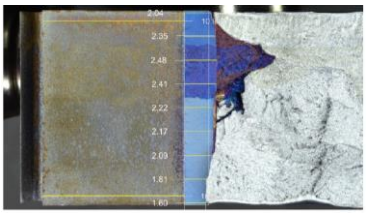

236-HAZ-3

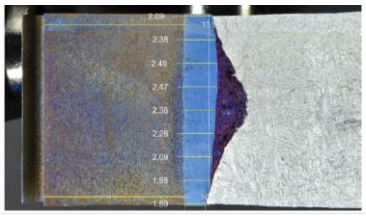

236-WMC-6

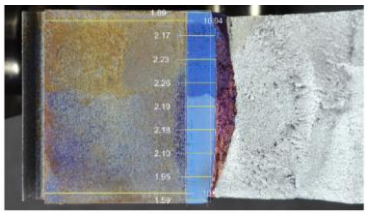

236-HAZ-5

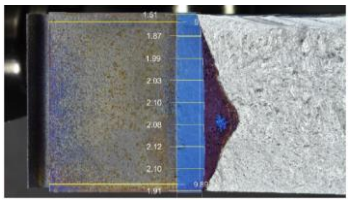

233-WMC-1

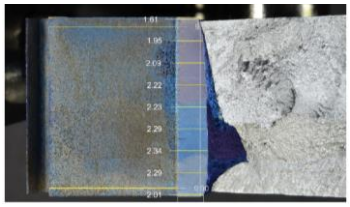

233-HAZ-2

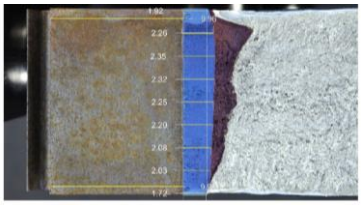

233-WMC-3

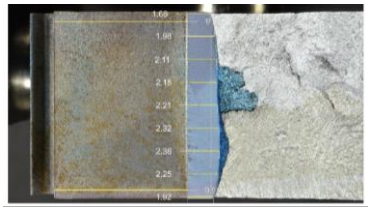

233-HAZ-4

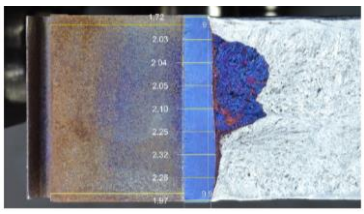

233-WMC-5

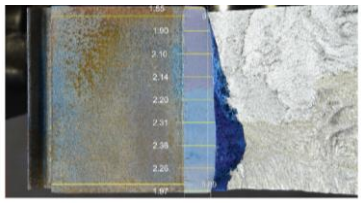

233-HAZ-6

Figure B59 Photographs of fracture surfaces of CTOD specimens from Welds 236 and 233

Table B10 CTOD results for WMC and HAZ testing of FCAW 236 (16 mm to 16 mm)

Weld ID	Notch Location	Specimen ID	Notch Position	CTOD (mm)	CTOD (in)	Fracture Mode
236	WMC	236-WMC-2	centered	0.12	0.005	c
		236-WMC-4	Off-center	0.20	0.008	u/c
		236-WMC-6	centered	0.21	0.008	m
	HAZ	236-HAZ-1	HAZ targeted	0.02	0.0006	c
		236-HAZ-3	HAZ targeted	0.02	0.0007	c
		236-HAZ-5	Away from FL	0.77	0.0302	m
233	WMC	233-WMC-1	off-center	0.14	0.005	u
		233-WMC-3	centered	0.15	0.006	m
		233-WMC-5	centered	0.10	0.004	c
	HAZ	233-HAZ-2	biased to WM	0.36	0.014	m
		233-HAZ-4	HAZ targeted	0.18	0.007	c
		233-HAZ-6	biased to WM	0.48	0.019	m

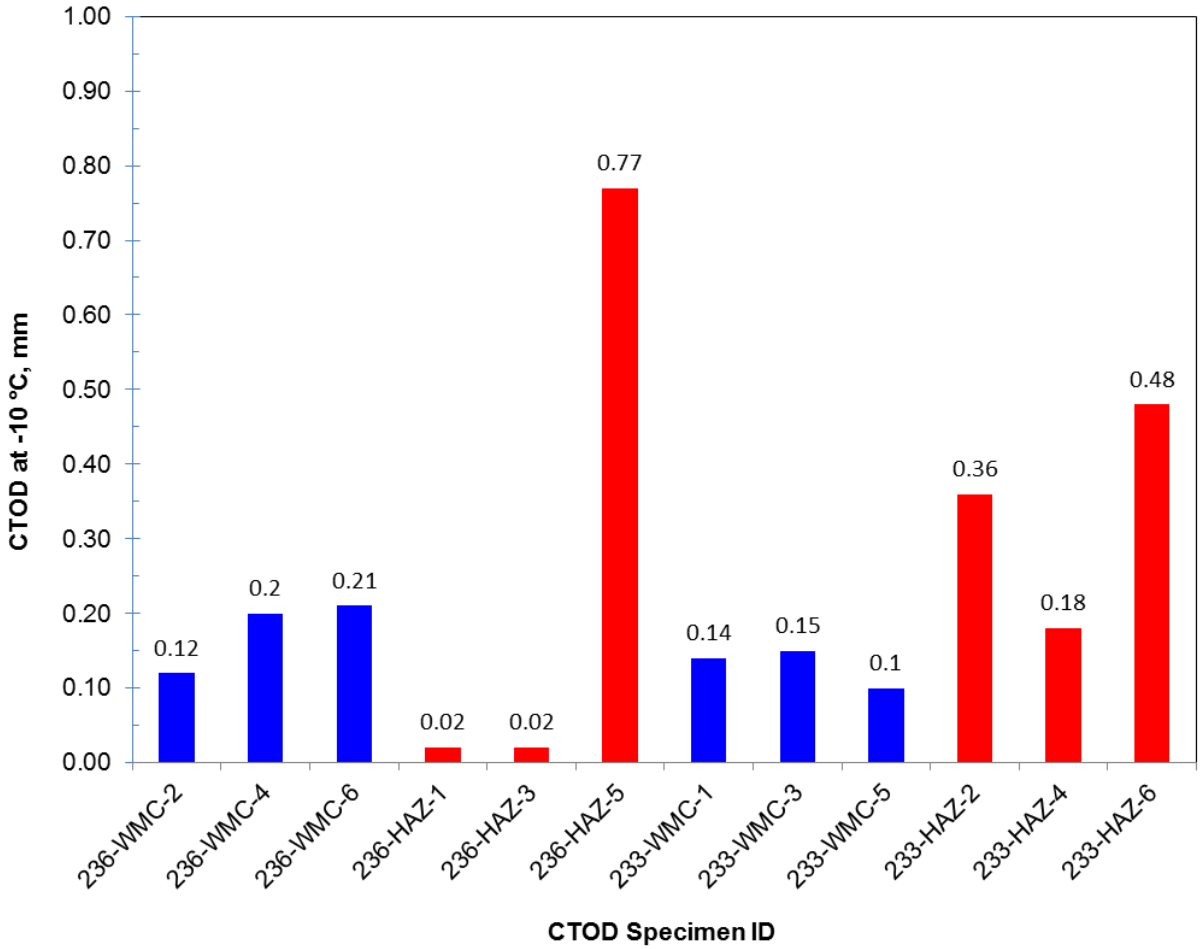

Figure B60 Bar chart showing WMC and HAZ CTOD values obtained from Welds 236 and 233